Université d'Ottawa · University of Ottawa

Université d'Ottawa • University of Ottawa

FACULTÉ DES ÉTUDES SUPÉRIEURES ET POSTDOCTORALES

FACULTY OF GRADUATE AND POSTDOCTORAL STUDIES

Fedora GONZALEZ

AUTEUR DE LA THÈSE - AUTHOR OF THESIS

M. Sc.(Earth Sciences)

GRADE - DEGREE

Department of Earth Sciences

FACULTÉ, ÉCOLE, DÉPARTEMENT - FACULTY, SCHOOL, DEPARTMENT

TITRE DE LA THÈSE - TITLE OF THE THESIS

Mineral Magnetism of Synthetic Microcrystalline and Nanophase Iron Oxyhydroxides and Iron Oxides

D. Rancourt

DIRECTEUR DE LA THÈSE - THESIS SUPERVISOR

CO-DIRECTEUR DE LA THÈSE - THESIS CO-SUPERVISOR

EXAMINATEURS DE LA THÈSE - THESIS EXAMINERS

A. Lalonde

K. Torrance

J.-M. De Koninck, Ph.D.

LE DOYEN DE LA FACULTÉ DES ÉTUDES SUPÉRIEURES ET POSTDOCTORALES

DEAN OF THE FACULTY OF GRADUATE AND POSTDOCTORAL STUDIES

MINERAL MAGNETISM OF SYNTHETIC MICROCRYSTALLINE AND NANOPHASE IRON OXIDES AND IRON OXYHYDROXIDES

by

Fedora González Lucena

A thesis submitted to the School of Graduate Studies and Research

in partial fulfillment of the requirements

for the degree of M.Sc. in Earth Sciences

OTTAWA-CARLETON GEOSCIENCE CENTRE

AND

UNIVERSITY OF OTTAWA

OTTAWA, CANADA

Your file Votre référence
ISBN: 0-494-01481-4
Our file Notre référence
ISBN: 0-494-01481-4

To Alessandro Talamonti

Abstract

A suite of well-characterized synthetic microcrystalline hematite samples, 2-line and 6-line ferrihydrite samples and nanohematite samples are studied through magnetization–field curves measured at room temperature. The single-domain microcrystalline hematite samples are analyzed through basic hysteresis parameters providing sample characteristics such as magnetic anisotropy information, the effect of annealing on the origin of the magnetization and the relatively constant intrinsic high field susceptibility. The application of a magnetic granulometry method on the magnetic data of the superparamagnetic nanohematite and ferrihydrite samples provides fundamental information such as the intrinsic mass magnetization and estimated particle size. Additionally, it gives insight into possible moment formation mechanisms within the superparamagnetic particles. The observed differences between the magnetic properties of the magnetically blocked and the superparamagnetic samples considered are also discussed.

Résumé

Une suite d'échantillons synthétiques microcristallins et bien caractérisés d'hématite, de ferrihydrite à 2 lignes et à 6 lignes et de nanohématite sont étudiés à l'aide de courbes de magnétisation, mesurées à température de la pièce. Les échantillons d'hématite qui sont des microcristaux à domaines magnétiques uniques sont analysés à l'aide de paramètres d'hystérésis de base, qui fournissent certaines caractéristiques de ces échantillons telles que de l'information sur l'anisotropie magnétique, l'effet de traitements thermiques sur l'origine de la magnétisation et la susceptibilité intrinsèque en champ élevé. L'application d'une méthode de granulométrie magnétique sur les données magnétiques des échantillons superparamagnétiques de nanohématite et de ferrihydrite nous donne de l'information fondamentale tel que la magnétisation intrinsèque de masse et une estimation de la grosseur des particules. De façon additionnelle, elle nous donne un aperçu des mécanismes possibles de la formation du moment à l'intérieur des particules. Les différences observées entre les propriétés magnétiques des échantillons magnétiquement bloqués et celles des échantillons superparamagnétiques sont aussi discutées.

Resumen

Un grupo de muestras de hematita sintética microcristalina, ferrihidratos de 2 líneas y 6 líneas, y nanohematita, se estudiaron a través de curvas de magnetización versus campo magnético adquiridas a temperatura ambiente. Las muestras que presentan un dominio magnético (hematitas microcristalinas) fueron analizadas a través de parámetros básicos de histéresis, los cuales proveen características tales como: información sobre anisotropía magnética, el efecto de tratamientos térmicos a altas temperaturas en el origen de la magnetización, y la invariabilidad del parámetro de susceptibilidad magnética en campos magnéticos altos. La aplicación de un método de granulometría magnética sobre los datos de las muestras superparamagnéticas (nanohematitas y ferrihidratos) permite obtener información fundamental tal como la magnetización intrínsica por masa de la partícula y la estimación de su tamaño. Adicionalmente, sugiere posibles mecanismos de formación del momento en la partícula superparamagnética. También se discuten las diferencias observadas de las propiedades magnéticas de las muestras bloqueadas magnéticamente y las muestras superparamagnéticas.

Table of Contents

List of Tables

List of Figures

Index of Symbols, Acronyms and Abbreviations

□	Vacancy in general structural formula for hematite
α	Exponent of n in relationship between μ' and n
χ_d	Demagnetization slope
χ_o	Initial slope
χ_g	Mass susceptibility of sample
χ_s	Mass susceptibility of sugar
μ	Supermoment of a particle
μ'	Number of cations contributing to supermoment
μ_B	Bohr magneton = 9.2741×10^{-21} erg/G
μ_s	Magnetic moment of sample
ρ	Density
A	Proportionality factor in relationship between μ' and n
A, B, C	Proportionality factors in terms of general moment formation model
AF	Antiferromagnetic
b	Number of incorporated molecules of water in hematite structure
C_1	Intercept of best-fit line in the graph χ_g versus H^2
C_2	Slope of best-fit line in the graph χ_g versus H^2
CANMET	Canada Centre for Mineral and Energy Technology
d	Diameter of spherical superparamagnetic particle
DDI	Distilled deionised (water)
DTA	Differential thermal analysis

g	Landé g-factor
GC	Gas chromatography
GSC	Geological Survey of Canada
H	Applied magnetic field
H_c	Magnetic coercivity
ICP-ES	Inductively coupled plasma emission spectroscopy
J	Atomic total angular momentum quantum number
k_B	Boltzmann's constant = 1.3807×10^{-16} erg/K
L	Atomic orbital momentum quantum number
LHT	Liquid helium temperature
LSSE	Lake Sediment Structure and Evolution research group
LT	Low temperature
m	Mass of sample
M_a	Mass of a molecule of hematite / ferrihydrite containing one Fe^{3+} cation
MITE	Metals in the environment project
M_g	Mass magnetization
M_m	Molecular weight of hematite/ferrihydrite
M_{max}	Maximum magnetization
M_r	Remanent magnetization
m_p	Mass of superparamagnetic particle
M_s	Spontaneous magnetization
MS	Mössbauer spectroscopy
n	Number of magnetic cations per particle

N	Number of magnetic cations per unit mass
N_A	Avogadro's number = 6.022×10^{23}
p	Effective paramagnetic Bohr magneton number
PBH	Pure bulk hematite
pXRD	Powder X-ray diffraction
RT	Room temperature
S	Atomic spin momentum quantum number
SD	Single-domain
SEM	Scanning electron microscopy
SP	Superparamagnetism / Superparamagnetic
SQUID	Super quantum interference device
T	Temperature
TGA	Thermogravimetric analysis
VSM	Vibrating sample magnetometer
x	Parameter in general structural formula for hematite-like materials
Z	Number of formula units per unit cell.

Chapter 1 - Introduction

The present thesis presents a magnetic characterization study of synthetic iron mineral phases meant to represent, to a certain degree, a group of commonly occurring iron bearing mineral phases in surface environments, such as soils, sediments and aquatic environments. Iron bearing minerals are widespread in the environment due to both the fact that iron is the fourth most abundant element in the Earth's crust and that it is readily available in multiple valences hence participating in various geochemical reactions in different environments. Iron is the most abundant magnetic element therefore mineral magnetometry is a potentially sensitive tool for characterizing iron bearing minerals.

The "original contribution" of the present work relies in the fact that it is a complementary characterization work performed on a group of samples previously studied through other experimental techniques such as powder X-ray diffraction, ^{57}Fe Mössbauer spectroscopy, gas chromatography and thermogravimetric analyses, among others. In this work the author develops an experimental procedure using a Vibrating Sample Magnetometer (VSM). The mineral magnetometry methodology applied in this thesis provides sample characteristics not given by other experimental techniques, including the first application of a recently developed magnetic granulometry method (Rancourt *et al.*, 2004).

The samples studied in this work consist of a suite of synthetic single-domain microcrystalline hematite samples that cover a wide range of defect proportion within their structure, a group of synthetic nanohematite samples, and a group of synthetic 2-line

ferrihydrite samples, including samples co-precipitated with sulphur and phosphate, and a synthetic 6-line ferrihydrite sample.

Hematite is the most stable iron oxide in surface environments. Its broad size range of single-domain behaviour makes it common to find it in this state in nature. The single-domain microcrystalline hematite samples considered in this study present a wide range of proportion of defects, attempting to represent many types of natural hematite in sediments and soils.

The magnetism of hematite has been a complex subject of discussion. The basic general consensus is that hematite possesses two "types" of magnetism. One type of magnetism is caused by the "spin-canted moment" which has its origin in a weak ferromagnetism resulting from a small canting of the spins towards each other in the antiferromagnetic lattice. This results in a net spontaneous moment perpendicular to the main antiferromagnetic axis (Dzyaloshinsky, 1958) and has its origin in an anisotropic superexchange interaction of the spin coupling (Moriya, 1960). Despite the many attempts to study the weak ferromagnetism of hematite, it is still poorly understood (Fuller, 1970). The other type of magnetism is caused by the "defect moment" whose origin is related to imperfections or defects in the crystalline structure of hematite, such as vacancies, impurities, displacements, dislocations and plane defects, which cause imperfect cancellation of the antiferromagnetic structure, resulting in a net moment.

Experiments on natural single crystals of hematite agree that at room temperature the weak ferromagnetism lies within the basal plane (e.g., Néel and Pauthenet, 1952; Lin, 1959). This weak ferromagnetism has been observed, through hysteresis curves at room temperature

and low fields, to be confined to the basal plane in a single crystal of hematite, and it has been shown to present different magnitudes of triaxial and uniaxial magnetic anisotropies among natural and synthetic specimens within this plane (e.g., Tasaki and Iida, 1963; Flanders and Remeika, 1965; Besser *et al.*, 1967).

The magnetocrystalline anisotropy of hematite is affected by temperature. The dipolar anisotropies and local ionic anisotropies in hematite are both significant and have opposite signs; their relative magnitude changes with temperature. At a temperature value of approximately 260 K (Morin temperature), the two anisotropies are equal in magnitude, and above or below this temperature, the change of sign of the net anisotropy changes the crystallographic easy axes; this is called the Morin transition. The Morin transition is sensitive to sample features such as particle size, particle shape, impurities and chemistry (Dang *et al.*, 1998) and therefore it can be suppressed to lower temperatures and sometimes not observable at temperature above 4.2 K. Some of the microcrystalline hematite samples considered in this thesis have a Morin transition and some do not show it.

Fine nanophase particles present different physical properties than their bulk counterparts. Specifically in magnetism, the nanophase nature takes special importance since the manifestation of superparamagnetism and surface effects mainly dominate the resultant magnetism of the nanoparticles. In this sense, it becomes necessary to study the magnetic properties of these nanophase materials.

The nanophase iron oxides and iron oxyhydroxides, such as the natural analogues of the nanohematite and the ferrihydrite samples considered in this study, are considered relevant in the soil formation on the Earth and probably even Mars (e.g., Bishop, 1998).

Ferrihydrites are very important in environmental surface processes. Ferrihydrite is common in water and sediments of lake and marine environments and in soils that undergo early rapid weathering (Jambor and Dutrizac, 1998). It is also common in mine waters and acid mine drainage (e.g., Bigham *et al.*, 1996), where it can adsorb toxic elements, such as arsenic (Rancourt *et al.*, 2001; Carlson *et al.*, 2002).

Ferrihydrite is a poorly ordered iron oxyhydroxide and its structure is still a subject of debate (e.g., Eggleton and Fitzpatrick, 1988; Jambor and Dutrizac, 1998). The chemical formula assigned to ferrihydrite varies; the most common stoichiometric formulas are $Fe_5HO_8 \cdot 4H_2O$ or $5Fe_2O_3 \cdot 9H_2O$ or $Fe_2O_3 \cdot 2FeOOH \cdot 2.6H_2O$ (Jambor and Dutrizac, 1998). Ferrihydrites are commonly described according to the main broad peaks visible in their X-ray diffractograms. The number of broad peaks range between two and seven; more visible peaks imply more crystallinity. The most common types of ferrihydrites studied are 2-line ferrihydrites and 6-line ferrihydrites, and these are the types considered in this thesis.

6-line ferrihydrite has been described as being an antiferromagnetic material (Pankhurst and Pollard, 1992; Jansen *et al.*, 2002) with a parasitic ferromagnetic component and as showing superparamagnetic behaviour at room temperature (Zergenyi *et al.*, 2000). 2-line ferrihydrite has been described as an antiferromagnetic material by Seehra *et al.*, 2000. Pankhurst and Pollard (1992) suggest that in 2-line ferrihydrites a two-sublattice ferrimagnetism originates from the uncompensation of the moments through the particle, due to the structural disorder, or at the surface due to the large surface area.

This thesis presents the results of room temperature magnetization-field cycle runs performed on the samples using a VSM. The extracted information is analyzed, providing

fundamental characteristics of the samples. The structure of this thesis is summarized as follows: Chapter 2 shows theoretical simulations of the magnetic behaviours of paramagnetism and superparamagnetism. Chapter 3 summarizes the initial exploratory work done using different types of natural sediment samples and provides insight into the complexity and advantages of interpreting magnetic data in natural samples; additionally, it provides a justification for the samples selected to be the focus of this thesis. Chapter 4 gives a description of the samples and shows all the characterization previously performed on them. Chapter 5 describes the experimental methodology used to obtain room temperature field cycles. Chapter 6 presents the processed results as corrected field cycle graphs from where the interpretable data is extracted. Chapter 7 describes the methods of analysis of the field cycles and the procedure for extracting information about the samples. Finally, chapter 8 presents the analysis of the extracted information and further discussion.

I would like to take the opportunity to thank my supervisor Dr. Denis Rancourt for his continuous guidance and availability for discussions about the thesis. I am grateful to Dr. Mei-Zhen Dang for her continuous help in providing information about the microcrystalline hematite samples. I would also like to express my gratitude to Dr. Gilles Lamarche for his training and guidance when performing low temperature measurements. I also appreciate the help from Pierre-Jean Thibault in providing information about the ferrihydrite samples. I am as well grateful to Prof. André Lalonde for his guidance in the sample preparation during the exploratory work. I finally thank Ana Delgado for her disposition in running the TGA-DTA measurements of the nanophase samples.

Chapter 2 - Theoretical Simulations of Paramagnetism and Superparamagnetism

The basic magnetic properties of solid materials can be described in terms of the properties of the atomic magnetic moments and the interactions between them. Table 2.1 describes the main categories of magnetic behaviour: diamagnetism, paramagnetism, ferromagnetism, antiferromagnetism, weak ferromagnetism, ferrimagnetism, and superparamagnetism. In general, all materials present the weak diamagnetic behaviour related to the closed shells of the atoms. When the magnetic moments are non-interacting the material is paramagnetic. A material that has interacting moments but that is at a temperature above its magnetic ordering temperature is also said to be paramagnetic, or in its 'paramagnetic state' as opposed to its 'magnetically ordered state'. A material that presents magnetic exchange interactions between the atomic moments is said to be 'magnetically ordered' at temperatures below its magnetic ordering temperature, if such an ordering temperature occurs. The magnetically ordered states of such materials can be ferromagnetic, antiferromagnetic, or weak ferromagnetic (or other less common types of magnetic order). If the particle size of these materials is small enough for the thermal energy to be comparable to the particle's barrier energy, then the material is superparamagnetic.

	Atomic/Magnetic Behaviour	Moment Configuration	Induced Magnetization
Diamagnetism	Atoms have no net magnetic moment.		Negative and small
Paramagnetism	The atomic magnetic moments are randomly oriented in zero field, at any instant.	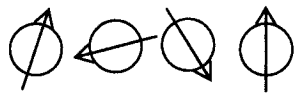	Positive and small
Ferromagnetism	The moments are aligned in a parallel way.	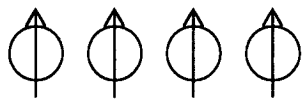	Positive and large. It shows hysteresis effects
Antiferromagnetism (AF)	The moments are aligned in two antiparallel sublattices with equal moment magnitude. The net moment is zero in zero field.	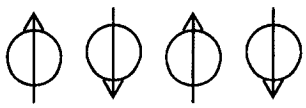	Positive and small
Weak Ferromagnetism (AF with spin canting)	The moments are aligned in an antiparallel way with a slight canting of the moments. There is a resultant spontaneous net moment perpendicular to the AF axis		Positive and large. It shows hysteresis effects.
Ferrimagnetism	The moments are aligned in two antiparallel sublattices. One sublattice has a greater moment than the other.	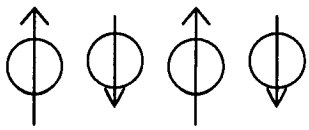	Positive and large. It shows hysteresis effects
Superparamagnetism	The relatively high thermal energy causes the net particle moment (or supermoment) to spontaneously flip between easy directions	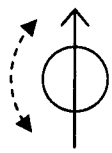	Positive and it can be very large.

Table 2.1 Main types of magnetic behaviour in materials

This chapter presents theoretical simulations of the behaviour of paramagnetism and superparamagnetism. The theoretical equations of these two types of magnetism are used to simulate the magnetization behaviour with respect to the applied field. These magnetic behaviours show distinguishable magnetic responses and this allows the interpretation of the magnetic configuration of the particles in the sample.

2.1 Paramagnetism

The simulations for paramagnetism are done using the Curie's Law for paramagnets at small fields:

$$M_g(H,T) = \frac{Ng^2\mu_B{}^2 J(J+1)H}{3k_B T} \qquad (2\text{-}1),$$

where:

M_g is the mass magnetization

N is the number of Fe^{3+} cations per gram of sample

g is the Landé g-factor = 2, for Fe^{3+} cations

μ_B is the Bohr magneton = 9.2741×10^{-21} erg/G

J is the atomic total angular momentum quantum number for Fe^{3+} = 5/2

H is the applied magnetic field

k_B is the Boltzmann's constant: 1.3807×10^{-16} erg/K

T is the temperature in Kelvin

The N used for these simulations is the one derived from the stoichiometry of the general formulas of hematite (Fe_2O_3) and ferrihydrite ($Fe_5HO_8 \cdot 4H_2O$ or $5Fe_2O_3 \cdot 9H_2O$ or $Fe_2O_3 \cdot 2FeOOH \cdot 2.6H_2O$), 7.54 x 10^{21} Fe^{3+}/g and 6.27 x 10^{21} Fe^{3+}/g, respectively. The field is varied in the range [-10 kG, 10 kG], and the temperature used is 290 K.

These simulations are based on the assumption that all of the Fe^{3+} cations present in the sample are paramagnetic, so it is assumed that all the cations contribute to the paramagnetism of the sample. Figure 2.1 shows the resultant graphs.

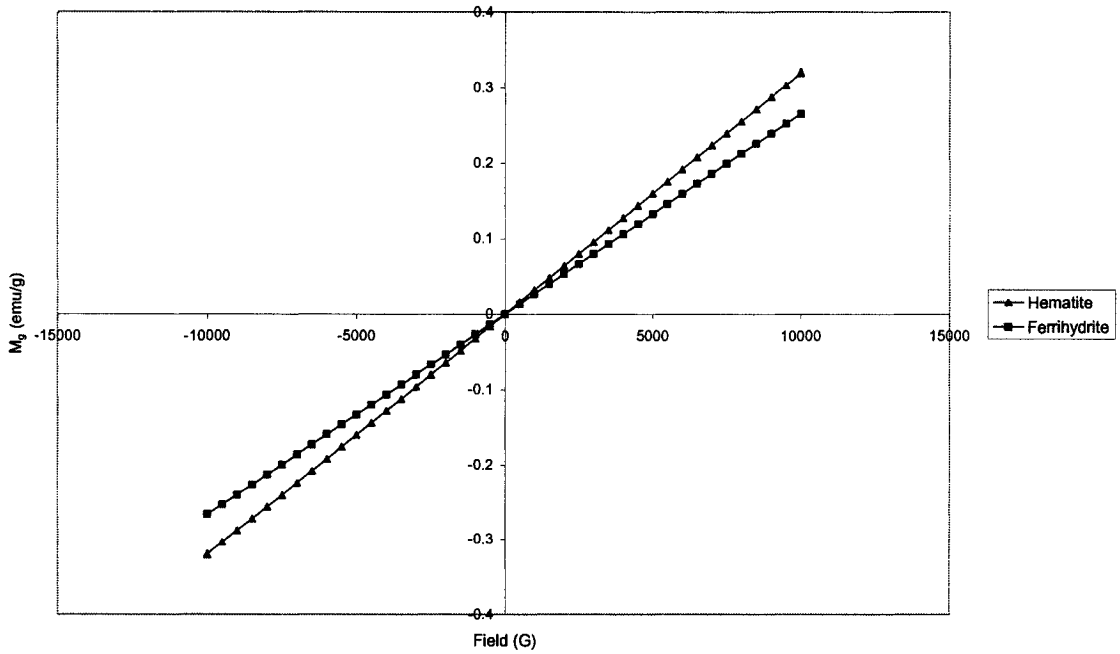

Figure 2.1 Simulation of paramagnetic behaviour for hematite and ferrihydrite

2.2 Superparamagnetism

Normally, the thermal energy of a single-domain particle is smaller than the crystalline, magnetoelastic or shape anisotropy energy; but when the particle size of the particle becomes small enough, the latter energies become comparable to the thermal energy and therefore spontaneous reversals of the supermoment take place. This thermally active condition is called superparamagnetism (Bean and Livingston, 1959).

When dealing with systems of fine particles such as those in nanophase materials it is important to study the superparamagnetism of the sample since it has a fundamental role in its magnetic properties. The following simulations present the magnetic behaviour of systems with different particle size and intra-particle spin configuration. The magnetization per unit mass due to superparamagnetism can be expressed as:

$$M_g(H,T) = \frac{N}{n}\mu L\left(\frac{\mu H}{k_B T}\right) \qquad (2\text{-}2),$$

where:

$$L(x) = coth(x) - \frac{1}{x} \qquad (2\text{-}3).$$

Here, $L(x)$ is the Langevin function and μ is the supermoment magnitude of a particle. Each particle is taken to be made up of n moment-bearing cations (Fe^{3+} cations) and the supermoment magnitude is expressed as μ' atomic moments:

$$\mu = \mu' g \mu_B J \qquad (2\text{-}4).$$

The simulations presented here are based on a general model of spin configuration that relates the total number of magnetic cations (n) with the number of magnetic cations that contribute to the supermoment of a particle (μ') in a proportional way. This is expressed as:

$$\mu' = A\, n \qquad (2\text{-}5).$$

The study of this model consists in varying the proportionality factor, A, and the number of magnetic cations, n, which implies a variation in the size of the particle, in order to see what are the effects in the superparamagnetic magnetization. Four different A values are considered ranging from 0.01 to 1 and n is varied from 10 to 10,000. The results for the case of ferrihydrites are shown in figures 2.2 to 2.5; the analogous results for hematites are very similar in behaviour. In order to compare with the magnitude of the magnetization assuming only paramagnetism, the curve of paramagnetism for ferrihydrites is included in figure 2.2. Note the great differences in the magnetization scale (y-axis) in these figures.

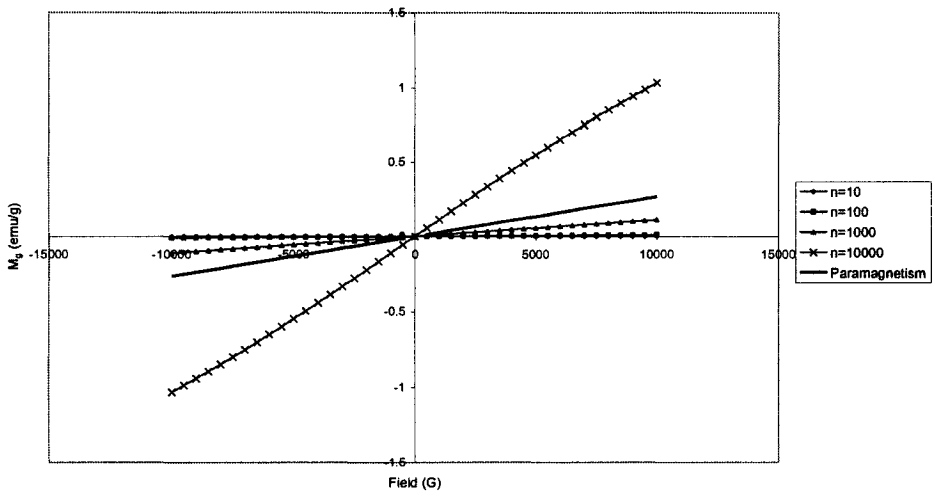

Figure 2.2 Simulation of superparamagnetism for ferrihydrite: μ'=0.01n

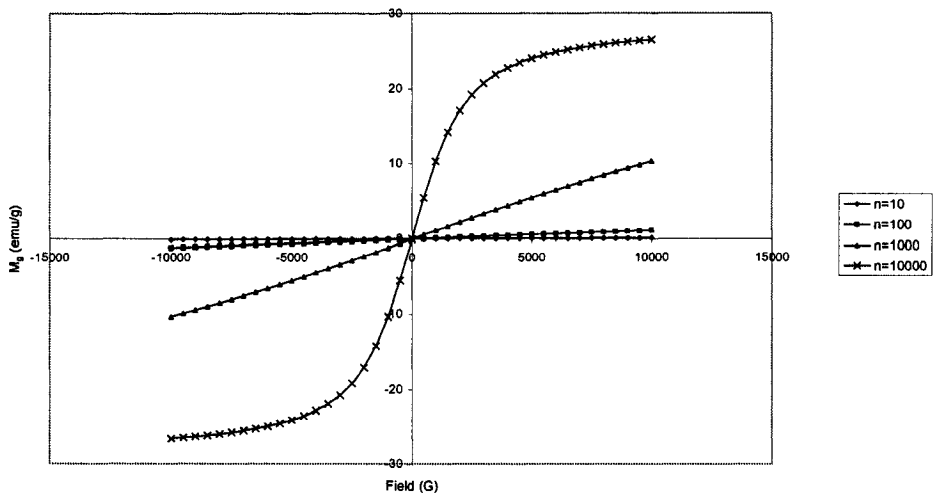

Figure 2.3 Simulation of superparamagnetism for ferrihydrite: μ'=0.1n

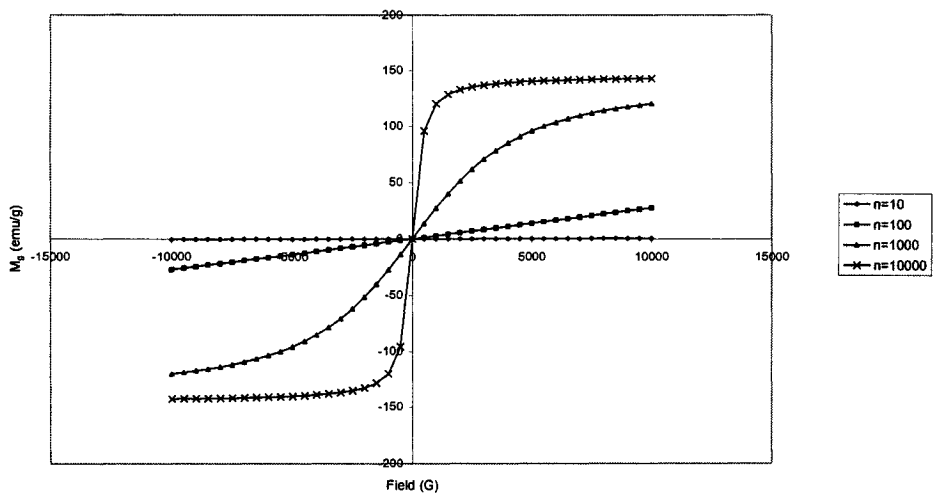

Figure 2.4 Simulation of superparamagnetism for ferrihydrite: μ'=0.5n

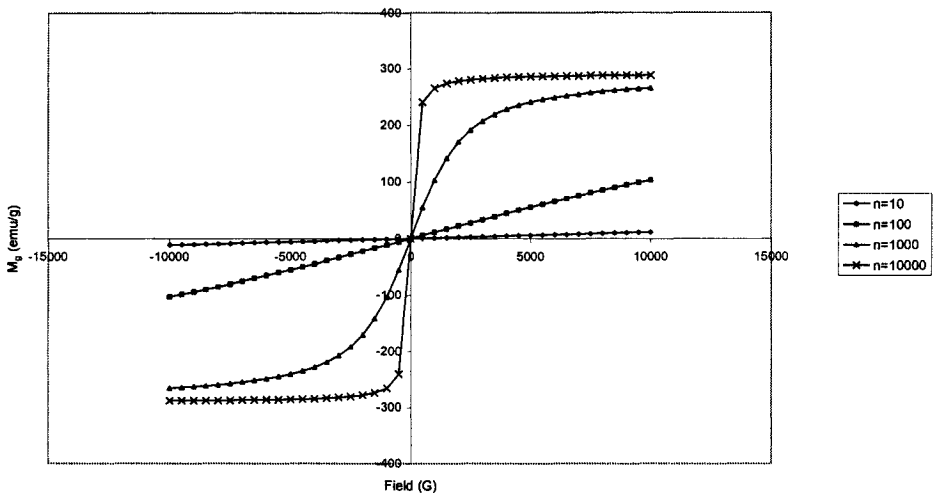

Figure 2.5 Simulation of superparamagnetism for ferrihydrite: μ'=n

Chapter 3 - Exploratory Work

This chapter deals with different magnetic measurements performed on several natural samples with the objective of acquiring a first sense of the results and assessing the information that could be obtained from them. The main idea was to test the limits and advantages of magnetometry in the study of natural samples and allowing the outcome of this initial work model the focus of the thesis project.

The samples considered in this exploratory phase consist of several natural samples: lake sediments, along with a sequential extraction fraction series of these, and Mediterranean sapropel samples. The magnetic properties of these samples were studied through hysteresis cycles (or field cycles) at room temperature and at low temperatures, and through temperature experiments in the range from liquid helium temperature (LHT) to room temperature (RT).

3.1 Lake Sediments and Sequential Extracts

The lake sediments samples considered are from the Perron Lake (Québec, Canada) cores of summer 2001 corresponding to the GSC (Geological Survey of Canada) Metals in the Environment (MITE) Phase-I samples. These samples are: RS-2 and RS-3; they correspond to the second and third centimetre of depth, respectively, from the sediment-water interface. RS-2 and RS-3 also correspond to a peak and a trough in the Fe^{3+}/Fe^{2+} ratio, respectively, obtained by Mössbauer spectroscopy measurements and chemical analyses. Figure 3.1 shows the field cycles at room temperature (RT=22 °C or 295 K) for these

samples. The resultant field cycles are very similar; they both have a saturating curve that may be related to ferrimagnetism with small coercivity and an increasing linear high field region that may be related to paramagnetism and/or superparamagnetism. For a discussion of this type of interpretation, see Rancourt *et al.* (2004).

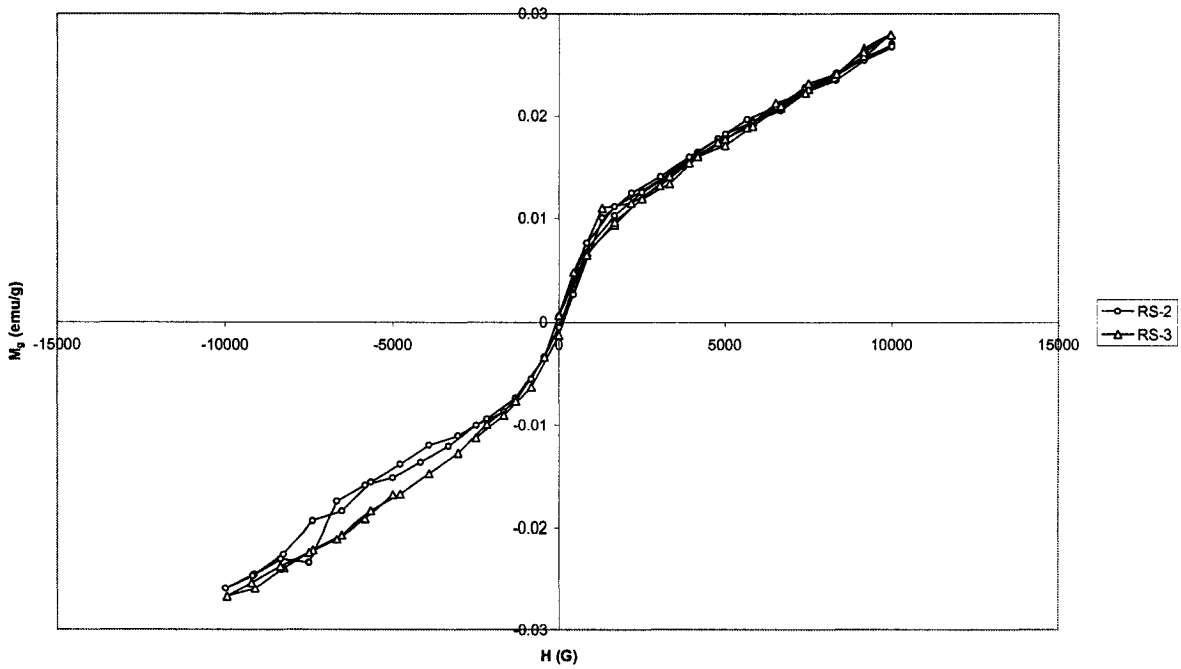

Figure 3.1 Field cycles at RT for lake samples RS-2 and RS-3

In order to test how much difference between natural samples could be resolved using this magnetometry technique, the sequential extraction fraction series from a sample of a homogenized core of sediments from Perron Lake provided by the GSC was run at RT. This series consists of the resultant residues of a sequential extraction procedure done on a homogenized sample (named LEX-21) representative of all the depths within the core. Starting from this sample, a series of successive chemical treatments (leach steps) are

performed; the residue after each leach step is a sample in the sequential extraction series. Table 3.1 indicates the chemical treatment that involved each leach step; table 3.2 indicates the sequential order in which the leach steps were applied, the effect that was being looked for after performing each treatment and the resultant residue after the application of each one of them along with its dry weight.

Leach Name	Procedure
A	20 ml 1.0 M NaO acetate, pH 5.0, 2-hour shake, 2 × 10 ml distilled deionised (DDI) H_2O rinse, dilution factor 1:40
B	40 ml 0.1 M $Na_4P_2O_7$, pH 10.0, 1-hour shake, 2 × 5 ml DDI H_2O rinse, factor 1:50
C	38 ml 0.1 M $Na_4P_2O_7$, pH 10.0, 1-hour shake, no DDI H_2O rinse, factor 1:38
D	30 ml 0.25 M $NH_2OHCHCl$ in 0.25 M HCl, 2-hour bath at 60 °C, 1 × 5 ml DDI H_2O rinse, factor 1:35
E	30 ml 1.0 M $NH_2OHCHCl$ in 25% HO acetate, 3-hour bath at 90 °C, 2 × 5 ml 25% HO acetate rinse, factor 1:40
F	8 ml Aqua Regia (6 ml. HCl : 2 ml HNO_3), ~3-hour bath (1 hour at 90 °C), made to 50 ml with DDI H_2O, rinse factor 1:50

Table 3.1 Leach procedures performed on LEX-21 and sequential residues (GSC, 2001, personal communication)

Sequential Order	Leach Step	Desired Effect	Resultant Residue	Dry Weight (g)
-	None	-	LEX-21 (Original non-treated sample)	0.973
1st	A	Dissolution and removal of adsorbed, exchangeable and carbonate phases	LEX-17	0.821
2nd	B and C	Dissolution of soluble organic phases	LEX-13	0.838
3rd	D	Removal of amorphous iron oxides	LEX-9	0.754
4th	E	Dissolution of crystalline iron oxides	LEX-5	0.770
5th	F	Removal of sulphides, residual organics, oxides and silicates	LEX-1	0.538

Table 3.2 Sequential extraction procedure and resultant residues (GSC, 2001; Dang, 2002, personal communication)

The field cycles at RT for the residues and original sample are shown in figure 3.2; this graph shows the magnetization per mass of sample (or residue) used for the measurement. These magnetization values should be corrected in order to obtain magnetization values per mass of original weight of LEX-21. This correction enables a direct comparison of magnetization values among the samples. The result can be seen in figure 3.3. The obvious off points in the curves are the result of an artifact of the device not resolved at the time of measurement of these samples. The corrected magnetization curves (figure 3.3) are similar in behaviour and moment magnitude to the non-treated lake samples (RS-2 and RS-3) shown in figure 3.1, but they do show more difference in magnetization values among them than do the non-treated lake sediments.

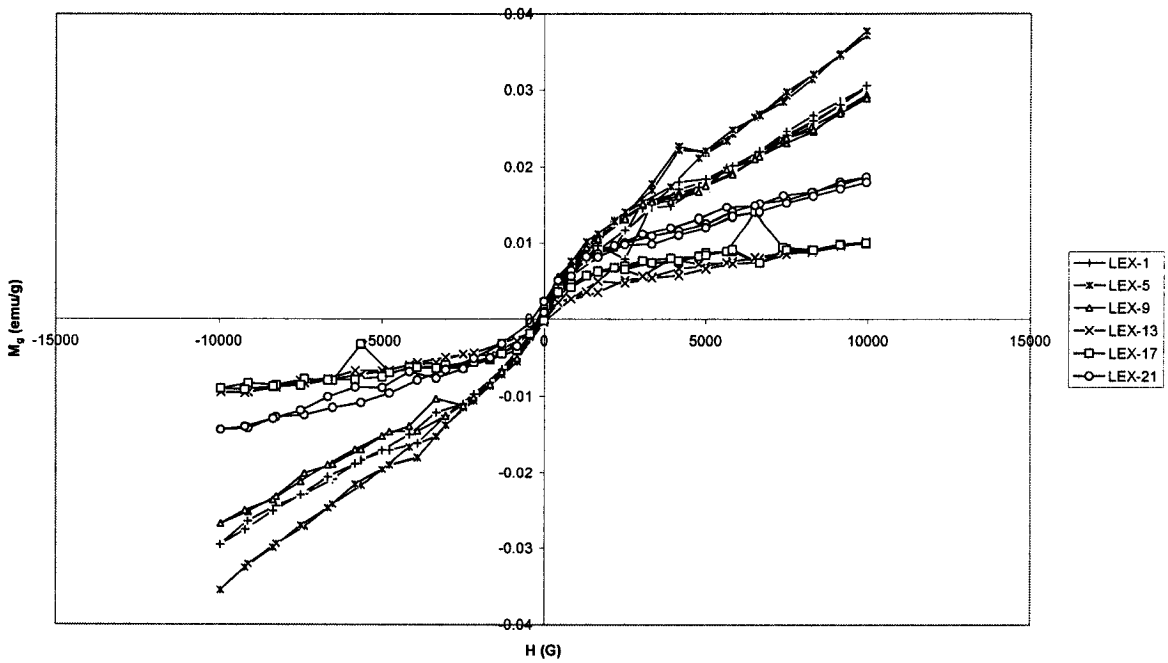

Figure 3.2 Field cycles at RT of sequential extracts not corrected for original weight of LEX-21

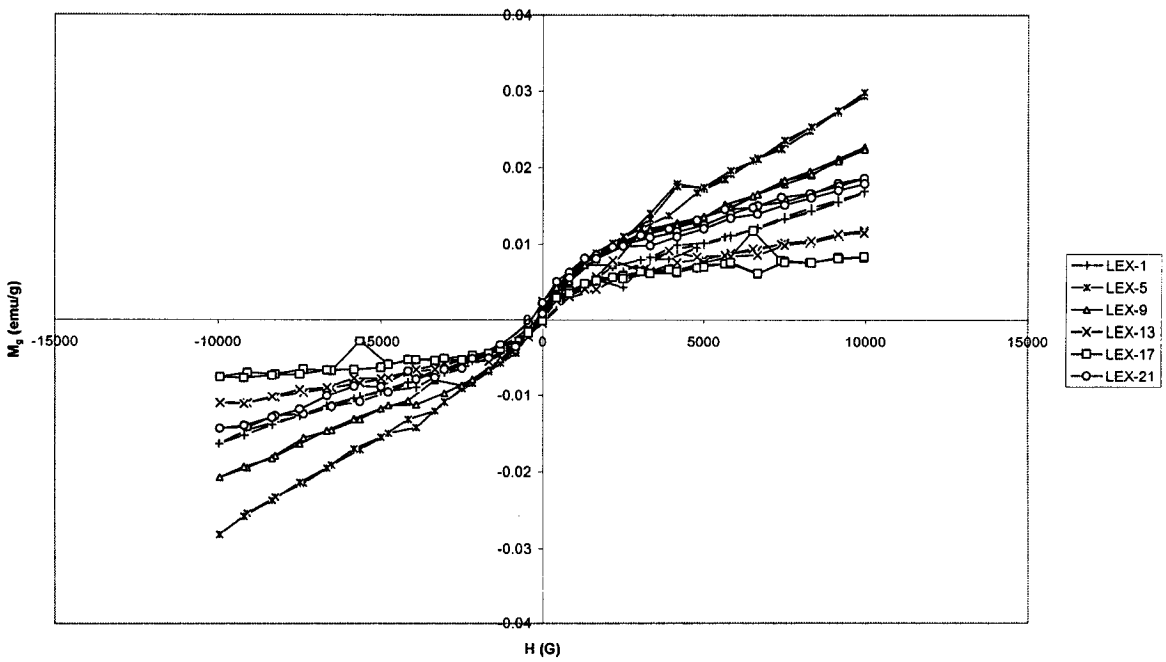

Figure 3.3 Field cycles at RT of sequential extracts showing magnetization per original weight of non-treated sample (LEX- 21)

The sensitivity of the magnetometry results for all the samples shown above was tested by comparing the iron content calculated by chemical analyses with the number of magnetic cations extracted from the field curves. The total iron content had been previously calculated by ICP-ES (inductively coupled plasma emission spectroscopy) for the lake samples RS-2 and RS-3 and by elemental composition analysis for the treated samples (extracts) and the initial non-treated LEX-21. These chemical results are used in the comparison assuming that the total iron in the sample is Fe^{3+}. Following this supposition and assuming that these magnetic cations are in a paramagnetic and in a ferrimagnetic phase, it is possible to calculate the number of cations per unit mass involved in each magnetic phase. In this scenario, the slope in the high field linear region is due to paramagnetism and the extrapolated zero-field saturation magnetization is related to the ferrimagnetism in the sample.

The number of paramagnetic cations is calculated using the measured slope of the linear portion of the curve at high fields (> ± 5 kG). Starting from Curie's law (equation 2-1) the number of paramagnetic species per gram may be expressed as:

$$N = \frac{3k_B T \chi_g}{\mu_B{}^2 p^2} \qquad (3\text{-}1),$$

where:

N is the number of Fe^{3+} cations per unit of mass

χ_g is the mass susceptibility: slope measured

μ_B is the Bohr magneton

p is the effective paramagnetic Bohr magneton number calculated for Fe^{3+} = 5.92

k_B is Boltzmann's constant

T is the temperature in Kelvin: 300 K

The number of ferrimagnetic cations per gram is calculated using the measured spontaneous magnetization (M_s). This measured magnetization is taken as the average of the absolute values of the intercepts of the best-fit lines through the points of the high field linear region (> ± 5 kG). The number of ferrimagnetic cations per unit mass is estimated as:

$$N = \frac{M_S}{p\mu_B} \qquad (3\text{-}2).$$

For all samples considered the number of ferrimagnetic cations estimated was two orders of magnitude smaller than the number of paramagnetic cations estimated. The sum of the calculated paramagnetic cations and the ferrimagnetic cations is compared with the number of Fe^{3+} cations per gram of original weight (Fe^{3+}/g) (i.e., per gram of LEX-21, the original non-treated sample) estimated from previously performed chemical analyses in figures 3.4 and 3.5 for the treated samples and the non-treated samples, respectively.

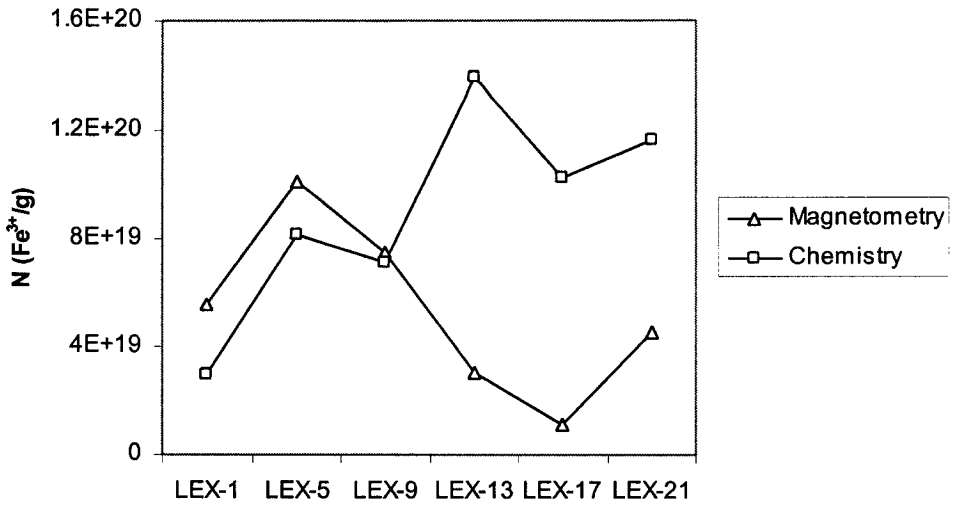

Figure 3.4 Estimation of number of Fe^{3+} cations per gram using magnetometry and chemical analyses for sequential extraction fractions of LEX-21

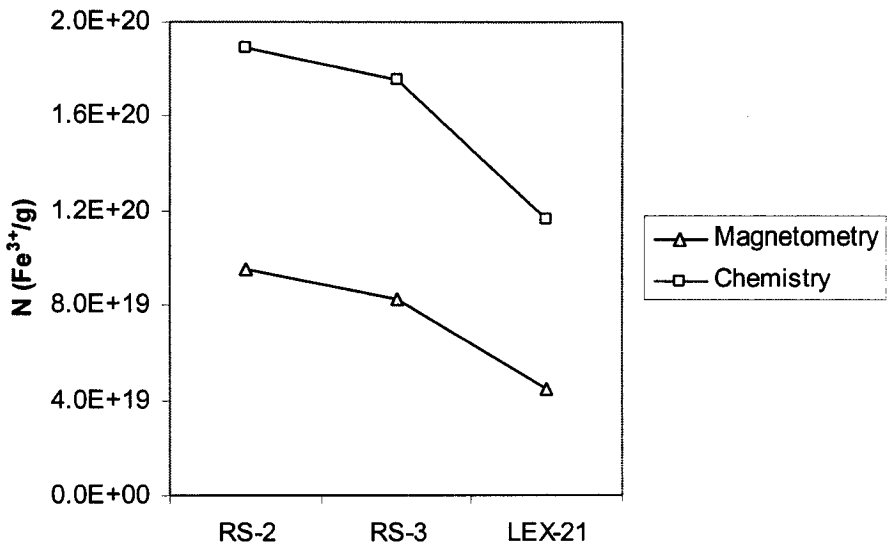

Figure 3.5 Estimation of Fe^{3+} cations using magnetometry and chemical analyses for non-treated lake samples

Figure 3.4 shows that for the last sequential residues (LEX-9, LEX-5 and LEX-1) the estimations done through magnetometry and chemical analyses agree and follow the same trend, however, for the original sample and the first sequential residues (LEX-21; LEX-17 and LEX-13) the estimation done through magnetometry underestimates the results of chemical analyses. In the same way, figure 3.5 shows that for the non-treated sediments, magnetometry is also underestimating the chemical analyses results.

Within the assumed scenario, the results shown in figures 3.4 and 3.5 suggest that for most of the samples, magnetometry is not detecting all the magnetic cations present in the sample. This is expected in a ferrimagnetic structure where the net magnetic moment results from the imperfect cancellation of the magnetic moments in the two antiparallel sublattices; consequently, only the fraction of the moments that is not cancelled is detected. In fact, an example of a situation where only a fraction of the moments is detected is later shown in section 8.2.3 for 2-line ferrihydrite samples where it is suggested that only 2 % of the atomic moments present in their structure are contributing to the measured supermoment of the particle.

The scenario of calculating number of magnetic species assuming superparamagnetism would require a different approach since one could not assume that saturation has been reached for the field strengths used in these measurements and therefore the apparent saturation value would not be indicative of the total number of superparamagnetic species. The recent development of a magnetic granulometry extraction method using hysteresis cycles (Rancourt *et al.*, 2004) could be applied in the future for these

type of samples, assuming a distribution of paramagnetic, ferrimagnetic and superparamagnetic species in the sample.

3.2 Sapropels from the Mediterranean Sea

Four samples from the sapropel unit S1 in the eastern Mediterranean Sea were run through field cycles at RT. The S1 sapropel unit is the most recently formed organic matter-rich layer from the sapropel sequence in this region. The samples are from two cores from different locations in the central region of the eastern Mediterranean. Table 3.3 indicates the location from where these cores were taken. Each core of sediment has a sequence of an oxidized portion of the sapropel and a reduced portion of the sapropel; table 3.4 indicates the depth intervals of these regions within core 1 (core 2 has analogous depth intervals). The samples considered are from each of these regions or portions of the sapropel; table 3.5 indicates the name of the samples and from which core and region they belong to.

Core	Geographical Position	Water Depth
1 (SL114)	35°47.85'N 28°36.50"E	2750 m
2 (BC19)	33°17.241'N 21°24.519'E	3390 m

Table 3.3 Location of cores from the Mediterranean Sea

Sapropel Region	Depth Interval (cm)
Oxidized portion	22.8 – 27.8
Reduced portion	27.8 – 35.8

Table 3.4 Depth intervals of oxidized and reduced portions of sapropel S1 in core 1

Portion of Sapropel	Core 1	Core 2
Oxidized region	O1	O2
Reduced Region	R1	R2

Table 3.5 Names of sapropel samples considered

In general, it has been determined that the reduced zone of this sapropel is rich in iron monosulphides and pyrite and that the oxidized region of the sapropel is rich in iron oxides and iron oxyhydroxides (e.g., Pruysers *et al.*, 1993). Previously performed Mössbauer spectroscopy and powder X-ray diffraction measurements on the samples considered have determined the predominance of nanogoethite as the main diagenetic iron oxyhydroxide (van der Zee *et al.*, 2003) and the relative absence of pyrite and hematite in the samples from the oxidized region. For the reduced region, these measurements have determined the predominance of pyrite and the relative absence of hematite and nanogoethite. Additionally, solid phase geochemistry shows that the reduced zone presents a higher organic matter concentration (up to 8% of the dry weight) than the oxidized zone. (Roberts *et al.*, unpublished).

Figure 3.6 shows the field cycles at room temperatures for these samples. These curves show a small coercivity ferrimagnetic component and/or a superparamagnetic component with a high field linear region that could be due to paramagnetism. The samples that are in the oxidized region of the sapropel layer (O1 and O2) show higher values of magnetization than the samples that are in the reduced portion of the sapropel (R1 and R2). The higher content of organic matter in the current sapropel would not affect the magnetic response of minerals in this region, since this response is directly affected by the presence of iron minerals.

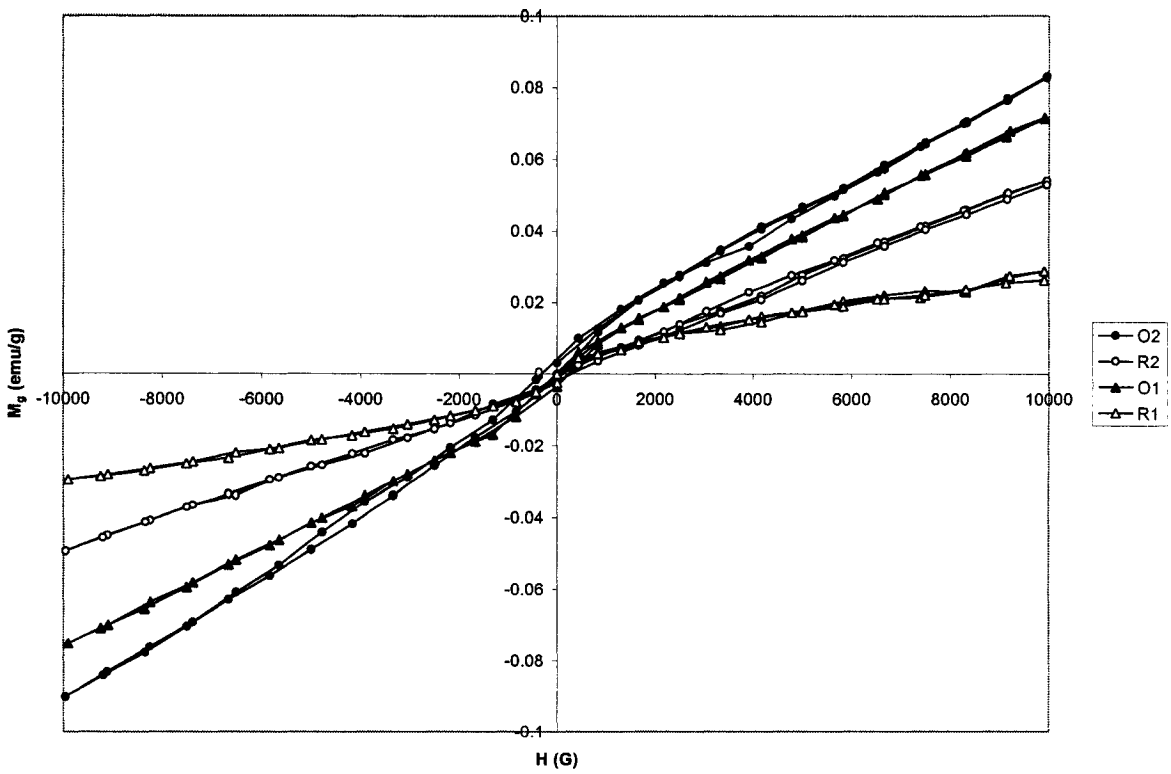

Figure 3.6 Field cycles at RT for sapropel samples

The graph in figure 3.6 suggests a positive correlation between the predominance of nanogoethite and the magnetization values reached and a negative correlation with the predominance of pyrite. The samples from the oxidized region have a maximum concentration of nanophase goethite (nanogoethite), which is a superparamagnetic mineral due to the small size of its particles. Thus, the magnetization in this region is mainly due to the predominance of superparamagnetic minerals and the presence of paramagnetism from minerals such as silicate phases and diagenetic clay minerals that are common in sediments. The samples from the reduced region present a minimum concentration of nanophase oxides and a maximum concentration of pyrite, which is a non-magnetic mineral. Thus, the minimum presence of superparamagnetic minerals, the predominance of a non-magnetic mineral as well as the presence of other paramagnetic minerals common in sediments determines the magnetization in this region. Consequently, it can be said in a general way, that samples from the oxidized region (rich in iron oxides and oxyhydroxides such as nanogoethite) have higher magnetization values than samples from the reduced region of the sapropel (rich in iron sulphides, such as pyrite). Nevertheless, the quantification and detailed characterization is not straightforward with RT measurements due to the heterogeneity in these samples. For this reason, the next section considers results from performing low temperature measurements on this type of samples.

3.3 Low Temperature Magnetization Measurements

Several iron oxides (e.g., hematite, magnetite) and iron sulphides (e.g., pyrrhotite) have magnetic transitions that are observed when the temperature is lowered to liquid helium

temperature (LHT = 4.2 K) (Cornell and Schwertmann, 1996; Torii *et al.*, 1996). A measurement of magnetic moment versus temperature in a constant applied field is useful for observing these transitions. Consequently, this type of measurement was performed on some of the previously studied samples in order to investigate the possible presence of certain iron oxides and iron sulphides. Additionally, the lowering of temperature could enable the magnetic blocking of superparamagnetic species, and therefore their presence can be detected.

The samples considered for these studies are the sapropel samples O1 and R1 and the lake sample RS-2. Figures 3.7 and 3.8 show the field cycles at 4.2 K for RS-2 and sapropels (O1, R1), respectively. These graphs show field curves that have a broad curvature through the whole field range that was not present in the RT curves and much higher magnetization values (figures 3.1 and 3.6). These changes on going to low temperatures suggest the presence of superparamagnetic species that give a larger magnetic response at low temperatures.

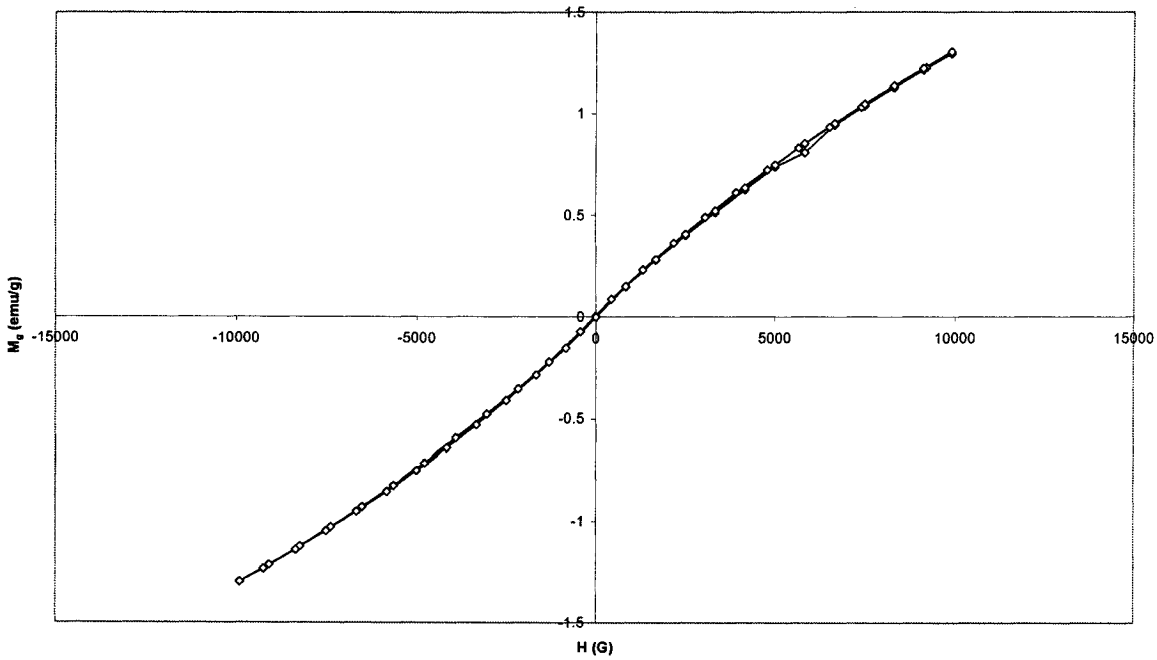

Figure 3.7 Field cycle of RS-2 at 4.2 K

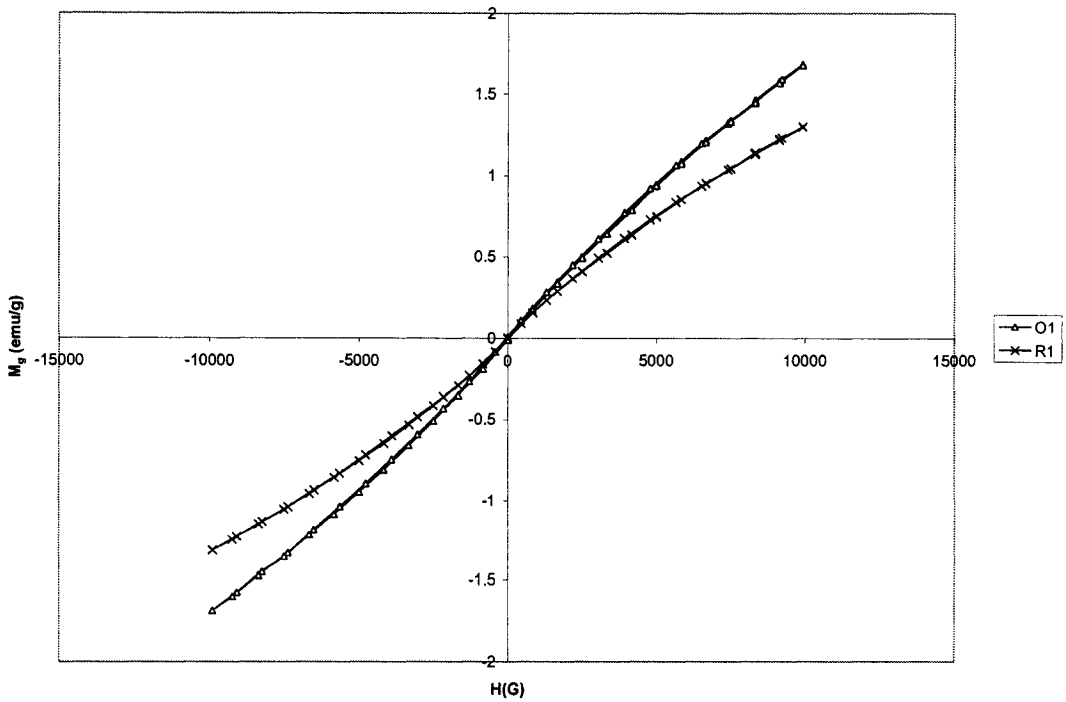

Figure 3.8 Field cycles of O1 and R1 at 4.2 K

Figure 3.9 shows the temperature run (mass magnetization versus temperature) on heating from LHT (4.2 K) to RT (300 K) for the sapropel samples; there is no observable transition or sudden change of magnetic moment through the whole range of temperature. The lack of any transition is also shown for sample RS-2 in figure 3.10 for the heating curve (from LHT to RT) and for the cooling curve (from RT to LHT). These results rule out the presence of pyrrhotite, and any hematite with a Morin transition or magnetite with a Verwey transition, but they do not rule out the presence of hematites or magnetites that have a magnetic transition suppressed below 4.2 K due to chemical and crystalline defects.

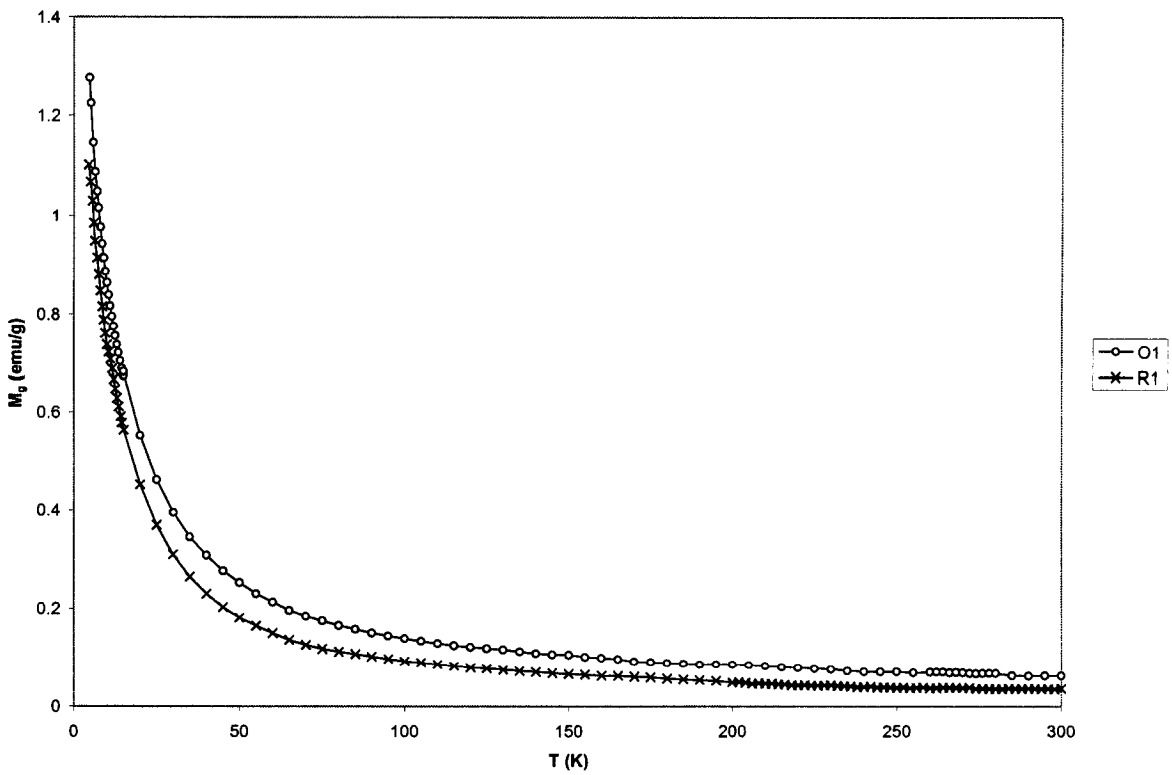

Figure 3.9 Temperature run of O1 and R1 from LHT to RT

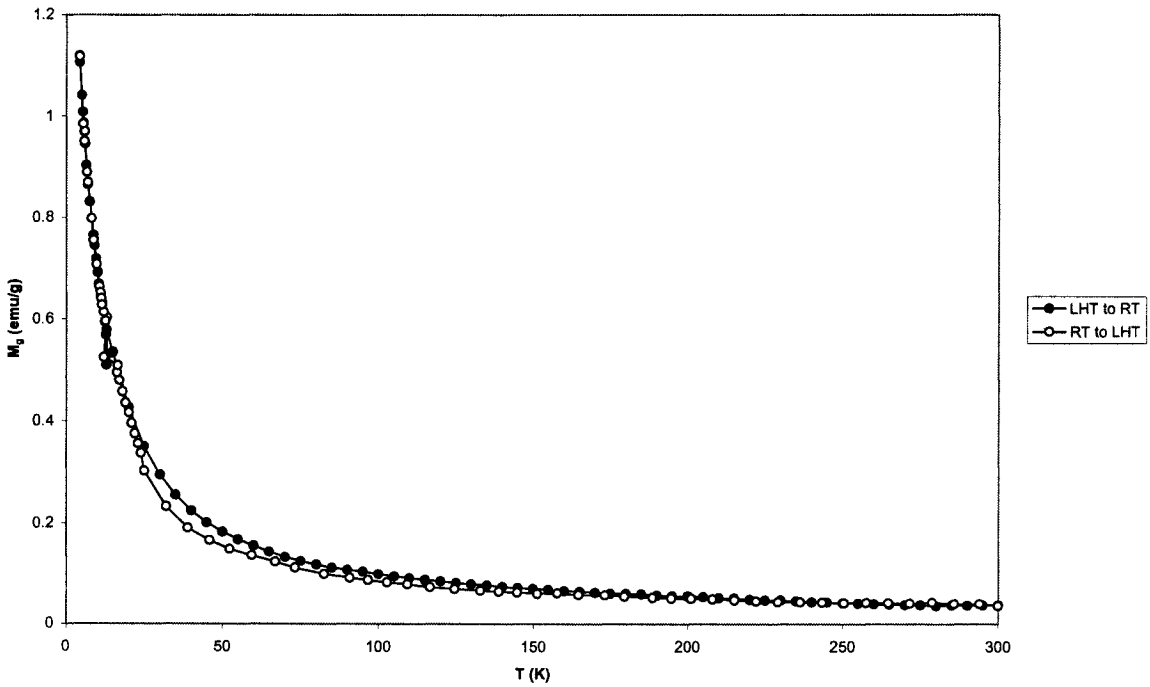

Figure 3.10 Temperature run of RS-2 from LHT to RT and back to LHT

3.4 Concluding Remarks

The magnetometry results shown in this chapter give insight into the complexity of the magnetism commonly present in natural samples. These types of samples could be constituted of a mixture of minerals with different magnetic properties. Nevertheless, the exploration done with these natural samples has given a good idea of the kind of information that magnetic measurements can provide and it shows that magnetometry is a very sensitive technique for the study of many common earth and planetary materials. This exploratory work strongly suggests that there is a need to study these materials through their magnetic properties when they are not mixed with different phases. In this sense, the study of

controlled synthetic samples of minerals that would be common in natural environments becomes necessary and pertinent. This is the fundamental proposition that these initial results give for the development of this thesis project. Thus, the samples selected to be the focus of this thesis are synthetic iron oxides and synthetic iron oxyhydroxides, described in the following chapter on sample synthesis and characterization (chapter 4).

Chapter 4 - Sample Synthesis and Characterization

The samples that are the focus of this thesis comprise a set of synthetic microcrystalline iron oxides, synthetic nanophase iron oxides and synthetic nanophase iron oxyhydroxides. The synthesis conditions of these samples are well known and they have been characterized through different techniques therefore they constitute a set of controlled samples which can be used to study possible variations of magnetic properties, and derived information, with known characteristics of the samples.

The microcrystalline iron oxides are hematite-like materials which are going to be referred as "microcrystalline hematites" throughout this thesis. The nanophase iron oxides are a set of samples initially considered as "nanohematite" samples and consequently they are referred as such throughout the whole text. The nanophase iron oxyhydroxides samples comprise a group of 2-line and 6-line ferrihydrites and as a group they are referred as "ferrihydrites". The following sections describe these samples and the previous characterizations performed on them.

4.1 Microcrystalline Hematites

The group of microcrystalline hematite samples constitute a set of synthetic hematite-like materials that cover a wide range of proportion of defects, anionic synthesis, impurities, structural OH^- groups and H_2O molecules in their composition. The general structural formula for these samples, excluding surface complexed anionic impurities (sulphate, nitrate or chloride), is: (Dang *et al.*, 1998)

$$Fe_{(2-x/3)}\square_{(x/3)}O_{(3-x)}(OH)_x \cdot bH_2O \qquad (4\text{-}1).$$

In this formula, □ represents a vacancy and the parameters *x* and *b* are reduced when an OH^- and vacancy loss repair mechanism, such as the thermal treatment by annealing, is applied to the sample. In this sense, a series of samples annealed at temperatures: 400 °C and 600 °C is also considered within the group of samples. In addition, a pure bulk hematite (PBH) sample was made by annealing a synthetic commercial hematite sample at high temperatures (~1000 °C). This process of annealing at such a high temperature assures that the resultant sample has a defect-free and repaired crystalline structure with a stoichiometry of pure hematite (Fe_2O_3) (Dang *et al.*, 1998).

4.1.1 Synthesis

The samples were received from J.E. Dutrizac of the Canadian Centre for Mineral and Energy Technology (CANMET); the synthesis was done by hydrothermal precipitation from different solutions at different synthesis temperatures as indicated in table 4.1.

Sample Name	Initial Solution	Synthesis Temperature (°C)
L1	$FeSO_4$	160
L3	$FeSO_4$	180
L7	$FeSO_4$	220
L9	$FeSO_4$	240
L10	$FeSO_4$	250
H1	$Fe(NO_3)_3$	150
H2	$Fe(NO_3)_3$	200
H3	$FeCl_3$	150
H4	$FeCl_3$	130
H5	$Fe(SO_4)_{1.5}$	210
M60	$Fe(SO_4)_{1.5}$	220
G12	$Fe(SO_4)_{1.5}$ and H_2SO_4	225

Table 4.1 Synthesis conditions of microcrystalline hematite samples

The annealed samples were made from sample M60 which was prepared by Dr. M. Z. Dang at the University of Ottawa, previous to this work; one portion was annealed at 400 °C and another portion at 600 °C. The resultant annealed samples are named: M60-400 and M60-600, respectively. Additional information on the synthesis of most of the microcrystalline hematite samples is given by Dang *et al.* (1998).

4.1.2 Sample Characterization

Many measurements have previously been performed on the microcrystalline hematites by several other researchers; table 4.2 indicates with an "X" the studies that have been performed on these samples. As can be seen in this table, sample M60-600 of the annealed series was not studied through pXRD or SQUID magnetometry; however, other samples (not included in this study) that were annealed from the same M60 as-synthesized sample, at temperatures 550 °C and 674 °C were studied through these techniques. Thus, the

data used for M60-600 is the range of values obtained for M60 annealed at 550 °C and M60 annealed at 674 °C. Additionally, the sample PBH was not studied using most of the techniques because it does not need further characterization, since the annealing process to which it was put under assures that the resultant sample is pure bulk hematite, as demonstrated by Dang *et al.* (1998). In summary, the studies performed on the samples are:

- Wet chemical analyses, which give elemental compositions per dry sample weight;
- Weight loss measurements performed by weighing the samples after various thermal treatments;
- Powder X-ray diffraction (pXRD) using CuKα radiation, which confirms that the mineral phase present is hematite for all samples and gives information about any other impurity present (table 4.3). Figure 4.1 shows the X-ray diffractogram of M-60, which represents a typical diffractogram for the microcrystalline hematites. The pXRD data allowed the estimation of the mean particle sizes of the samples assuming a tetragonal cell; the results can be seen in table 4.3 (Dang *et al.*, 1998 and unpublished).
- Super quantum interference device (SQUID) magnetometry, which gives magnetic information including the presence or not of a Morin transition down to 4.2 K (table 4.3) (Dang *et al.*, 1998 and unpublished).
- Room temperature ^{57}Fe Mössbauer spectroscopy (RT MS) and low temperature ^{57}Fe Mössbauer Spectroscopy (LT MS), which resolve, among other things, the magnetic structure state;
- Elemental analysis by gas chromatography (GC), which gives concentration of light elements (C, N, H, S);

- Scanning electron microscopy (SEM), which shows the size and shape of particles or aggregates down to a resolution of 0.1 μm;
- Thermogravimetric analysis and differential thermal analysis (TGA-DTA), which give information about temperature-dependant weight loss, type of heat-induced reactions and reaction kinetics.

Sample	Chemistry	Weight Loss	pXRD	RT MS	LT MS	GC	SEM	SQUID	TGA-DTA
L1	X	X	X	X	X	X	X	X	X
L3	X	X	X	X	X	X	X	X	X
L7	X	X	X	X	X	X	X	X	X
L9	X	X	X	X	X	X	X	X	X
L10	X	X	X	X	X	X	X	X	X
H1	X	-	X	X	-	X	-	X	X
H2	X	-	X	X	-	X	-	X	X
H3	X	-	X	X	-	X	-	X	X
H4	X	-	X	X	-	X	-	X	X
H5	X	-	X	X	-	X	-	X	X
M60	X	X	X	X	X	X	X	X	X
M60-400	X	X	X	X	X	X	X	X	-
M60-600	X	X	-	X	-	X	-	-	-
G12	X	X	X	X	X	X	X	X	X
PBH	-	-	X	-	-	-	-	-	-

Table 4.2 Previous studies performed on the microcrystalline hematite samples

Sample	pXRD results	Particle Size (Å)	Morin Transition
L1	Fe_2O_3 + trace FeOOH (goethite)	900	No
L3	Fe_2O_3 + trace FeOOH (goethite)	1000	No
L7	Fe_2O_3 + faint trace (~0.25%) $FeSO_4OH$	2500	No
L9	Fe_2O_3	1500	No
L10	Fe_2O_3	2500	Yes
H1	Fe_2O_3	500	Yes
H2	Fe_2O_3	800	Yes
H3	Fe_2O_3	200	No
H4	Fe_2O_3	200	No
H5	Fe_2O_3	700	No
M60	Fe_2O_3	300	No
M60-400	Fe_2O_3	400	No
M60-600	Fe_2O_3	400-680	Yes
PBH	Fe_2O_3	-	Yes
G12	Fe_2O_3 + minor $FeSO_4OH$	1100	Yes

Table 4.3 pXRD results and detection of Morin transition for the microcrystalline hematite samples as reported by Dang *et al.* (1998 and unpublished)

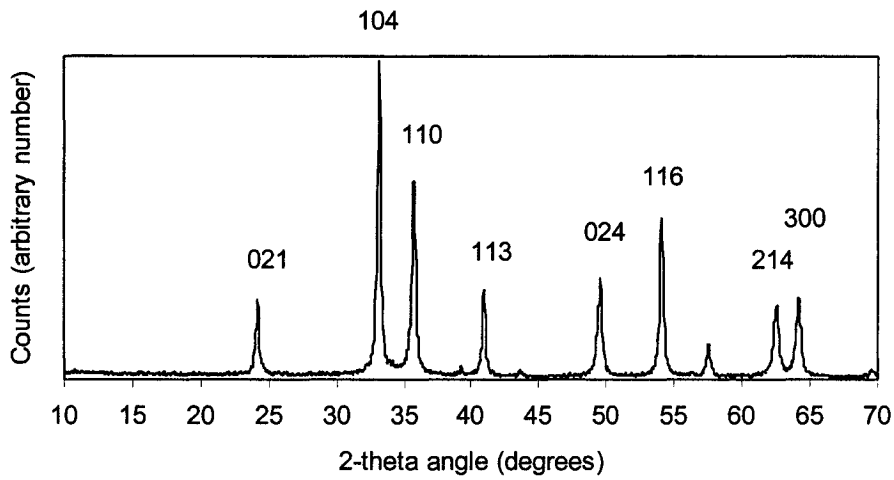

Figure 4.1 X-ray diffractogram of M-60 showing the Miller indices for the main diffraction peaks. (Dang *et al.*, 1998)

4.2 Ferrihydrites

4.2.1 Synthesis

The group of synthetic ferrihydrite samples comprises one 6-line ferrihydrite (FH-6L) and four nominally 2-line ferrihydrites (FH-2L series) precipitated from different solutions. Table 4.4 shows the initial solution of precipitation for all of these samples and further description of the synthesis procedure is given below.

Name	Initial Solution
FH-6L	$Fe(NO_3)_3$
FH-2L-N1	$Fe(NO_3)_3$
FH-2L-N2	$Fe(NO_3)_3$
FH-2L-S	$Fe(SO_4)_{1.5}$
FH-2L-N3-P	$Fe(NO_3)_3 + NaH_2PO_4 \cdot H_2O$

Table 4.4 Initial solution of precipitation for the ferrihydrites (Thibault, 2003, personal communication)

The 6-line ferrihydrite (FH-6L) was received from Steeve Bonneville from Utrecht University. This sample was synthesized following the recipe for 6-line ferrihydrite suggested by Cornell and Schwertmann (1996, p.491). In this synthesis procedure, 2 litres of distilled water are heated in an oven at 75 °C and 20 g of unhydrolyzed crystals of $Fe(NO_3)_3 \cdot 9H_2O$ are added stirring rapidly. This solution is put into the oven and left there for approximately 10 minutes during which the Fe hydroxyl-polymers are formed, but still there is no precipitation. The solution is then cooled in a forced way by plunging into ice water; after this, it is transferred to a dialysis bag and dialysed for at least three days, changing the water daily several times; finally, the suspension is freeze-dried.

The 2-line ferrihydrite samples were synthesized at CANMET by Pierre Jean Thibault (LSSE member). All of these samples were synthesized through the following procedure using the initial solution indicated in table 4.4. A concentration of 0.1 M of the initial iron salt solution (and an additional 0.01 M of sodium phosphate for FH-2L-N3-P) was maintained at 60 °C during the addition of NaOH in order to induce precipitation. The pH was increased from a starting value ranging from 1.0 to 1.9, to the end value 4.0 at a constant controlled rate of addition of NaOH (8 M concentration) of 1.1 mL/min. When the pH 4.0 was reached, it was maintained for two hours approximately (1 hour for FH-2L-N3-P) while the reaction continued, under constant agitation and oxic conditions. The sample was filtered under vacuum, rinsed with distilled water and filtered under vacuum again (except for FH-2L-N3-P, which was not rinsed).

FH-2L-N2 presents the same initial solution and synthesis conditions as FH-2L-N1, but a different brand name of filter was used, which is suspected to have been incorporated into the sample in a small proportion.

4.2.2 Sample Characterization

The studies previously performed on the ferrihydrites are listed in table 4.5. They include many of the measurements performed on the microcrystalline hematite samples, with the exception of gas chromatography, which for these samples does not include the concentration of sulphur.

Sample	pXRD	RT MS	LT MS	GC	TGA-DTA
FH-6L	X	X	X	X	X
FH-2L-N1	X	X	X	X	X
FH-2L-N2	X	X	X	X	X
FH-2L-N3-P	X	X	X	X	X
FH-2L-S	X	X	X	X	X

Table 4.5 Studies previously performed on the ferrihydrite samples

The X-ray diffractograms for all the ferrihydrites are shown in figures 4.2 through 4.6, and the summary of the results are presented on table 4.6. The X-ray pattern for FH-6L shows the Miller indices associated with each of the main broad peak reflections (Cornell and Schwertmann, 1996). Many of the samples referred as 2-line ferrihydrites show more than two broad peaks in the X-ray pattern and a degree of similarity with the six-line ferrihydrite, therefore, they could have an associated crystallinity in between that of actual 2-line ferrihydrites and 6-line ferrihydrites; however, the samples referred as 2-line ferrihydrites presented seem to be more similar to 2-line ferrihydrites than to 6-line ferrihydrites. In fact, the 2-line ferrihydrite samples show a clear difference in their DTA curves that differentiates them from FH-6L (figure 4.7). Consequently, they will be referred as 2-line ferrihydrites in order to distinguish them from the 6-line ferrihydrite sample considered. The sharp peak shown for FH-2L-N2 and FH-2L-N1 is probably associated to the transformation to hematite and is characteristic of ferrihydrites synthesized from a ferric nitrate solution. (Jambor and Dutrizac, 1998).

The X-ray diffractogram for FH-2L-N3-P shows additional lines associated with the salt ($NaNO_3$) that was formed during precipitation and that was not extracted from the sample through rinsing. The phosphate co-precipitated during the synthesis is believed to

have been incorporated into the ferrihydrite structure since a series of these types of samples with increasing concentration of sodium phosphate in the initial solution (not included in this study) show a gradual change in the X-ray diffractogram, suggesting a major structural change with increasing concentration of sodium phosphate (Thibault, 2003, unpublished).

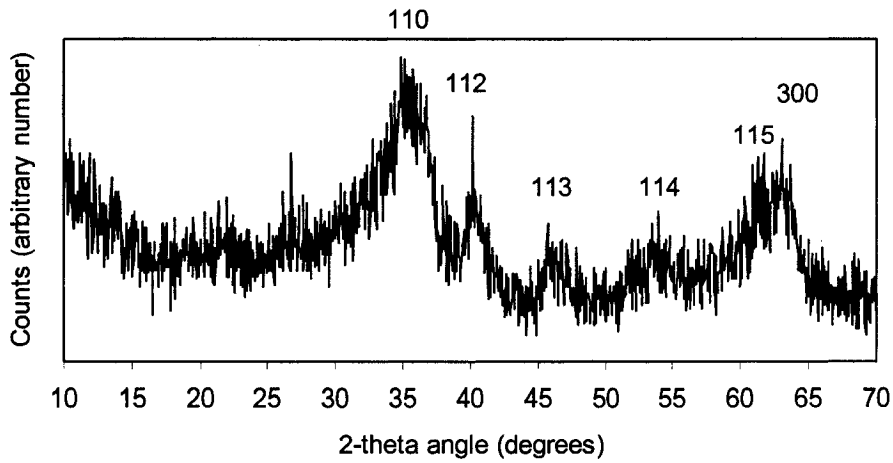

Figure 4.2 X-ray diffractogram of FH-6L

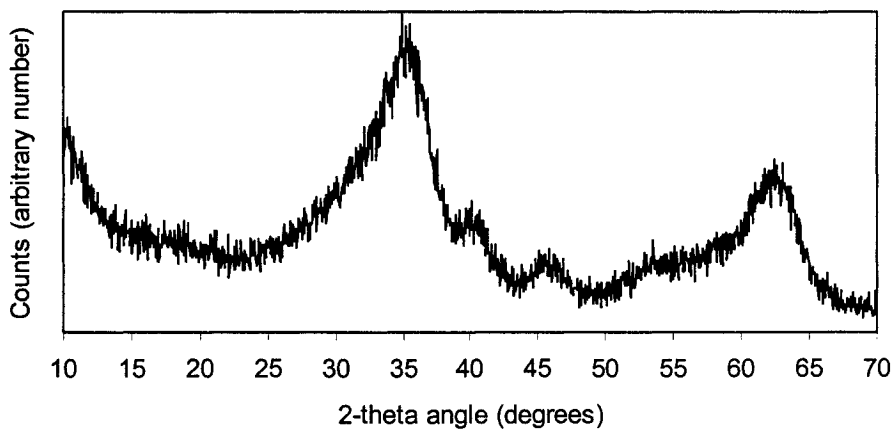

Figure 4.3 X-ray diffractogram of FH-2L-N1

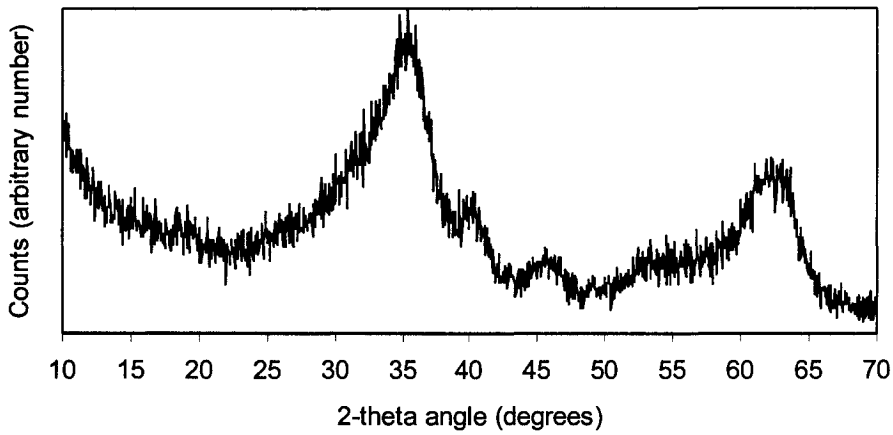

Figure 4.4 X-ray diffractogram of FH-2L-N2

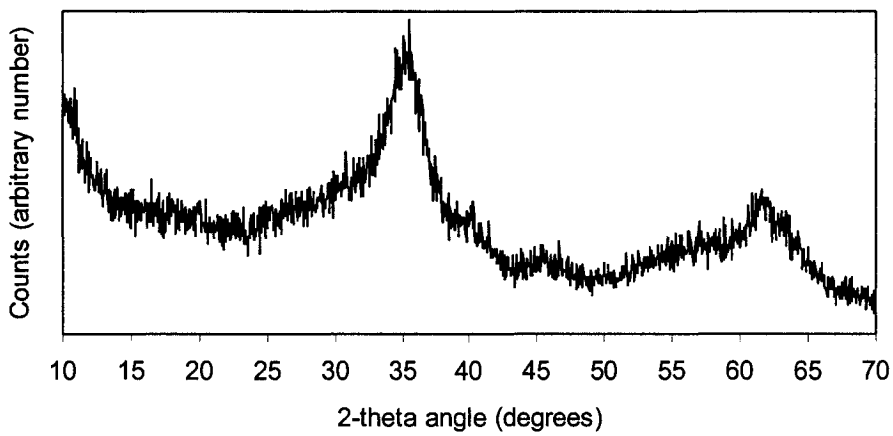

Figure 4.5 X-ray diffractogram of FH-2L-S

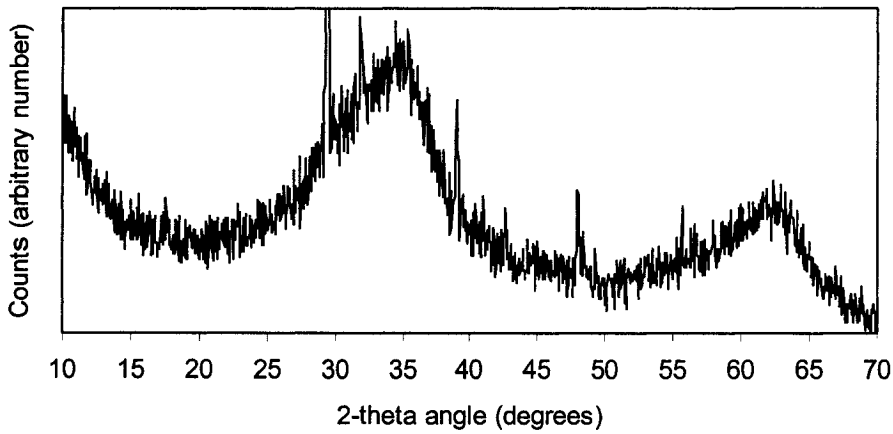

Figure 4.6 X-ray diffractogram of FH-2L-N3-P

Sample	pXRD Results
FH-6L	Ferrihydrite
FH-2L-N1	Ferrihydrite
FH-2L-N2	Ferrihydrite
FH-2L-S	Ferrihydrite
FH-2L-N3-P	Ferrihydrite +$NaNO_3$

Table 4.6 pXRD results for the ferrihydrites

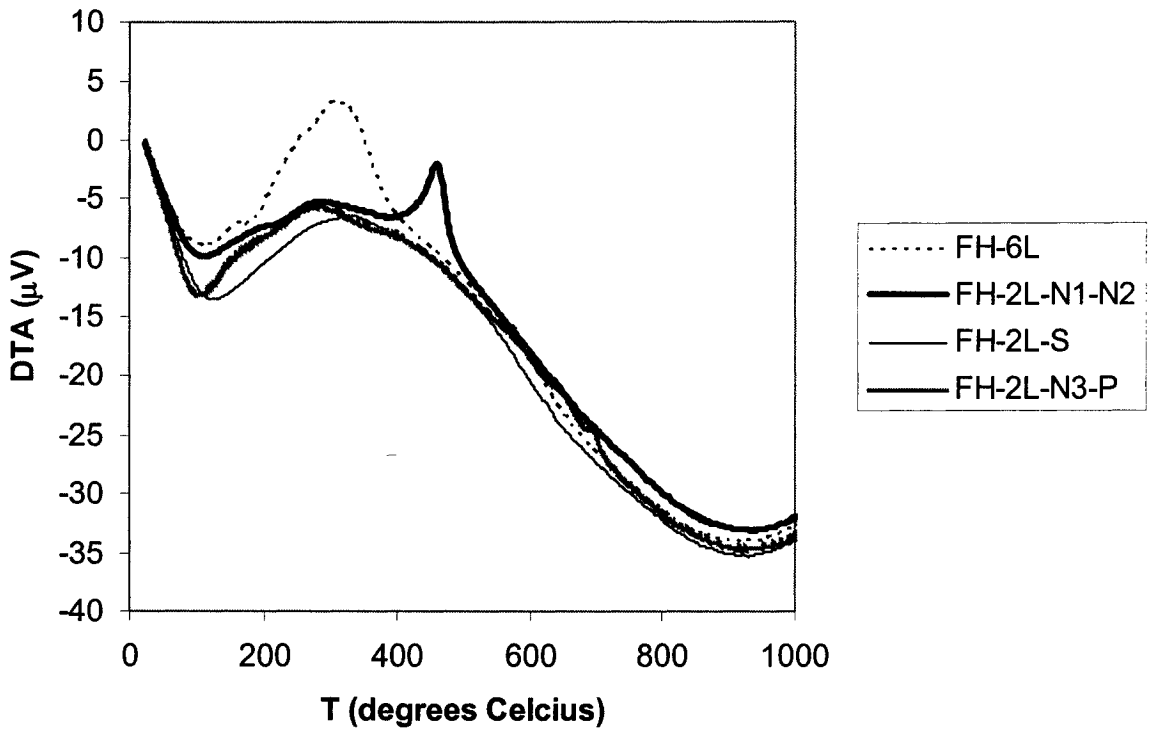

Figure 4.7 DTA curves for the ferrihydrites. FH-2L-N1 and FH-2L-N2 have the same curve

The weight loss curve from TGA analysis of FH-2L-S shows a sudden weight loss at approximately 600 °C (figure 4.8). A similar weight loss of adsorbed sulphur was observed for the microcrystalline hematite sample M60 (Dang *et al.*, 1998), which was also precipitated from a ferric sulphate solution therefore suggesting the presence of adsorbed sulphur in FH-2L-S.

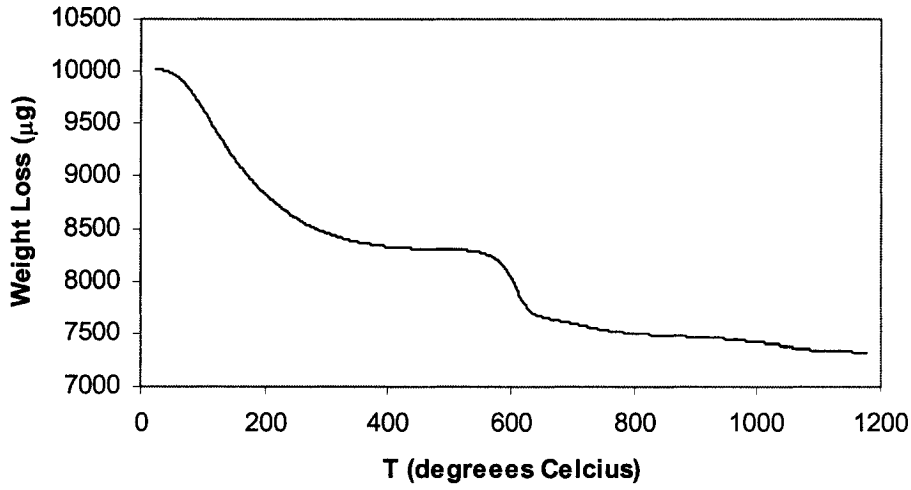

Figure 4.8 Temperature-dependent weight loss of FH-2L-S

4.3 Nanohematites

4.3.1 Synthesis

The nanohematites were received from Thilo Behrens, Steeve Bonneville and Philippe van Cappellen of Utrecht University. All four nanohematites were synthesized following the same procedure. This procedure consists of adding a $Fe(NO_3)_3$ solution to heated water with a rate of 3 ml/min; after this was added the heater was turned off and the suspension was cooled to room temperature without forced cooling. When room temperature was reached the suspension was filled into a dialysis tube; one litre of suspension in a dialysis tube was put into four litres of water with a pH of 4 (adjusted with HNO_3). The water was exchanged every two days; this was repeated until the pH in the water became constant; the suspension was freeze-dried.

4.3.2 Sample Characterization

The studies previously performed on the nanohematites samples by researchers at the University of Ottawa and other collaborators are summarized in table 4.7.

Sample	pXRD	RT MS	LT MS	GC	SQUID	TGA-DTA
NH-1	X	X	-	X	X	X
NH-2	X	X	-	X	-	X
NH-3	X	X	-	X	-	X
NH-4	X	X	X	X	X	X

Table 4.7 Previous studies performed on nanohematite samples

The pXRD results and the estimated particle sizes from this data are shown in table 4.8; two of the nanohematites (NH-3 and NH-4) present quartz (SiO_2) impurities presumably from the holder that contained the samples, and all four "nanohematites" samples were found to present 6-line ferrihydrite. Figure 5.2 shows the X-ray diffractogram for NH-2, which represents a typical diffractogram for all the other samples, except for the additional quartz impurity diffraction lines in samples NH-3 and NH-4. When comparing the diffraction pattern of nanohematite (figure 4.9) with that of a microcrystalline hematite (figure 4.1) it can be seen that the intensities of the first and second most intense diffraction peaks in the microcrystalline hematite, (104) and (110), respectively, are inverted in the nanohematite diffraction pattern, in that the reflection (110) becomes the most intense. This suggests that there is another mineral present that is affecting the diffraction pattern of nanohematite. 6-line ferrihydrite has a diffraction pattern with the most intense broad peak corresponding to the (110) reflection as shown in section 4.2.2, figure 4.2, therefore 6-line ferrihydrite might be contributing to the intensities and to the observed peak broadening in these nanohematite

samples. In addition, the weak broad peak in figure 4.9 observed at a two-theta angle of approximately 47° does not correspond to any peak for hematite, instead, it corresponds to the broad peak in the 6-line ferrihydrite pattern with Miller indices (113) (figure 4.2). This confirms the presence of 6-line ferrihydrite in these samples and it suggests that the amount present is smaller than that of actual nanohematite.

Sample	pXRD Results	Particle Size (Å)
NH-1	Fe_2O_3 + 6-line Ferrihydrite	81 (19)
NH-2	Fe_2O_3 + 6-lineFerrihydrite	78 (23)
NH-3	Fe_2O_3 + 6-line Ferrihydrite + trace SiO_2	85 (20)
NH-4	Fe_2O_3 + 6-line Ferrihydrite + trace SiO_2	90 (20)

Table 4.8 pXRD results for the nanohematite samples

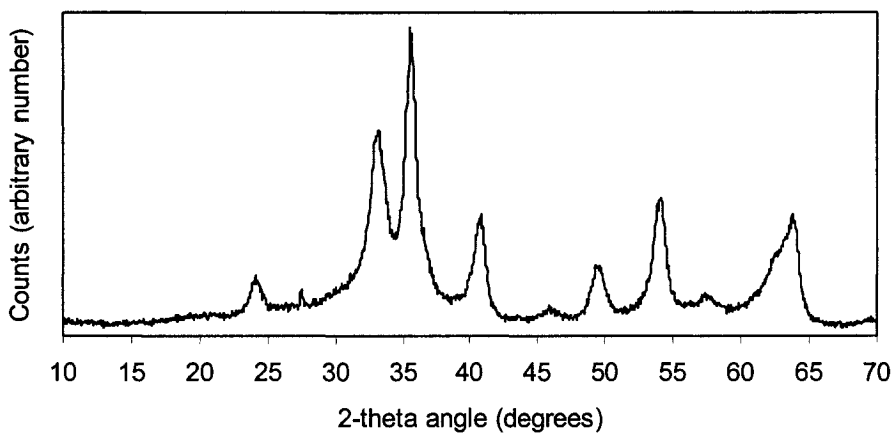

Figure 4.9 X-ray diffractogram of NH-2

The results from other studies performed on these "nanohematite" samples are in agreement with the interpretation that these samples are actually a mixture of nanohematite and 6-line ferrihydrite. The RT MS spectra of the four nanohematites show the superposition

of two signals. Figure 4.10 shows the spectrum for NH-1; one of the signals is a doublet which corresponds to superparamagnetic 6-line ferrihydrite; the other signal is what can be interpreted as a partially developed magnetic hyperfine sextet that is representing a nanohematite with its blocking temperature near RT, as seen with the small measurement time ($\sim 10^{-8}$ sec) of ^{57}Fe Mössbauer spectroscopy. It is not a well developed magnetic hyperfine field sextet as can be seen from comparisons with other signals modelled for various magnetic behaviours (Rancourt, 1998).

Yet another study supporting the two-phase mixture nature of the nanohematite samples considered in this study is the differential thermal analysis (DTA). The DTA curves of these samples and the 6-line ferrihydrite are very similar, and at the same time, both of them are different to the curve corresponding to hematite; this is clearly shown with specific samples in Figure 4.11. This figure shows the DTA curves for a microcrystalline hematite sample (G12) and the curves corresponding to NH-2 and the 6-line ferrihydrite (FH-6L); the curve for hematite does not present any noticeable exothermic feature (peak); the curve for 6-line ferrihydrite presents an exothermic feature that consists of two peaks centered at 260 °C and 300 °C with a sum total width at half maximum of 120 °C approximately, which is not present in the 2-line ferrihydrites considered in this thesis. The DTA curve for NH-2 presents a very similar exothermic feature consisting of two peaks with approximately the same positions and sum total width at half maximum. Consequently, these results are in agreement with the idea that the "nanohematite" samples considered in this study are a mixture of nanohematite and 6-line ferrihydrite.

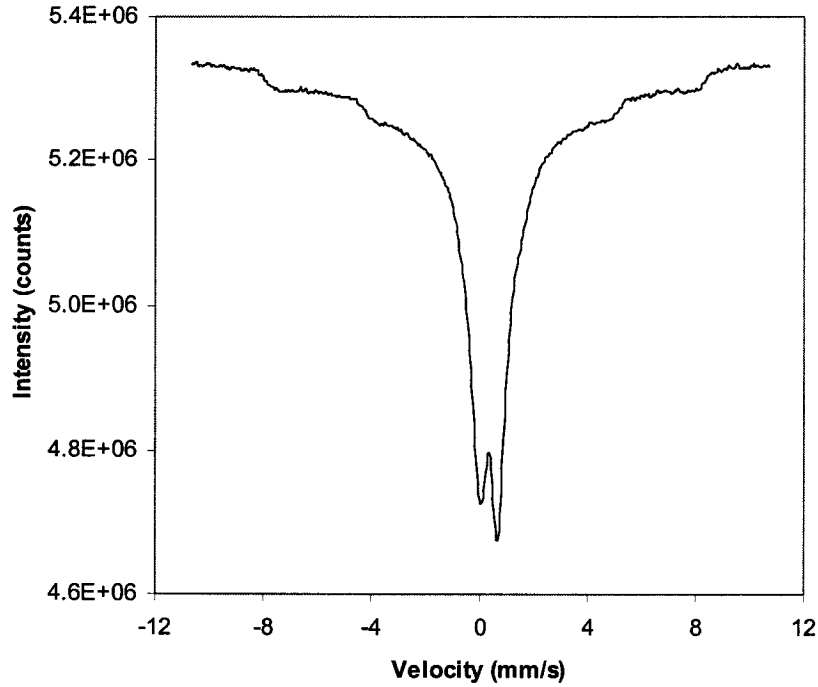

Figure 4.10 RT Mössbauer spectrum of NH-1

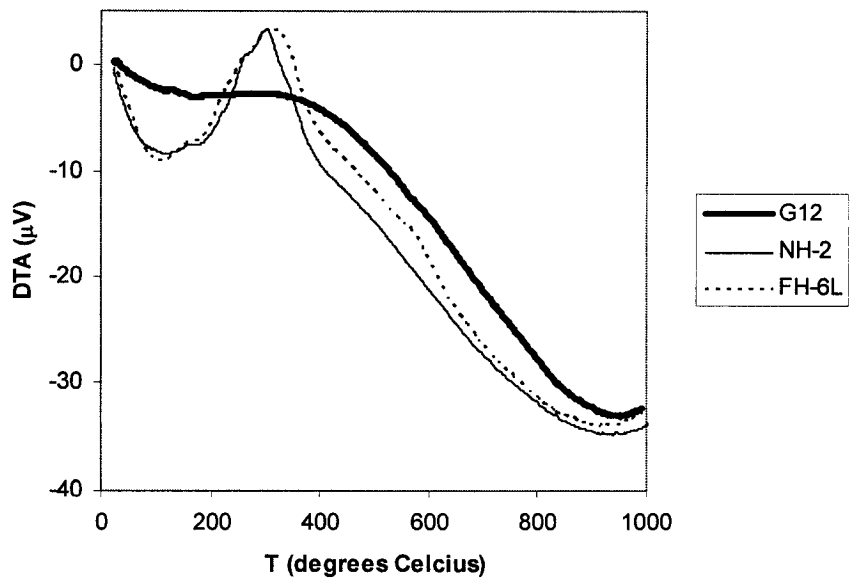

Figure 4.11 DTA curves of microcrystalline hematite G12, "nanohematite" NH-2 and the 6-line ferrihydrite (FH-6L)

Chapter 5 - Magnetic Measurement Methods

5.1 VSM operation

5.1.1 Measurement Principle

The vibrating sample magnetometer (VSM) is a very commonly used instrument for measuring magnetic hysteresis properties. The principle of operation is based on the induction method. The sample is made to vibrate at a fixed frequency in a perpendicular direction with respect to the applied magnetic field, which is produced by an electromagnet and measured by a Hall-effect probe (figure 5.1). The oscillation of the sample's magnetic dipoles changes the magnetic flux, thus inducing an a.c. voltage in the detection coils (Crangle 1991, p.59; Foner 1959). The non-symmetrically distributed effective area-turns of the coils permit the detection of this voltage. The device converts the magnitude of this voltage into a magnetic moment value and plots it as a function of the applied field measured by the Hall-effect probe.

5.1.2 VSM Specifications

The VSM used is the model 7304 manufactured by Lake Shore Cryotronics, Inc. The Lake Shore VSM software IDEAS-VSM Version 3.0 controls the experiments. The error in the moment measurement claimed by the manufacturer is 5×10^{-6} emu. This quantity is in agreement with the statistical error in the magnetic moment calculated using time experiments (see appendix A, section A.1)

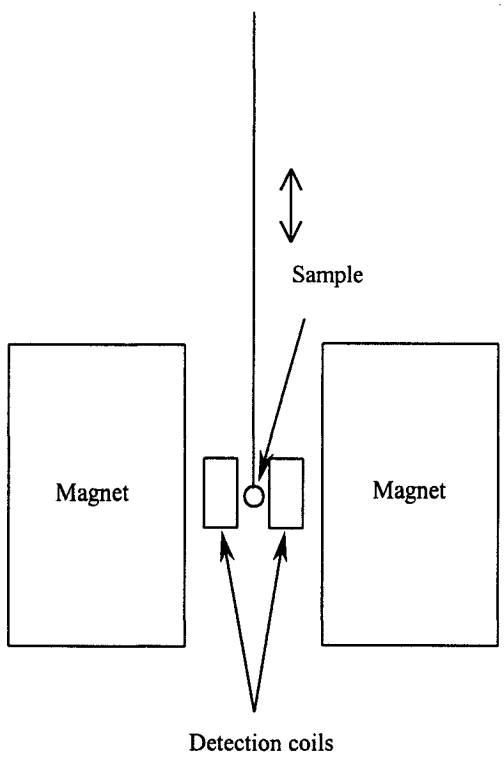

Figure 5.1 Schematic representation of the main VSM features. Modified from Crangle (1991)

The manufacturer claims a field error of 0.05 G and a reproducibility better than 1% of the measured moment or 0.15% of the full scale, whichever is greater. The measured reproducibility (see appendix A, section A.2) ranges from 0.9 to 1.9% of the measured moment value.

5.1.3 Experimental Settings

The hysteresis curves or field curves at room temperature (RT) (22 °C) are obtained through a field cycle in which the magnetic moment is measured as the applied magnetic field strength is varied between –10 and 10 kG ([-10,000; 10,000] G). These field cycles include an initial magnetization curve from 0 to 10 kG and a complete field cycle curve that

goes from 10 to −10 kG and back to 10 kG. Table 5.1 indicates the settings and conditions used for these measurements.

Name of experiment	hyst RT
Experiment type	Field experiment: initial curve + hysteresis (0 to H_{max} to $-H_{max}$ to H_{max})
H_{max}	10 kG
Acquisition mode	Point by point
Field increment	0.847 kG
Average time per point	10 s
Number per points	60
Time constant	300 ms
Auto Range	On

Table 5.1 Experimental settings for the hysteresis measurements

5.1.4 Experimental Procedure

The VSM is operated following the guidelines recommended by the manufacturer and some additional suggestions (see appendix B). After performing the necessary calibrations and procedures necessary before each hysteresis measurement session, hysteresis measurements at room temperature (22 °C) were performed in all empty sample holders and samples with the settings and conditions described in the previous section (section 5.1.3)

The samples were weighted in a microbalance following the procedure outlined in appendix C. The first set of ten samples was weighed three times each one using this procedure. Within this procedure, the errors in the weight values for the holders and samples (including holder) were taken as the standard deviation of the mean, following the statistical analysis of random errors (Preston and Dietz, 1991). The net sample weight has an associated error calculated through propagation of errors (see following section 5.4). The mean value of

these errors, 0.004 mg, was taken as the error in the net weight value of the rest of the samples.

Two hysteresis measurements ("hyst RT" experiments) were performed on each sample, using the option of "profiles" provided by the software, which permits several experiments to be run one after the other. All the experiment details were recorded in a VSM run sheet (see appendix A and D), and all the data was saved in the magnetometry backup system in the laboratory. The measured data is in the cgs (emu) unit system, and all the quantities derived from it are kept in this unit system; appendix E indicates the units used for each magnetic quantity and their conversion to the SI unit system.

5.2 Pre-treatment of Data

The two sets of data in a profile were averaged and thus one set of data (moment, field) was assigned for each holder (*holder signal*) and each sample ((*sample + holder*) *signal*). For the case of samples that show hysteresis (i.e., remanence and coercivity), only the first hysteresis cycle run was considered since the second run signal is affected by the remanent magnetization from the first run.

The empty holder signal was different in shape and magnitude for each holder, perhaps due to impurities included in the material during the manufacturing process. Thus, it is necessary to correct the sample signal for this effect. The sample signal is then given by:

$$sample\ signal = (sample + holder)\ signal - holder\ signal \qquad (5\text{-}1).$$

The following figures illustrate the pre-treatment of data for sample M60-600: figure 5.2 shows the raw measured data for the sample; figure 5.3 shows the two runs considered

for the holder used in this case and their average, which is taken as the holder signal; and figure 5.4 shows the holder-corrected signal for M60-600.

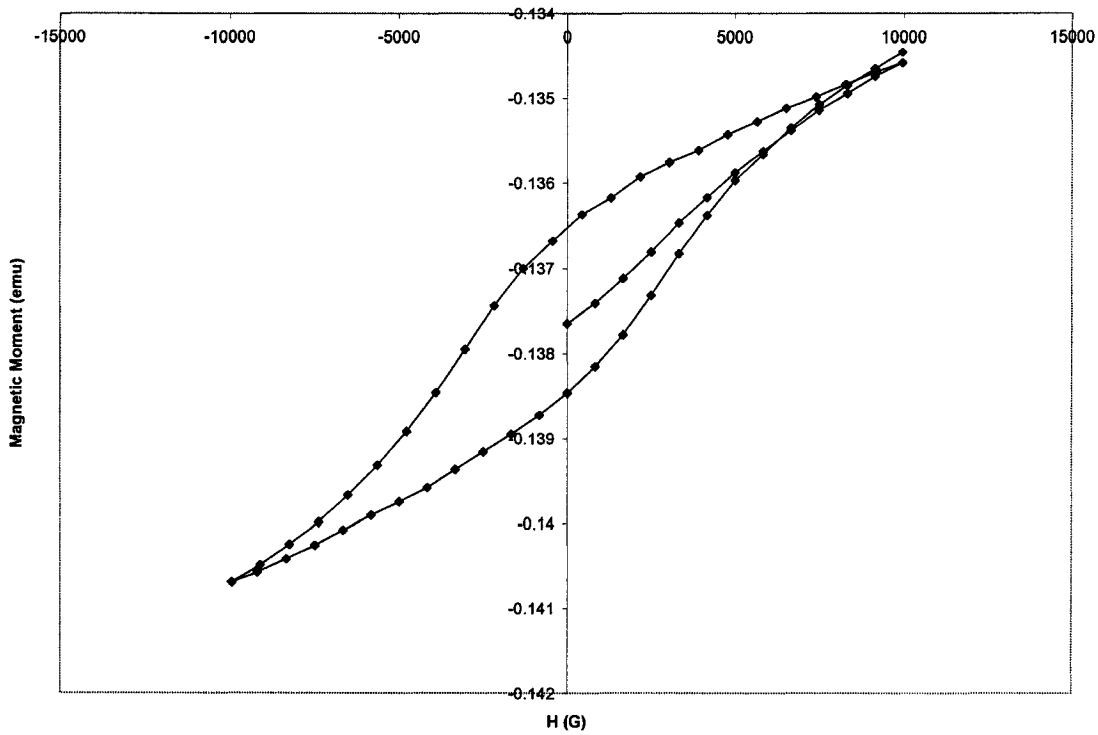

Figure 5.2 Raw data of M60-600 before holder correction

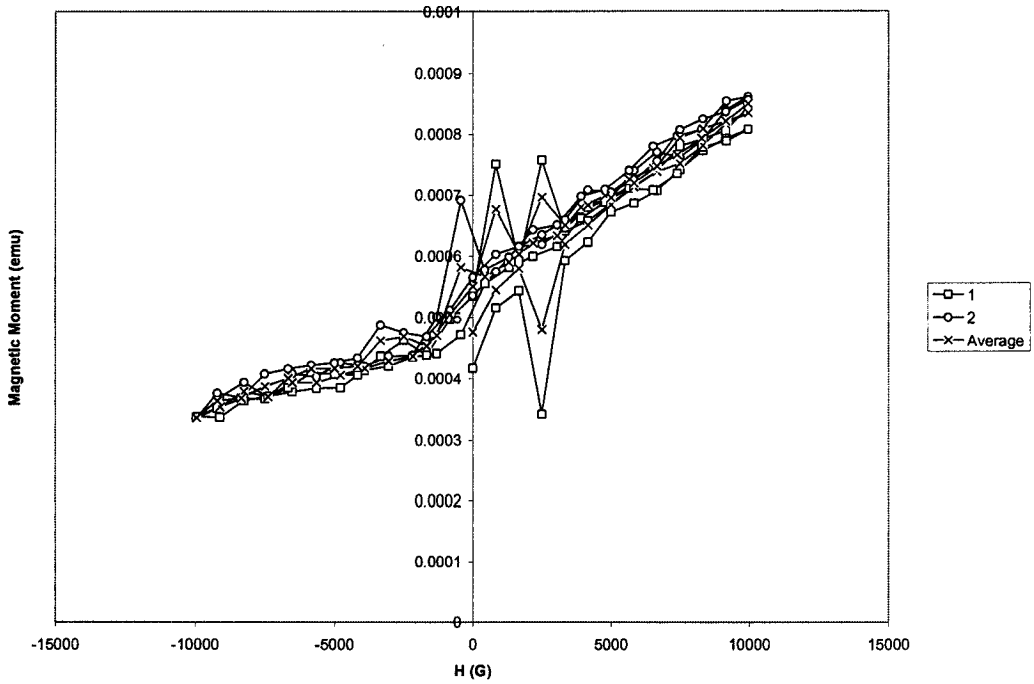

Figure 5.3 Field cycle runs of holder used for M60-600

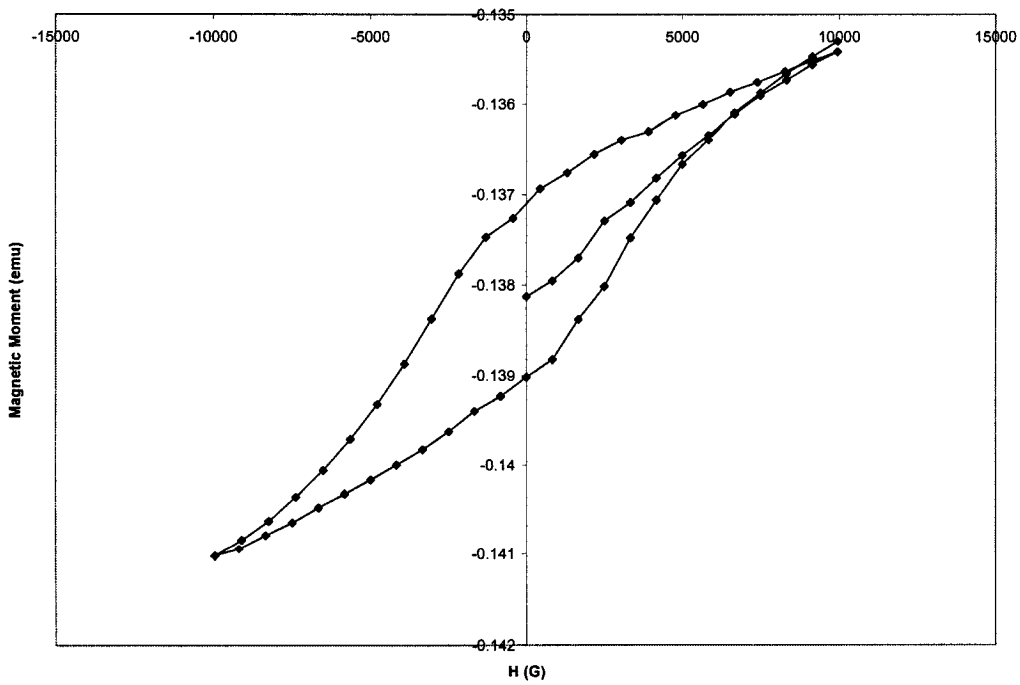

Figure 5.4 Holder-corrected field cycle for M60-600

5.3 Data Corrections

The pre-treated data needs to be corrected for several factors in order to obtain correct and comparable magnetization curves for the samples. Figures 5.5 to 5.7 illustrate the effect of the correction procedure performed on sample M60-600. The necessary corrections are:

- Centre shift

Generally, the measured data is not visually centred at zero. That is, it presents a shift from the zero moment value (e.g., figure 5.2). This is an artifact of the Lake Shore VSM system (see appendix A, section A.3). To make visual comparison among samples easier, all of the sample signals were centred at zero by adding or subtracting a "centre shift" value to the data (see figure 5.5). This value is calculated finding the intercepts of the hysteresis curve in the positive and negative axis and taking half of their absolute difference. Then, this value is subtracted or added, depending whether the original initial moment value (at zero field) is in the positive or negative axis, respectively.

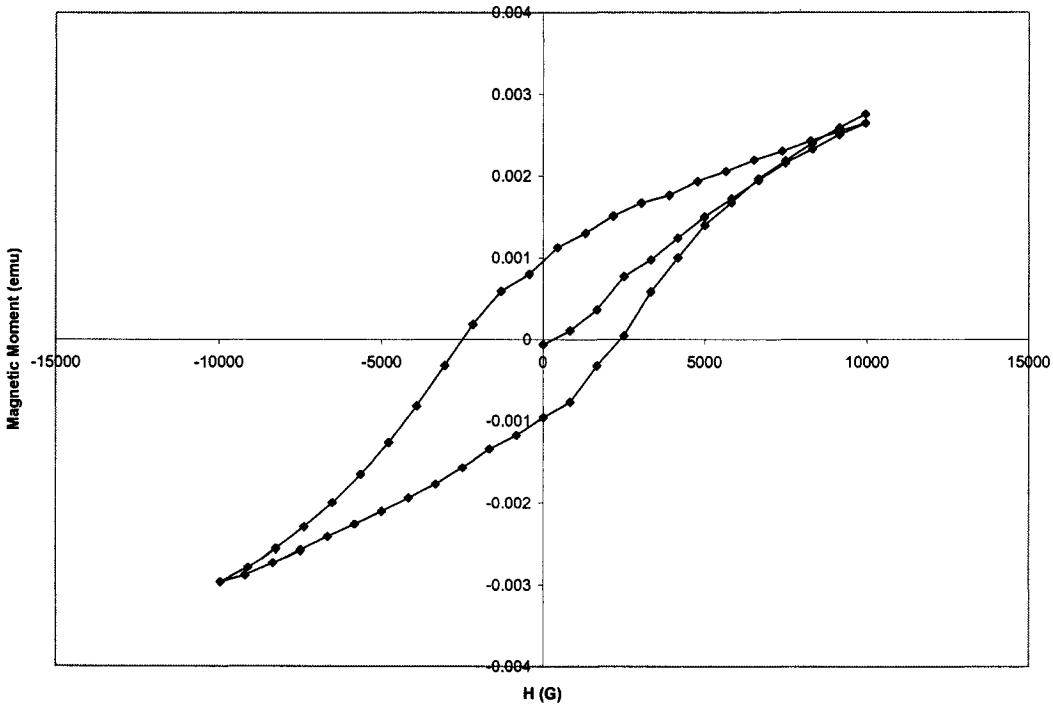

Figure 5.5 Centred field cycle of M60-600

- Addition of Diamagnetic Material

Some samples (M60-400 and M60-600) were available only in small quantities and did not fill completely the holder therefore the sample could not be immobilized. The addition of a non-magnetic material became necessary to completely fill the volume of the holder and assure the immobilization of the sample. The non-magnetic material added was powdered sugar; this material does not alter the magnetic properties of the sample and it can be removed afterwards by rinsing the sample.

A hysteresis measurement of the pure powdered sugar performed with the same settings and conditions as with the samples gives a diamagnetic mass susceptibility value (χ_s)

of -1.120(5) × 10^{-6} emu/gG characteristic of the sugar used. This value is used to correct for the magnetic contribution of the sugar in the two samples mentioned above. The magnetic moment value associated with the sugar is $\chi_s m_s H$, where m_s is the amount of sugar added for each sample, and H is the applied field strength. Therefore, the corrected signal is: (see figure 5.6)

$$sample\ signal - \chi_s m_s H. \qquad (5\text{-}2).$$

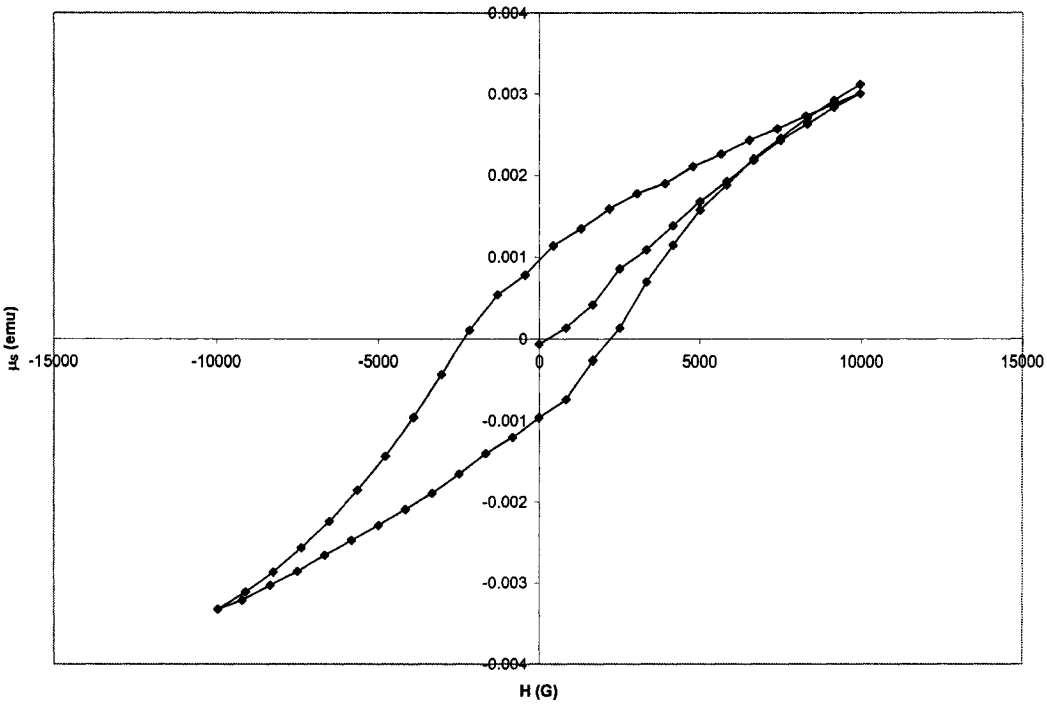

Figure 5.6 Field cycle of M60-600 corrected for addition of diamagnetic material

- Sample Mass

The corrected sample signal (μ_s) is normalized by the sample mass (m) to enable comparison among samples. This correction provides the mass magnetization value (M_g) in emu/g: (see figure 5.7)

$$M_g = \frac{\mu_s}{m} \tag{5-3}$$

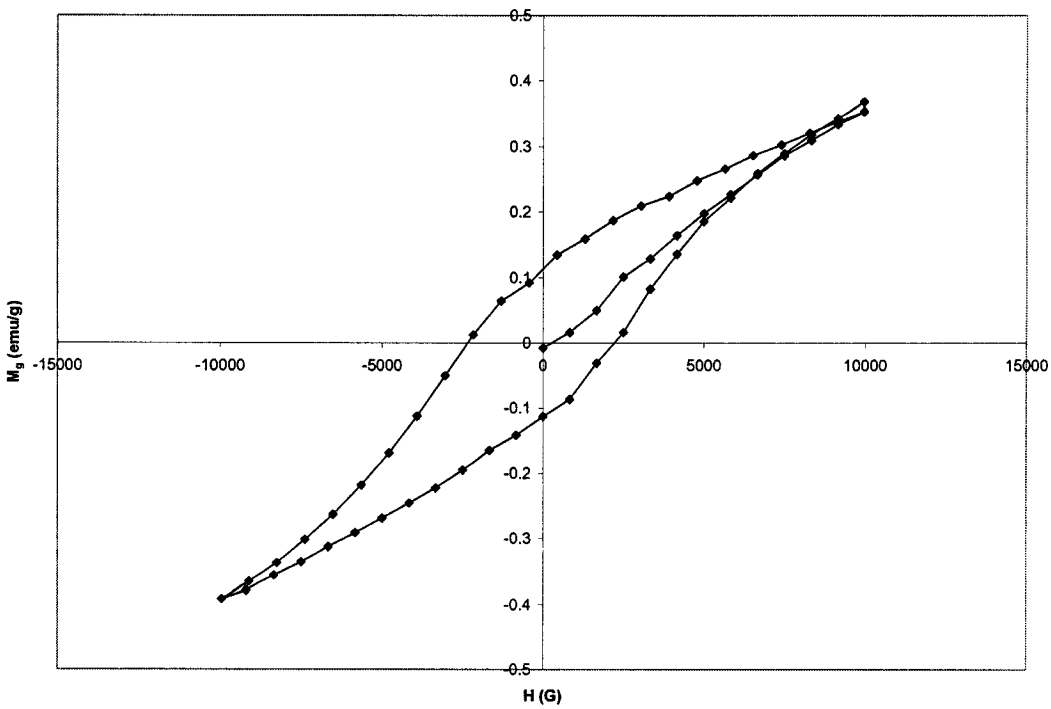

Figure 5.7 Final mass magnetization field cycle of M60-600

- Core diamagnetism correction

This correction considers the diamagnetism associated with the closed shells of the ferric and oxygen atoms in hematites and ferrihydrites. The theoretical diamagnetic mass

susceptibilities for hematite assuming a stoichiometry of Fe_2O_3 and of ferrihydrite assuming any of the three most accepted formulas ($Fe_5HO_8 \cdot 4H_2O$; $5Fe_2O_3 \cdot 9H_2O$; $Fe_2O_3 \cdot 2FeOOH \cdot 2.6H_2O$) are -3.51×10^{-7} and -4.04×10^{-7} emu/gG, respectively. These values correspond to a typical range of 0.2 to 1.7% of the measured mass susceptibilities. This range is comparable to the precision error range in the measured moment (0.1 to 2.0%) and therefore the data was not corrected for this effect.

5.4 Estimation of Errors

The final mass magnetization value (M_g) and all the calculated quantities in this thesis have an associated precision error that is the product of the propagation of the errors of all the quantities involved in the calculations and necessary corrections. This propagation follows the basic formula for error propagation (Preston and Dietz, 1991):

$$\delta w = \sqrt{\left(\frac{\partial w}{\partial x}\delta x\right)^2 + \left(\frac{\partial w}{\partial y}\delta y\right)^2 + \left(\frac{\partial w}{\partial z}\delta z\right)^2} \qquad (5\text{-}4).$$

In this formula w is the quantity being calculated using the quantities: x, y and z; their associated errors are δx, δy and δz, respectively, and δw is the propagated precision error for the derived quantity, w.

When a best-fit line is used to calculate a quantity, the precision errors of the y-axis quantity are used as statistical weights in the calculation of the best-fit line and the errors in the associated intercept and slope.

Chapter 6 – Presentation of Measured Data

This chapter shows the measured data of hysteresis cycles or mass magnetization-field cycles for all the samples considered in this study. These curves are corrected for all the aspects indicated in sections 5.2 and 5.3 in order to obtain comparable and the most accurate data possible that can be used for the analysis and study of the samples considered. For all the samples the precision errors in the mass magnetization values shown, calculated as described in section 5.4, are smaller than the size of the data markers. Figures 6.1 to 6.15 show the samples referred to as microcrystalline hematites in chapter 4. Figures 6.16 to 6.20 show the samples called ferrihydrites; and figures 6.21 to 6.24 present the data for the samples referred to as nanohematites, all previously described in chapter 4 (Sample Synthesis and Characterization).

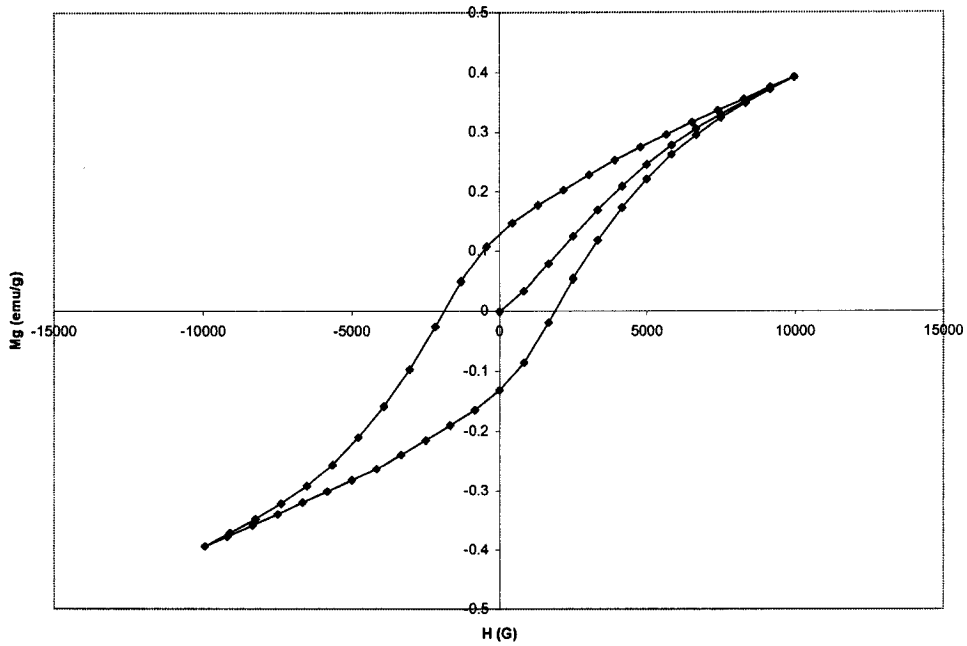

Figure 6.1 Field cycle of sample L1 (Initial solution: $FeSO_4$; Synthesis T: 160 °C)

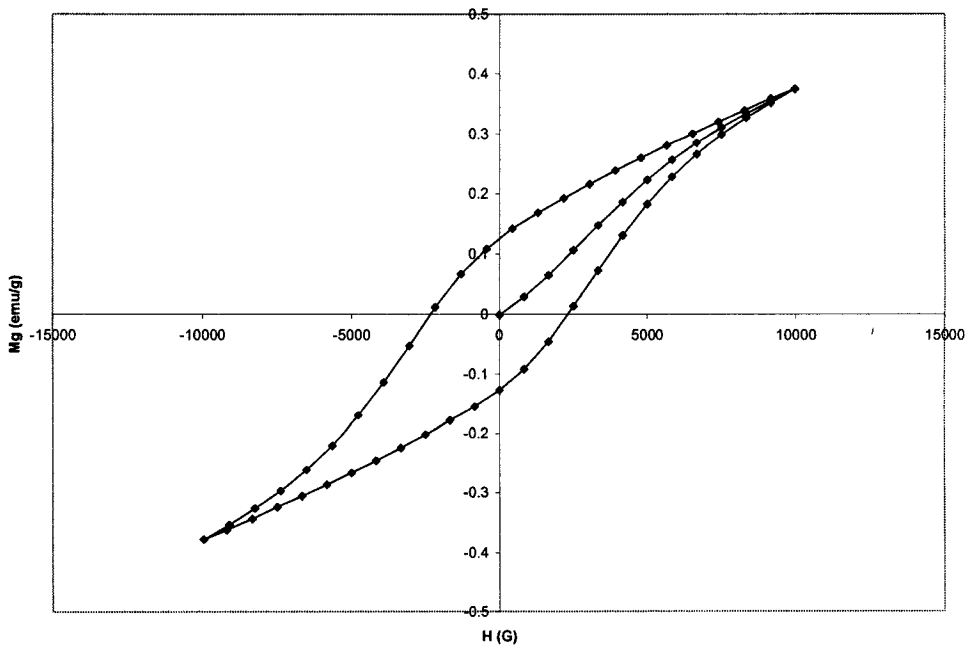

Figure 6.2 Field cycle of sample L3 ($FeSO_4$; 180 °C)

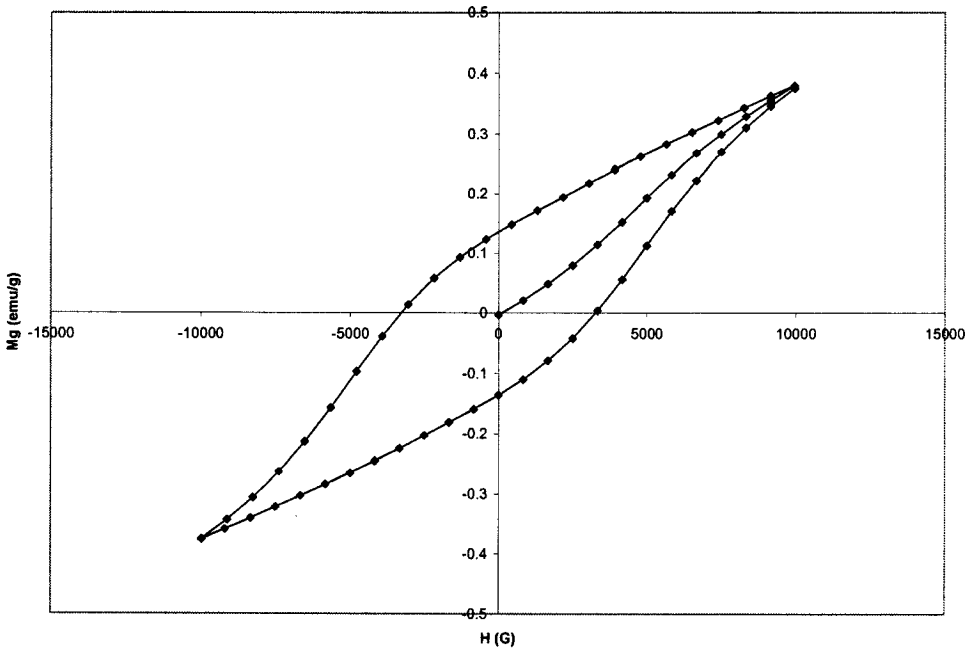

Figure 6.3 Field cycle of sample L7 ($FeSO_4$; 220 °C)

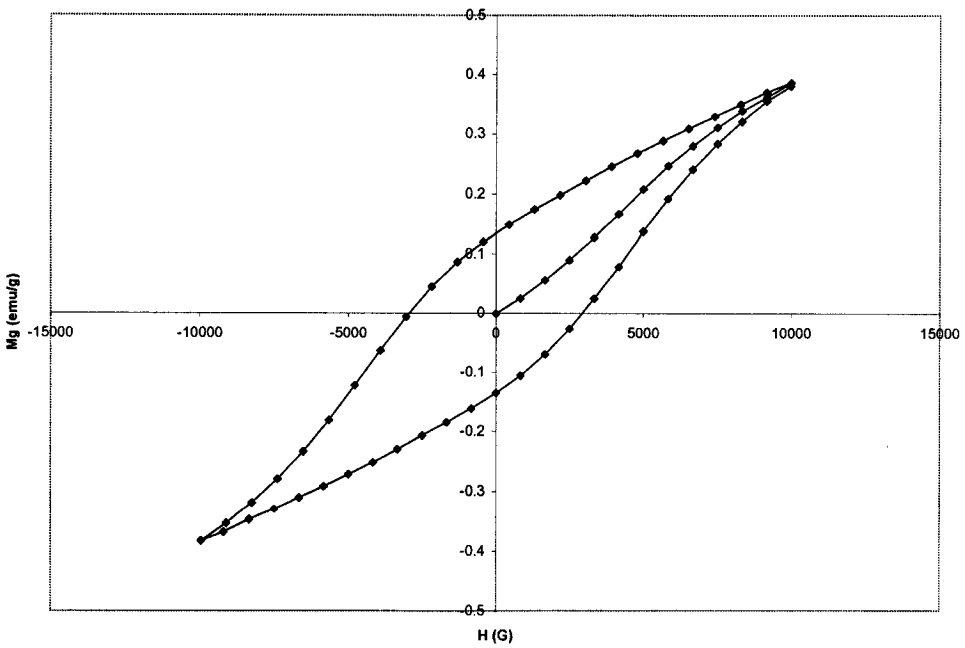

Figure 6.4 Field cycle of sample L9 ($FeSO_4$; 240 °C)

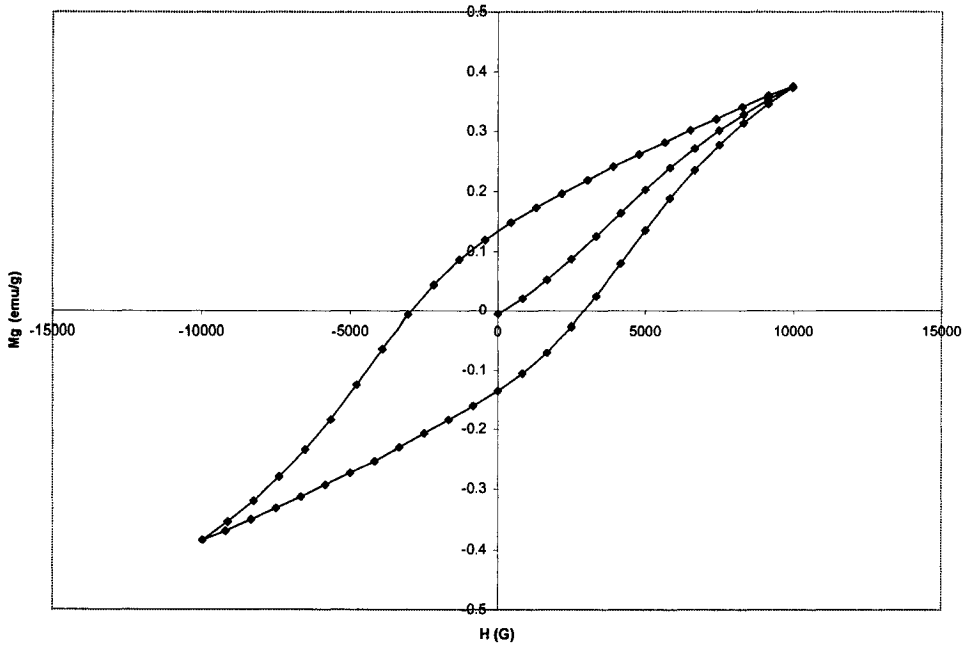

Figure 6.5 Field cycle of sample L10 ($FeSO_4$; 250 °C)

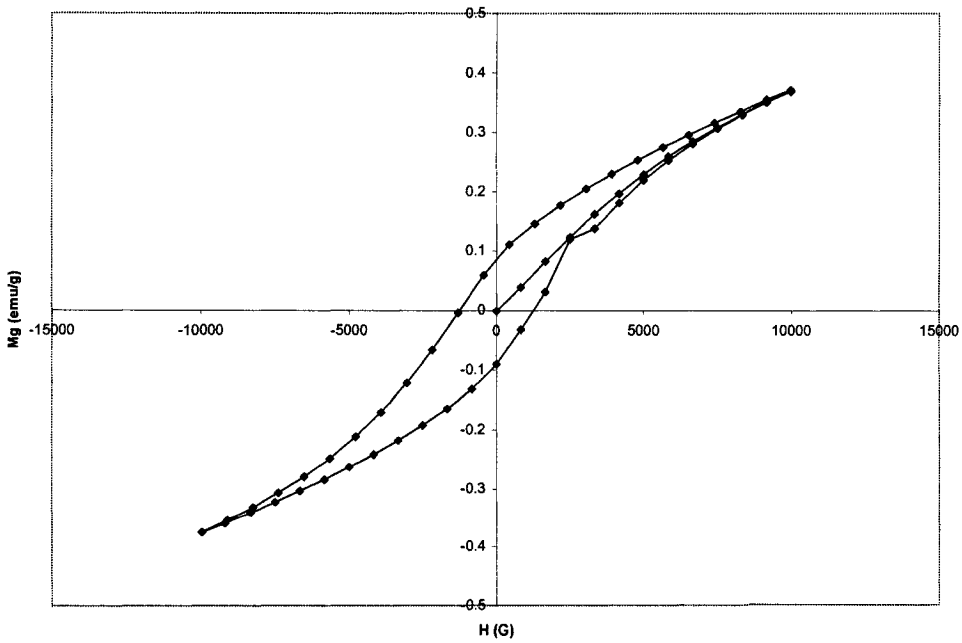

Figure 6.6 Field cycle of sample H1 ($Fe(NO_3)_3$; 150 °C)

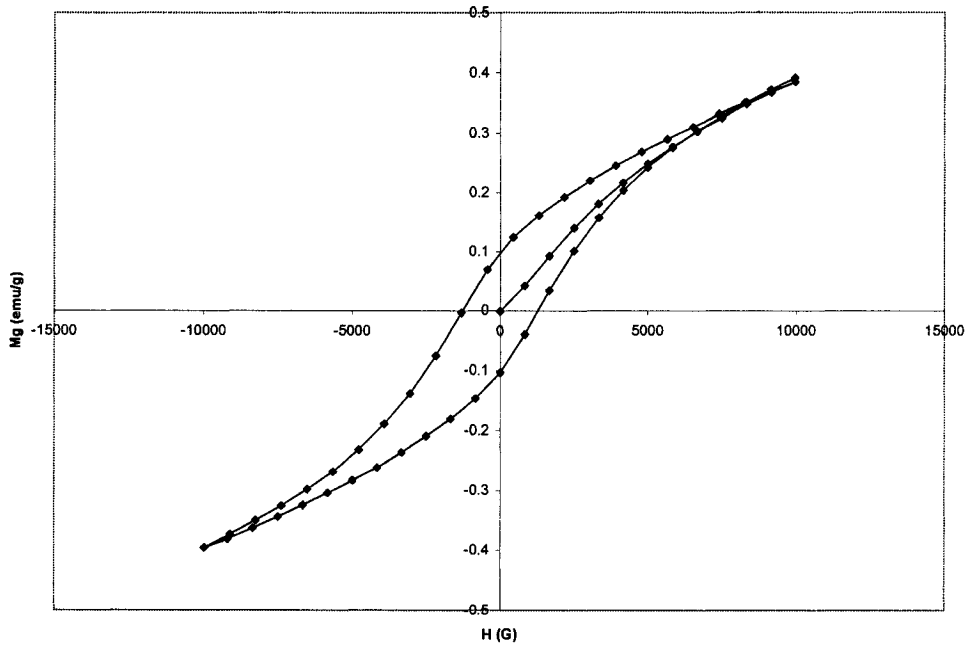

Figure 6.7 Field cycle of sample H2 ($Fe(NO_3)_3$; 200 °C)

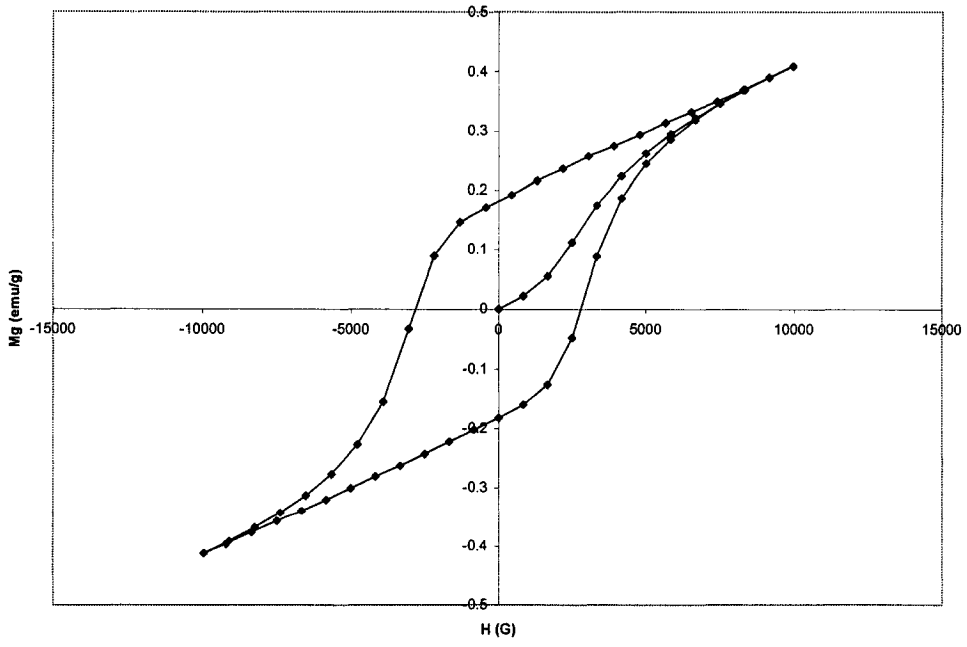

Figure 6.8 Field cycle of sample H3 ($FeCl_3$; 150 °C)

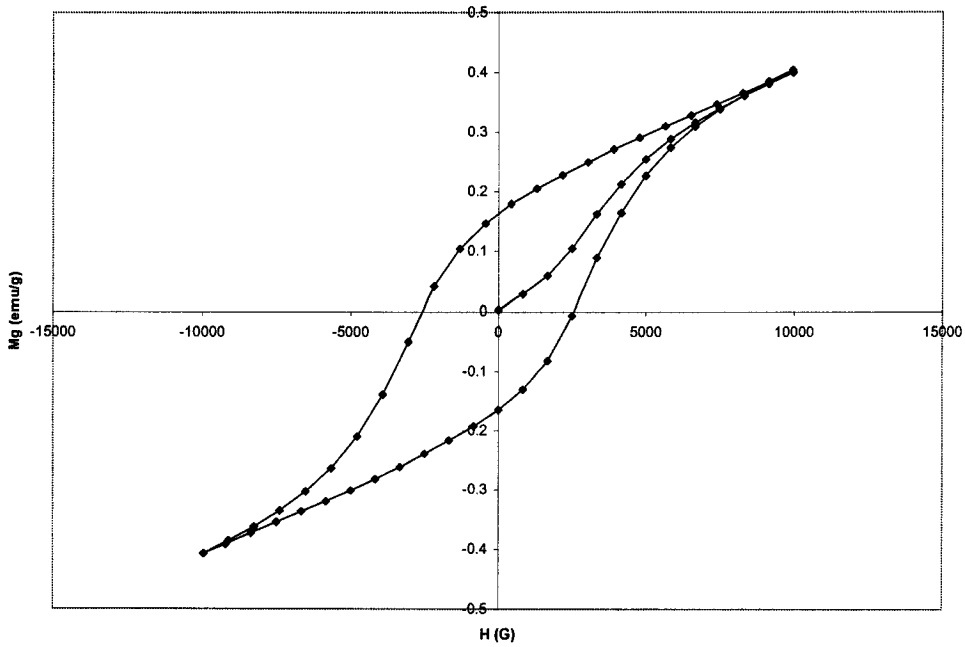

Figure 6.9 Field cycle of sample H4 ($FeCl_3$; 130 °C)

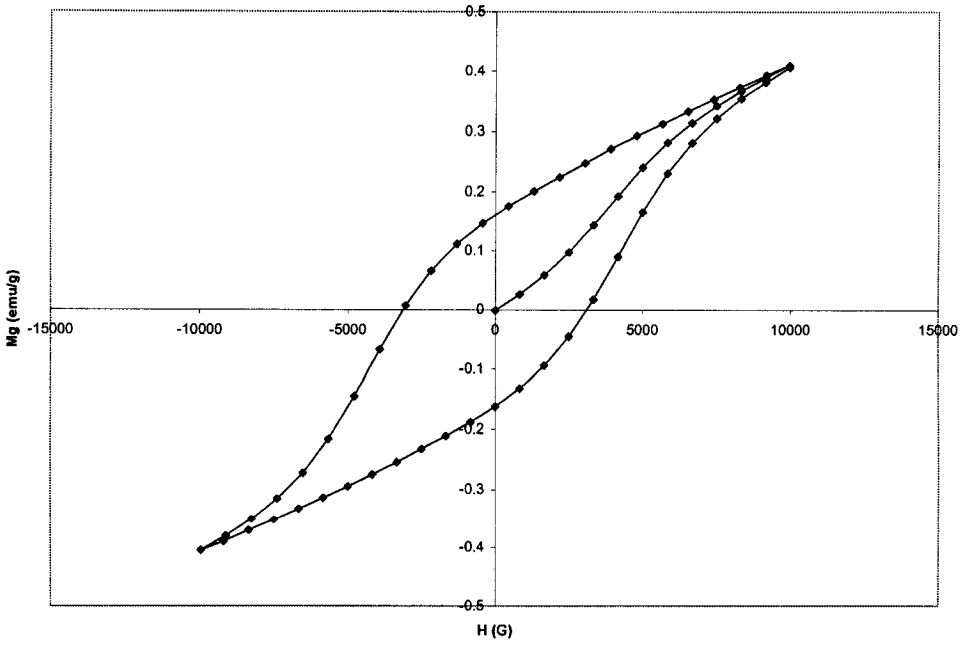

Figure 6.10 Field cycle of sample H5 ($Fe(SO_4)_{1.5}$; 210 °C)

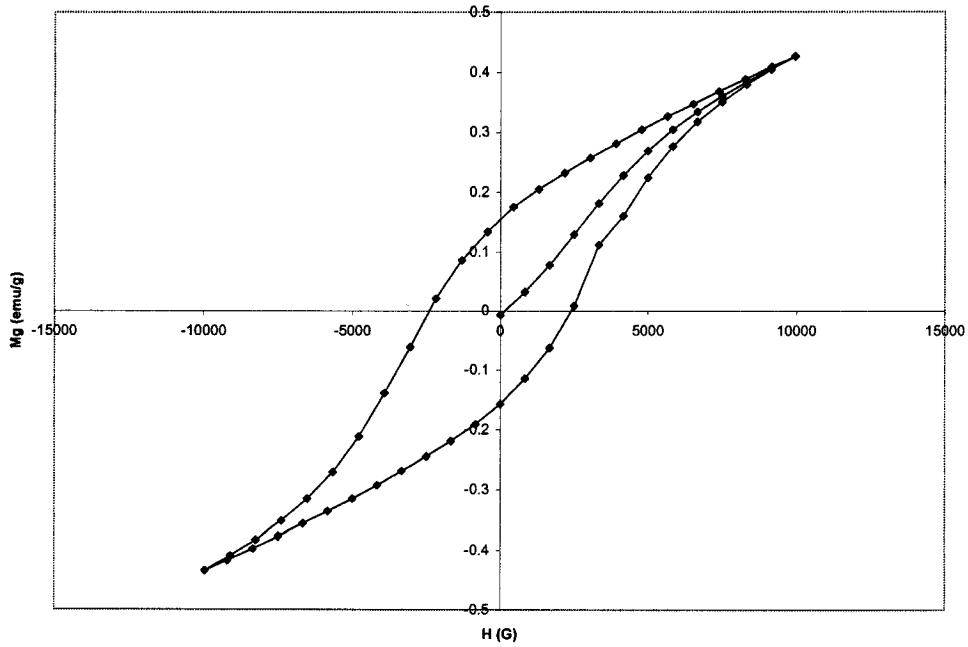

Figure 6.11 Field cycle of sample M60 ($Fe(SO_4)_{1.5}$; 220 °C)

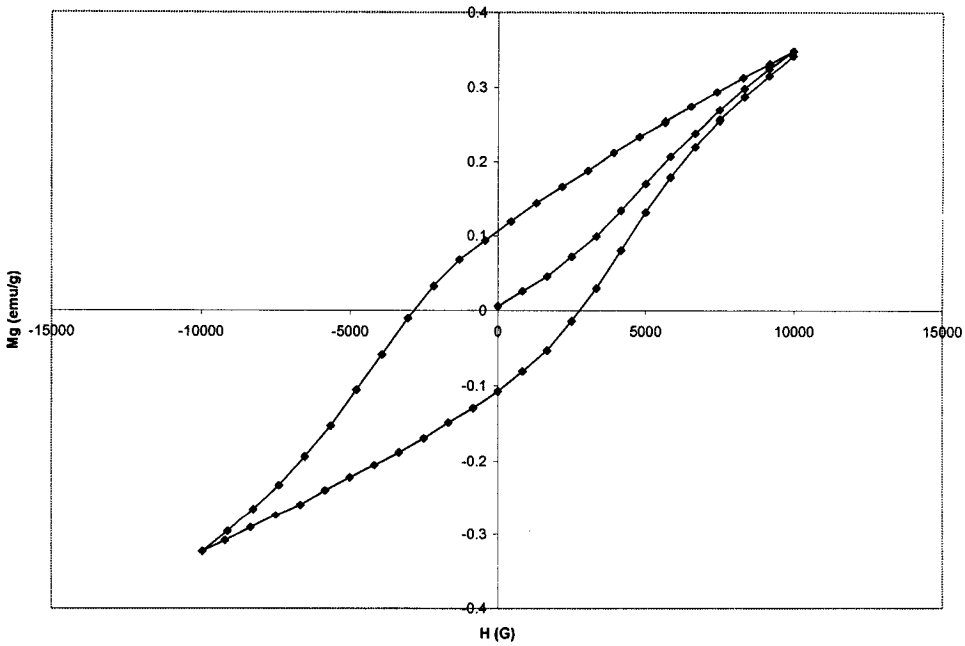

Figure 6.12 Field cycle of sample M60-400 ($Fe(SO_4)_{1.5}$; 220 °C)

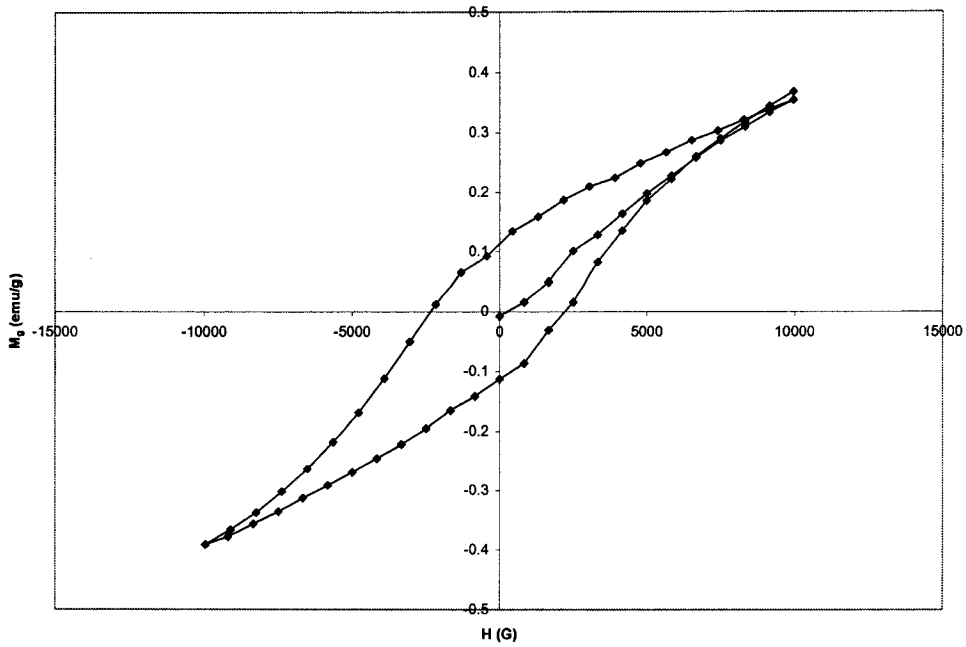

Figure 6.13 Field cycle of sample M60-600 ($Fe(SO_4)_{1.5}$; 220 °C)

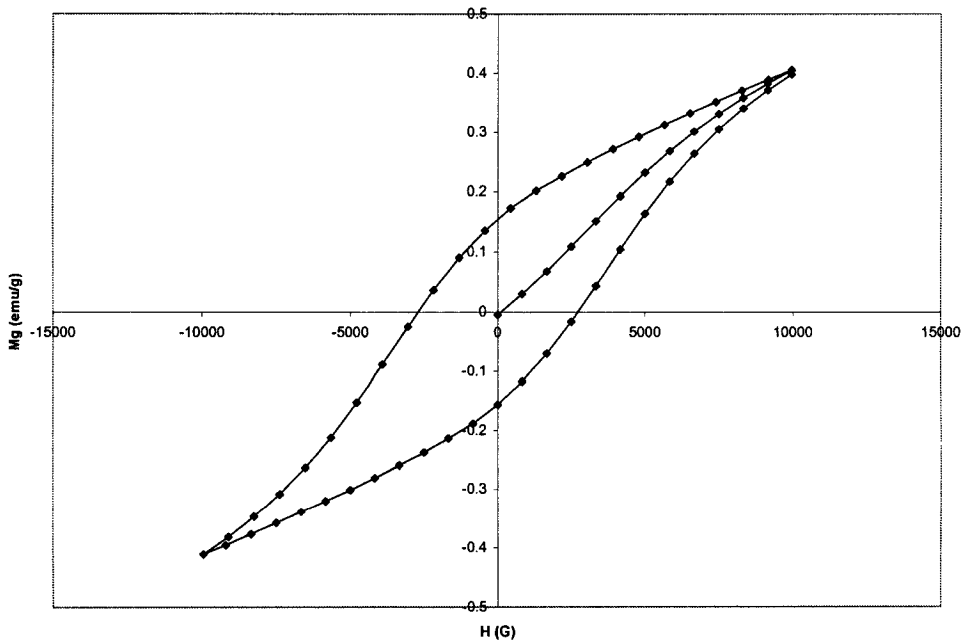

Figure 6.14 Field cycle of sample PBH

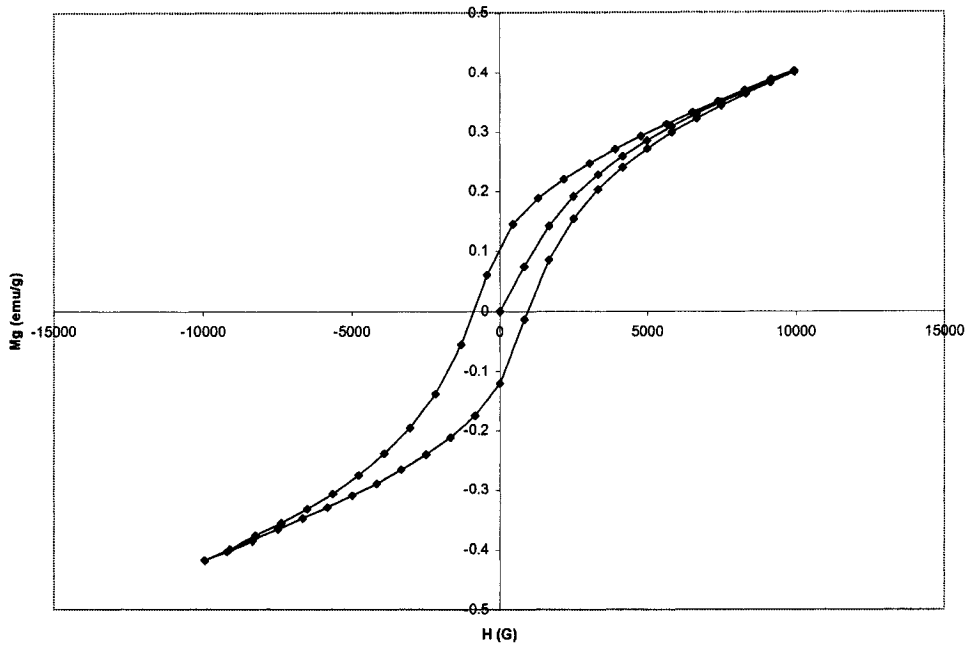

Figure 6.15 Field cycle of sample G12 ($Fe(SO_4)_{1.5}$ and H_2SO_4 ; 225 °C)

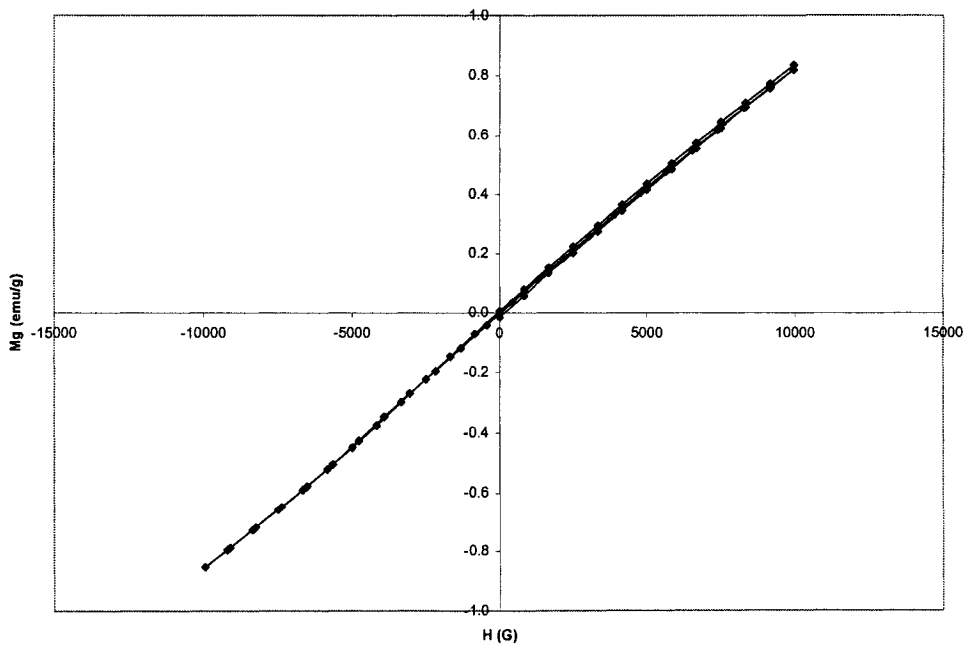

Figure 6.16 Field cycle of sample FH-6L ($Fe(NO_3)_3$)

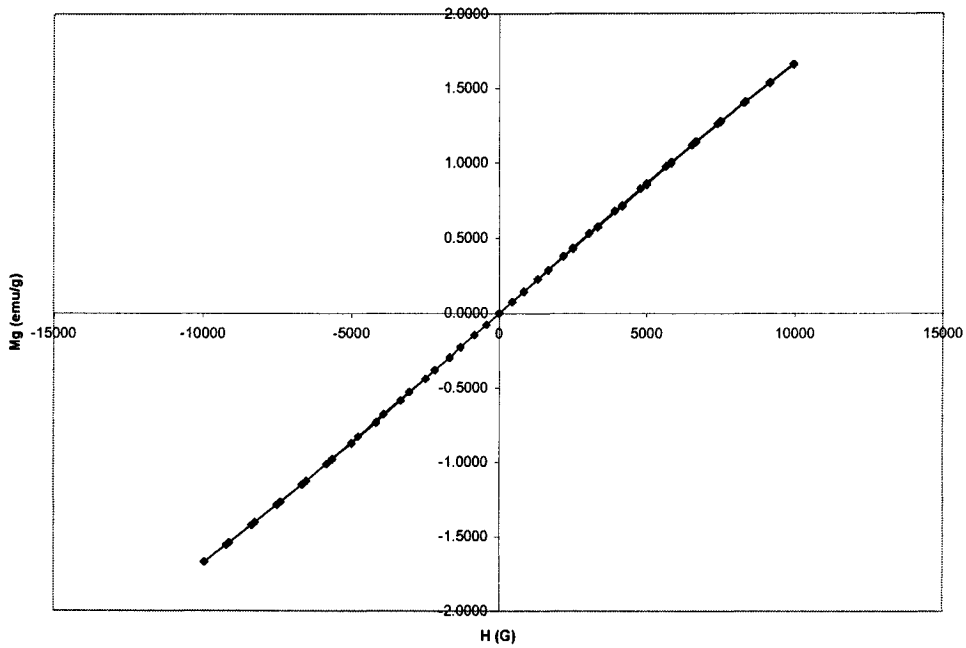

Figure 6.17 Field cycle of sample FH-2L-N1 ($Fe(NO_3)_3$)

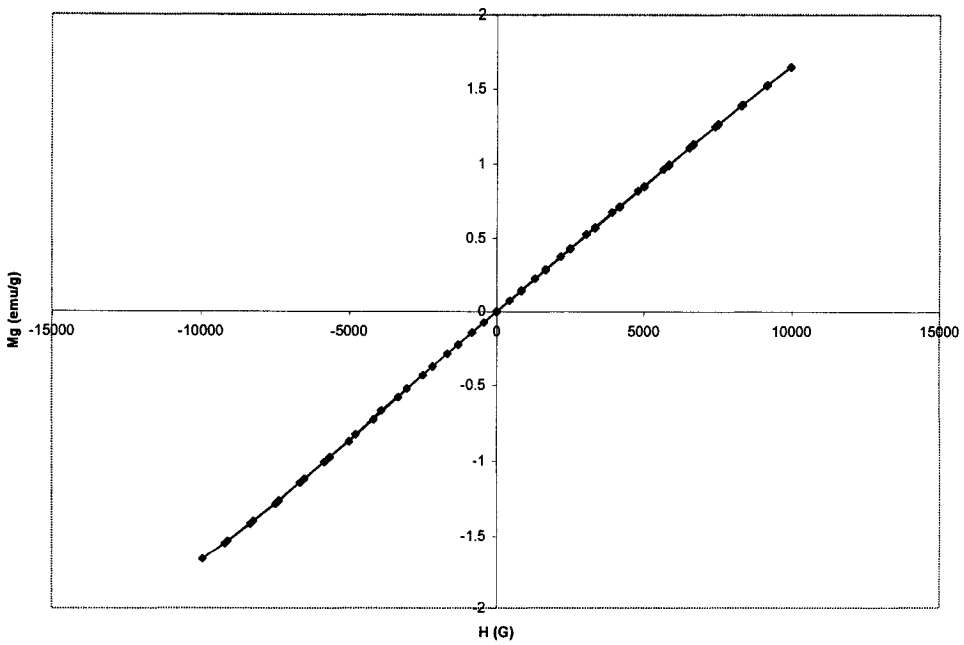

Figure 6.18 Field cycle of sample FH-2L-N2 ($Fe(NO_3)_3$)

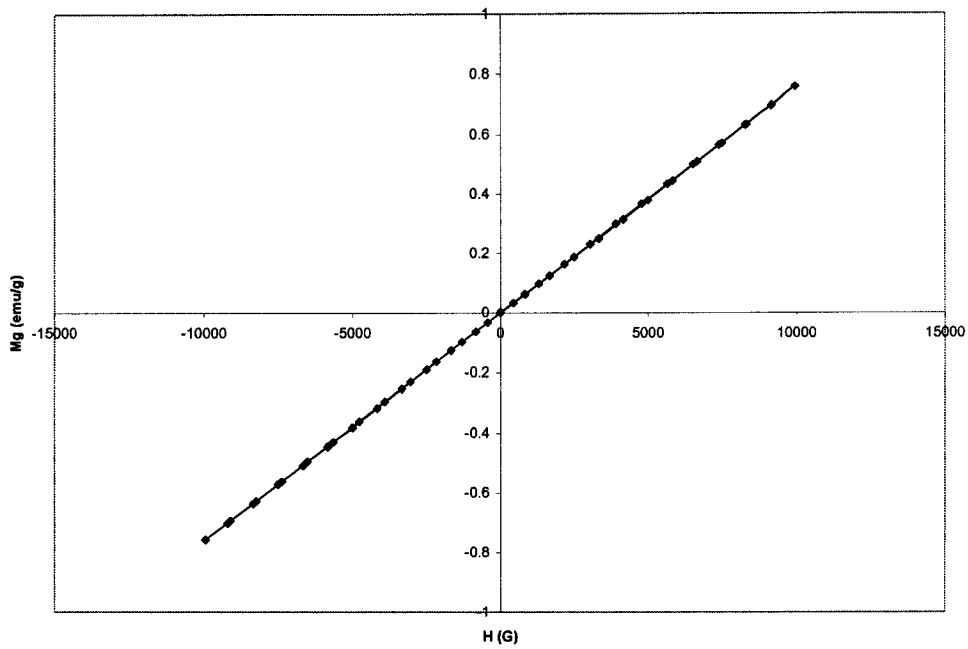

Figure 6.19 Field cycle of sample FH-2L-S ($Fe(SO_4)_{1.5}$)

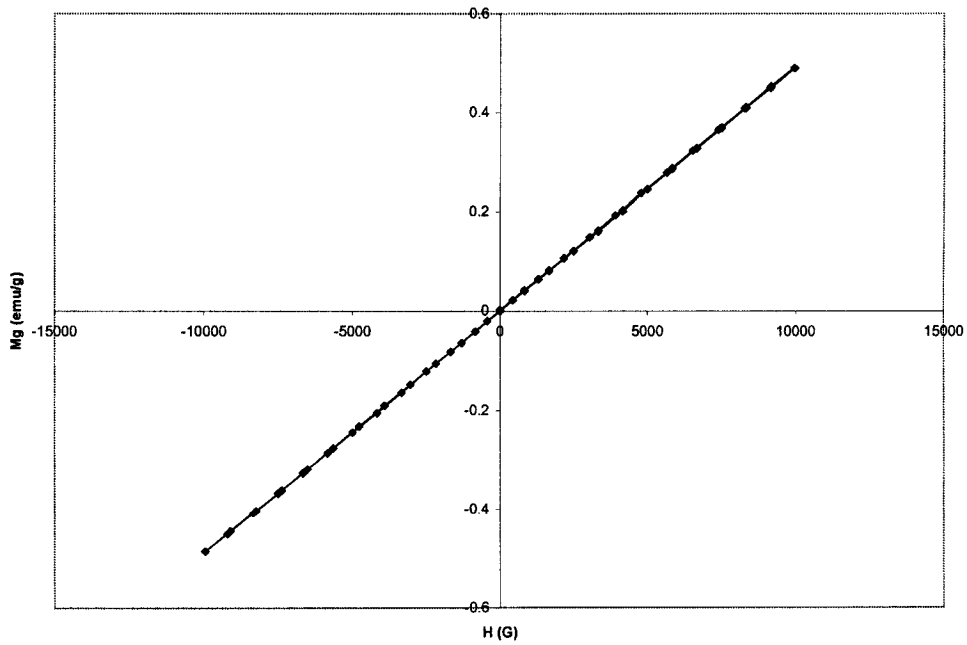

Figure 6.20 Field cycle of sample FH-2L-N3-P ($Fe(NO_3)_3$ and $NaH_2PO_4 \cdot H_2O$)

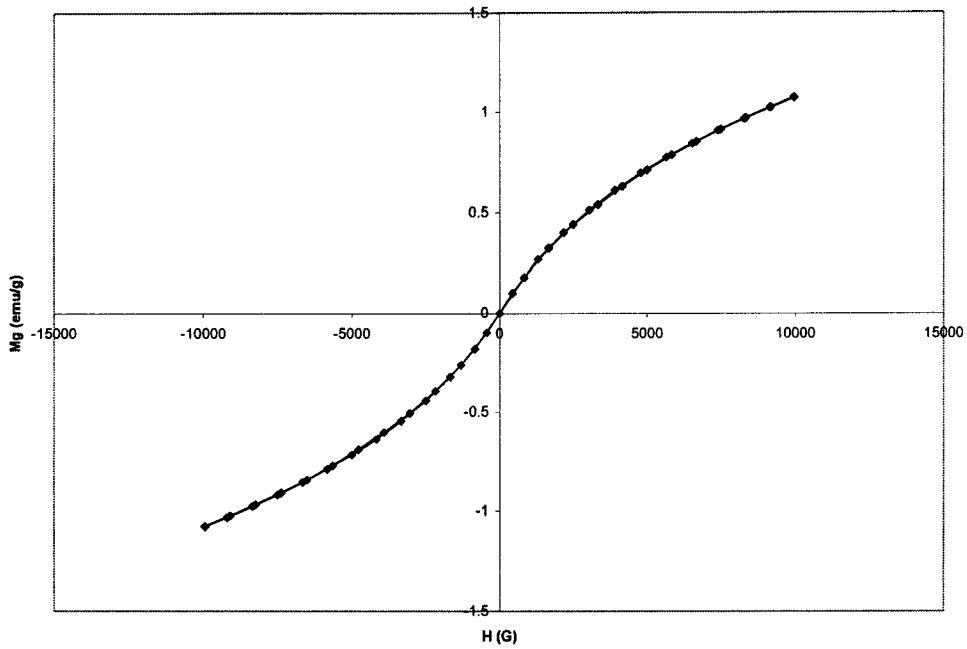

Figure 6.21 Field cycle of sample NH-1 ($Fe(NO_3)_3$)

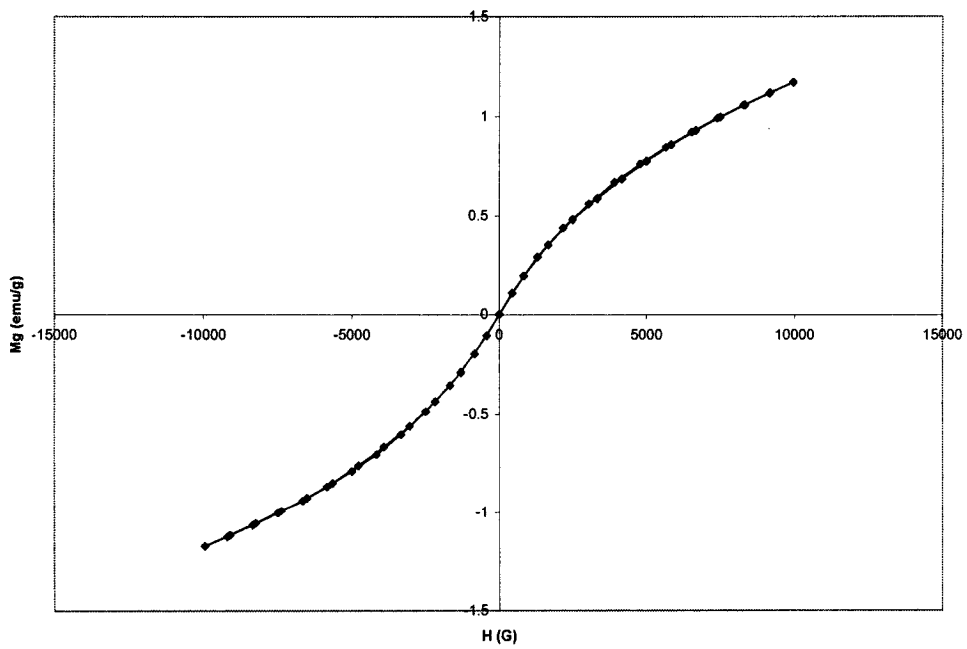

Figure 6.22 Field cycle of sample NH-2 ($Fe(NO_3)_3$)

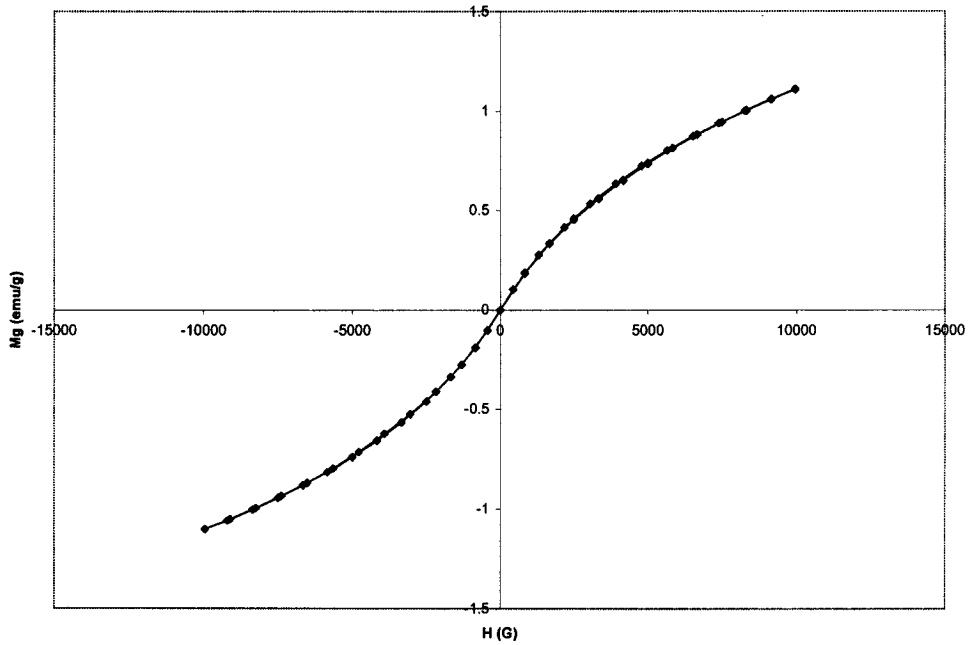

Figure 6.23 Field cycle of sample NH-3 ($Fe(NO_3)_3$)

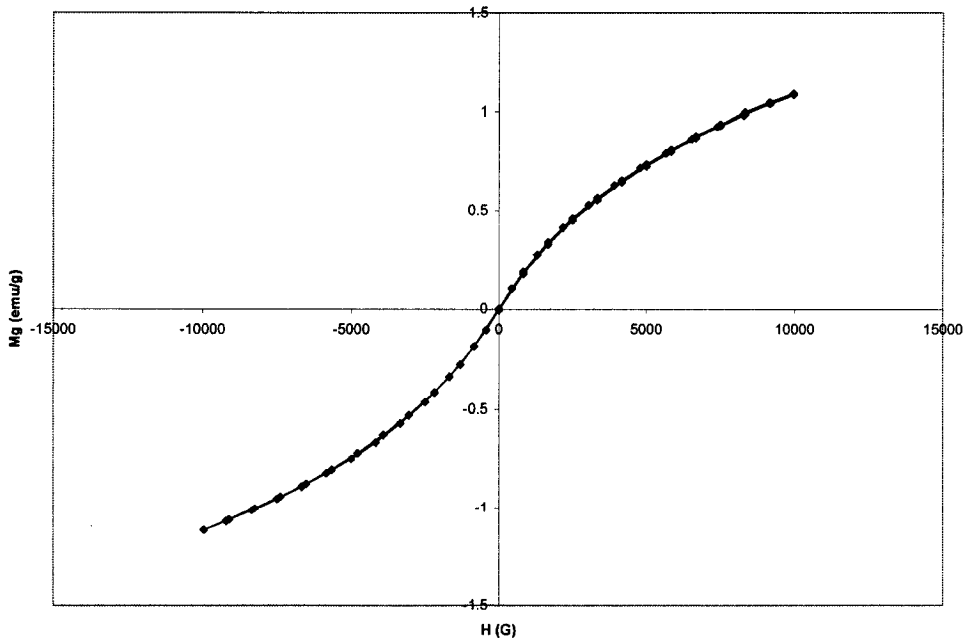

Figure 6.24 Field cycle of sample NH-4 ($Fe(NO_3)_3$)

Chapter 7 – Data Analysis Methods

After performing all the necessary data corrections outlined in chapter 5, the magnetization curves presented in chapter 6 are now ready to be used for the study of the samples. This chapter explains the methods of analysis of the data presented in the magnetization curves.

7.1 Basic Extractable Parameters

As can be seen in the presentation of the data (chapter 6), there are two distinguishable types of magnetization-field cycles. The microcrystalline iron oxides (microcrystalline hematite samples) present wide field cycles (figures 6.1 to 6.15); they actually show the hysteresis effect, meaning that they present remanence and coercivity. In contrast, the nanophase iron oxides and oxyhydroxides (nanohematites and ferrihydrites) show narrow field cycles (figures 6.16 to 6.24) where the magnetization curves and demagnetization curves are the same, showing lack of remanence and coercivity. Figures 7.1 and 7.2 show schematic representations of typical wide and narrow field cycles, respectively, indicating the operational parameters that can be extracted directly from the field cycles, which could aid their description and analysis. In a few words these parameters are: the coercivity (H_c), the remanent magnetization (M_r), the spontaneous (i.e., extrapolated to zero field) magnetization (M_s), the maximum magnetization (M_{max}) measured at the highest field applied (± 10 kG), the initial slope (χ_0) and the demagnetization slope (χ_d) at high field region.

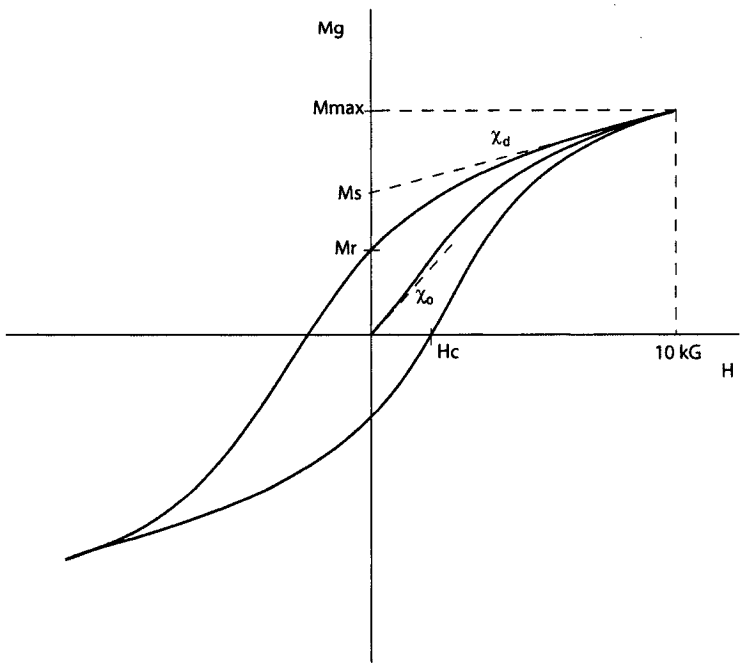

Figure 7.1 Representative hysteresis cycle of microcrystalline samples showing operational extractable parameters

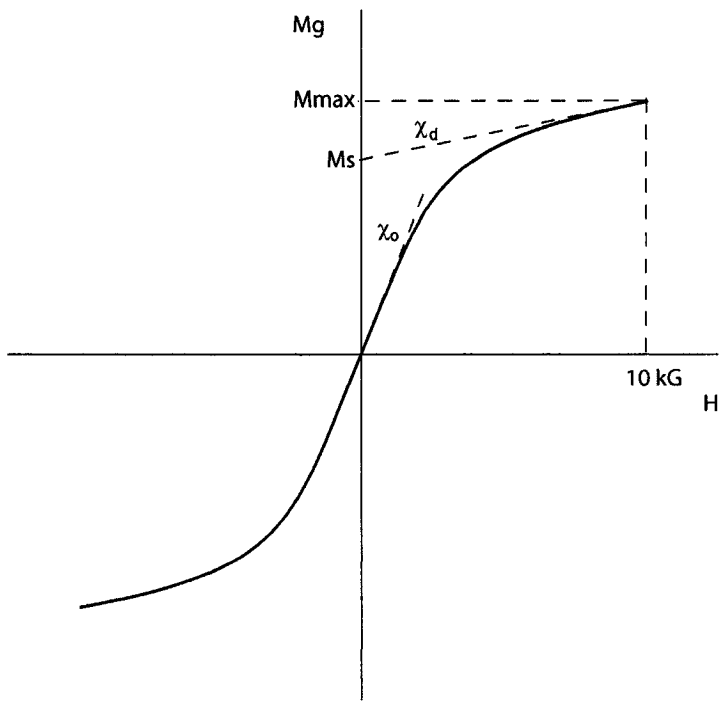

Figure 7.2 Representative field cycle of nanophase samples showing operational extractable parameters

The coercivity (H_c) is taken as the intersection point of the curve on the field axis. The remanent magnetization (M_r) is taken as the crossing point of the field curve on the magnetization axis. The maximum magnetization (M_{max}) is the value of magnetization at the highest absolute field attained (± 10 kG). The spontaneous magnetization (M_s) is the intercept on the magnetization axis of the best-fit line through the points on the high field region that often present a linear behaviour ($|H| \geq 6$ kG, for the microcrystalline hematite samples and the nanohematites samples; $|H| \geq 7$ kG, for ferrihydrites). It is important to point out that saturation might not have been reached at the highest field attained (± 10 kG) for all of the samples considered, thus, M_s and M_{max} may not be truly saturation magnetizations. The demagnetization slope (χ_d) is the slope of the best-fit line of the points in the high field linear region used for the extraction of M_s. All of the parameters described above were extracted from both the positive and negative axis, and the final value used is the average of the absolute values of these.

For the microcrystalline hematite samples, the initial slope (χ_o) is defined as the slope of the curve in the field range from 0 G to 500 G. This is the slope of the line formed by the first and second point of the initial magnetization curve. Ideally, the intrinsic initial susceptibility of a material is measured at very low fields (up to 1 G). This is usually hard to measure in a VSM and commonly the apparent initial susceptibility is measured at relatively higher fields. The initial slope extracted as indicated previously, represents then, the apparent initial susceptibility, which can be also characteristic of the material, but is generally an overestimation of the intrinsic initial susceptibility. The initial slope for the nanophase samples (nanohematites and ferrihydrites) was defined as the slope of the best-fit line

through the points in the field range from –500 G to 500 G, which includes the four central data points. All of these parameters are analyzed for the data of the samples considered in this study in the following chapter (Chapter 8: Analysis, Interpretation and Discussion).

7.2 Magnetic Granulometry

For the nanophase samples, it is possible to extract intrinsic information from the magnetization-field data. Rancourt *et al.* (2004) have developed a method for calculating the magnetic granulometry of superparamagnetic particles. In this method, a graph of the mass susceptibility ($\chi_g = \frac{M_g}{H}$) versus field squared (H^2) can be used to extract the number average of the mass of the superparamagnetic particles (m_p) and the number average of the supermoment of the particles (μ). This method therefore yields information about intrinsic properties of the samples. This is very important when studying nanophase samples since the basic extractable parameters discussed in the previous section (7.1) may not be representing actual saturation values and therefore may not be providing reliable interpretable parameters.

Theoretically, the graph of χ_g versus H^2 should be initially linear and then it should deviate from the linear behaviour to larger susceptibility values, at larger field values. The slope (C_2) and intercept (C_1) of the best-fit line through the points showing linear behaviour can be used to calculate the previously mentioned supermoment (μ) and mass of the superparamagnetic particles (m_p) using the following equations:

$$\mu = k_B T \left(\frac{15 C_2}{C_1} \right)^{\frac{1}{2}} \qquad (7\text{-}1),$$

$$m_p = 5k_B T \frac{C_2}{C_1^2} \qquad (7\text{-}2),$$

where k_B is Boltzmann's constant and T is the temperature in Kelvin.

This procedure of extracting the average mass and average supermoment of superparamagnetic particles is applied in the following chapter (Chapter 8: Analysis, Interpretation and Discussion) to the nanophase samples (nanohematites and ferrihydrites) within the analysis of the data of this thesis.

7.3 Estimation of Additional Parameters

As shown in the previous section (7.2), the most reliably extracted parameters from the magnetization-field cycles at room temperature for the nanophase samples are the average supermoment of the SP particles, μ, and the average mass of the SP particles m_p. Other parameters such as the number of moments contributing to the supermoment (μ'), the number of magnetic moments within a particle (n), and the size (d) of the particles, can be estimated based on several assumptions. Table 7.1 shows the association between the directly extracted parameters and the estimated parameters based on assumed known parameters.

Extracted Parameters	Assumed Parameters	Estimated Parameters
μ	g, J, μ_B	μ'
m_p	M_a	n
	ρ, shape	d

Table 7.1 Physical parameters estimated from the extracted supermoment and particle mass

The size (d) of the SP particles can be estimated from the particle mass if we assume that the particles have a spherical shape. Consequently, by rearranging the expression of the

volume of a spherical particle, we obtain the following expression for the diameter of the particle:

$$d = \left(\frac{6m_p}{\pi\rho} \right)^{\frac{1}{3}} \qquad (7\text{-}3),$$

where ρ is the assumed density of hematite and ferrihydrite: 5.26 g cm^{-3} and 4.0 g cm^{-3}, respectively.

The number of atomic moments contributing to the supermoment (μ') is related to the supermoment (μ) by the expression:

$$\mu = \mu' g J \mu_B \qquad (7\text{-}4).$$

Here it is assumed that the orbital momentum, L, is zero for Fe^{3+} and therefore the total angular momentum J is equal to the spin momentum, S, which is assumed as the saturation atomic moment magnitude, $\frac{5}{2}$; consequently, the Landé g-factor (g) has a value of 2.

Additionally, using the particle mass value (m_p), it is possible to calculate the number of magnetic cations (Fe^{3+}) in a particle, n, assuming the molar mass of a molecule of ferrihydrite or nanohematite containing one iron cation (M_a):

$$n = \frac{m_p}{M_a} \qquad (7\text{-}5),$$

where the molar mass M_a is calculated using the following expression:

$$M_a = \frac{M_m}{Z \times N_A} \qquad (7\text{-}6).$$

M_m is the molecular weight of the hematite (Fe_2O_3) or ferrihydrite using any of the commonly assigned general chemical formulas ($Fe_5HO_8 \cdot 4H_2O$ or $5Fe_2O_3 \cdot 9H_2O$ or $Fe_2O_3 \cdot 2FeOOH \cdot 2.6H_2O$). Z is the number of formula units per unit cell in hematite and ferrihydrite: 4 and 6, respectively (Cornell and Schwertmann, 1996), and N_A is Avogadro's number. Thus, by using equation 7-6, it is assumed that all of the samples studied are consistent with the stoichiometry represented by the chemical formula assumed.

All of the above additional parameters are calculated for the ferrihydrite and nanohematite samples and discussed in the following chapter (Chapter 8: Analysis, Interpretation and Discussion).

Chapter 8- Analysis, Interpretation and Discussion

8.1 Microcrystalline Hematites

8.1.1 Hysteresis Cycles – Basic Hysteresis Parameters

The magnetization-field curves for the microcrystalline hematite samples presented in chapter 6 (Presentation of Measured Data: figures 6.1 to 6.15) show wide cycles therefore they show the hysteresis phenomenon. This fact confirms that all of these samples retain remanence after an external field is applied, meaning that they are not superpaparamagnetic. In fact, they show hysteresis curves typical of single-domain particles; multidomain particles would exhibit a different type of hysteresis curve, where the coercivities and remanence are smaller (Dunlop and Özdemir, 1997). Single-domain (SD) behaviour for hematite has been previously observed in a broad particle size range approximately from 275 Å to 150,000 Å (Banerjee, 1971) and even up to 1,000,000 Å (0.1 mm) for metastable SD behaviour (Kletetschka and Wasilewski, 2002). The previously estimated particles sizes for our samples range from 200 Å to 2500 Å (section 4.1.2). Consequently, the hysteresis curves observed and the estimated sizes confirm that our microcrystalline hematite samples are constituted of single-domain particles.

Figures 8.1 to 8.3 show the variation of the different basic hysteresis parameters defined in section 7.1. The line connecting the points is an aid to the eye for observing the variation among the parameters. The solid points indicate the samples that present a Morin transition above 4.2 K. There seems to be no systematic trend between the presence of a Morin transition or the synthesis temperature used and the hysteresis parameters considered.

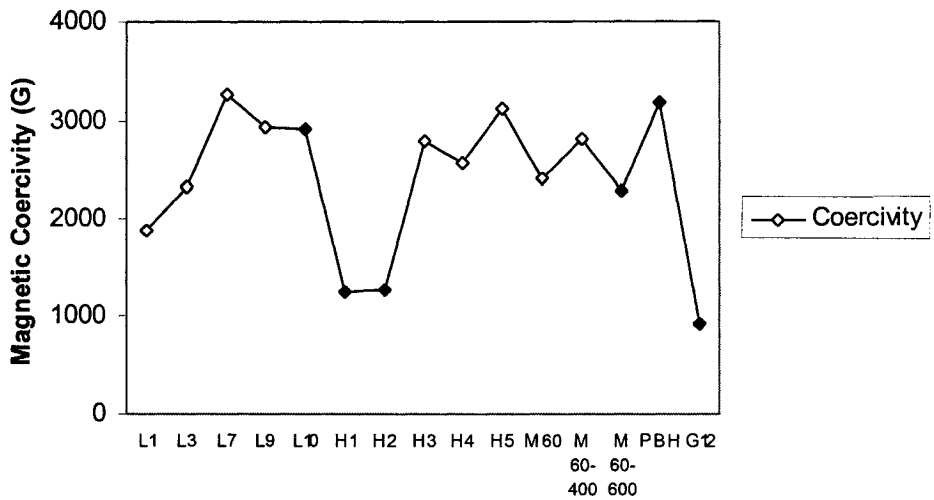

Figure 8.1 Variation of magnetic coercivity values (H_c) for the microcrystalline hematite samples

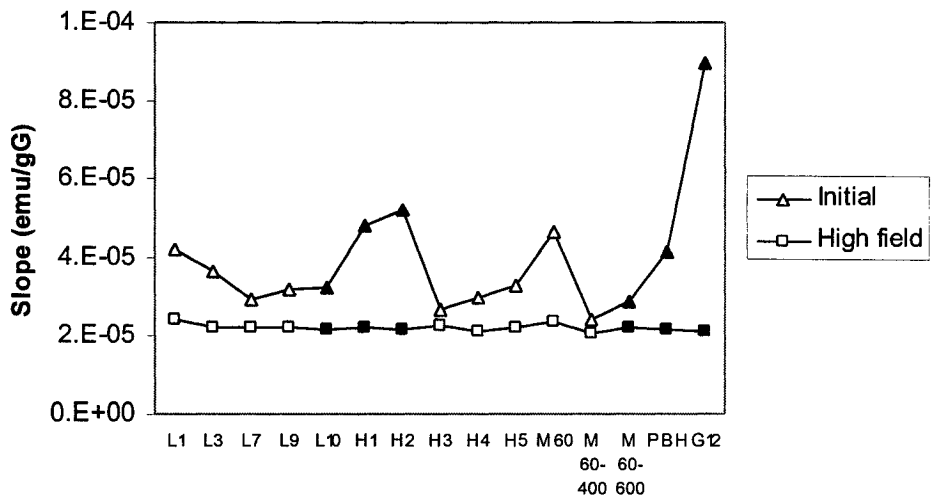

Figure 8.2 Variation of extracted slope values (χ_0, χ_d) for the microcrystalline hematite samples

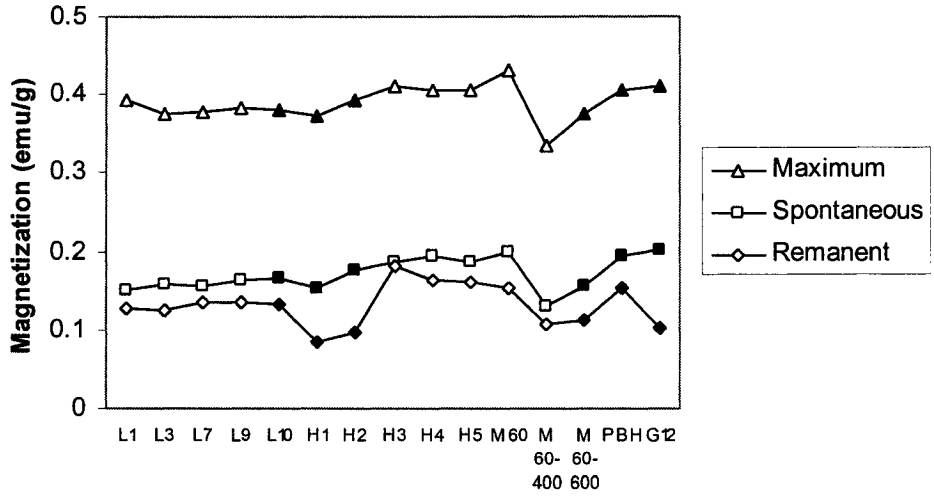

Figure 8.3 Variation of extracted magnetization values (M_{max}, M_r, and M_s) for the microcrystalline hematite samples

A major observation in the hysteresis curves of the microcrystalline hematite samples considered (figures 6.1 to 6.15) is that they do not show a saturated horizontal line at high fields. The high field region ($|H| \geq 6$ kG) shows saturating magnetization curves that converge to a positive slope line. The basic hysteresis parameter called demagnetization slope, χ_d, characterizes this high field slope. When compared with the other extracted parameters (figures 8.1 to 8.3), the demagnetization slope shows the smallest variation among the samples. The mean value of this high field slope for all samples (figure 8.1) agrees with the known value of the high field mass susceptibility for hematite of 2×10^{-5} emu/gG (O'Reilly, 1984). This value has been previously observed to be constant along the trigonal axis and along any direction within the basal plane for a single crystal, above the Morin transition temperature (Néel, 1953).

The high field mass susceptibility has been explained by Halgedahl (1995) as the result of two processes: 1) the rotation of spins within the basal plane towards the field direction, and 2) the increase of the net spontaneous moment as a result of the increase in the canting of the spins due to the effect of the applied field. However, the first process should most likely occur at relatively moderate fields, lower than the fields in the defined high field region, where the spins align along an easy magnetic direction such that the magnetization along the applied field direction is a maximum. The second process is most likely to occur after this first alignment with the field takes place and at higher fields, where the main effect of the field is now to increase the canting angle of the spins. Thus, the high field susceptibility should be mainly the effect of the increase of the canting angle of the spins.

In brief, the results presented here confirm that the high field linear region slope, which represents the high field mass susceptibility, is an intrinsic property for hematite samples that are large enough not to be superparamagnetic. It is related to the additional spin canting induced by high-applied fields. This additional canting is relatively constant for all samples and therefore it is not sensitive to the proportion of defects in the structure.

Considering the spin-canting angle for hematites of approximately 10^{-4} rad suggested by Dzyaloshinsky (1958), the expected spontaneous magnetization due to this canting for hematite is at least 0.05 emu/g. As seen from figure 8.3, the values of spontaneous magnetization (M_s) for all the microcrystalline hematite samples are higher than this value; they range from 0.1292 emu/g to 0.2026 emu/g. The defect moment can account for the rest of the spontaneous magnetization not due to the spin-canted moment. The defect moment in our microcrystalline hematite samples has its origin mainly in the presence of impurities and

vacancies in the crystalline structure, which cause an imperfect cancellation of the spins in the antiferromagnetic (AF) structure. Additionally, the surface moments, also caused by the imperfect cancellation of the AF structure as a result of the spatial limit imposed by the surface, can be a considerable contribution to the spontaneous moment for the case of small particles, such as the microcrystalline hematite samples considered in this study.

8.1.2 Magnetic Anisotropy

The remanent to saturation magnetization ratio $\left(\frac{M_r}{M_s}\right)$ is a parameter that can be used to recognize different magnetic anisotropy axis multiplicities in the basal plane of hematite samples (Dunlop and Özdemir, 1997). Dunlop (1971) has calculated theoretically a range of values for this ratio in agreement with different anisotropy multiplicities in the basal plane for an assemblage of randomly oriented SD grains of hematite. For a uniaxial anisotropy, the range of values of this ratio is from 0.500 to 0.637; for triaxial anisotropy, the range is from 0.750 to 0.955. The lower values of these ranges apply when the net moment is perfectly aligned with the maximum field, that is, where it is pulled out of the plane, if it is necessary, to be parallel to the applied field. The higher values apply when the net moment is still confined in the easy plane at the highest field attained. Figure 8.4 shows that the remanent to saturation magnetization ratio values for the microcrystalline hematite samples considered in this thesis are separated in the two predicted ranges of values: samples H1, H2 and G12 show values associated with uniaxial anisotropy; the rest of the samples are grouped within the values associated with triaxial anisotropy.

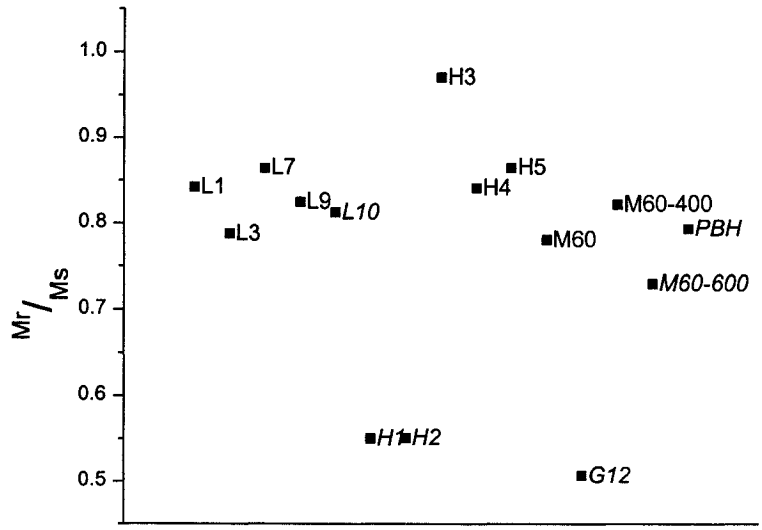

Figure 8.4 Remanent to saturation magnetization ratio for the microcrystalline hematite samples

The remanent to saturation magnetization ratio values associated with each anisotropy type cover a great part of the range expected theoretically therefore suggesting a different degree of alignment of the spins with the applied field for each sample of a specific anisotropy type. Actually, the magnetization of hematite is expected to be affected by substitutions of other ions, such as OH^- groups and H_2O, in the crystalline structure since these substitutions change the bond angles between atoms and consequently change the superexchange mechanism (Catti *et al.*, 1995). Following this line of thought, the differences in alignment suggested by the remanent to saturation ratio values for a given anisotropy type may be related to structural variations among the samples related to different proportions and arrangement of defects, which could limit or facilitate the physical rotation of the spins under the effect of an applied magnetic field.

The distinction in magnetic anisotropy type observed suggests that samples H1, H2 and G12 are very different from the other samples. In effect, they show extreme values in other basic hysteresis parameters, such as initial susceptibility (figure 8.5), where they have the highest values; coercivity (figure 8.6), where they have lowest values, meaning they are relatively soft materials, that is, a smaller field, in comparison to the other samples, is needed to change the magnetization; and remanent magnetization (figure 8.7), where they also show the lowest values. Additionally, they distinguish themselves for being the samples synthesized from a ferric nitrate solution (H1 and H2) and from a ferric sulphate solution with added sulphuric acid (G12) (section 4.1.1). It is also worth mentioning that all of these samples which show uniaxial anisotropy present an observable Morin transition.

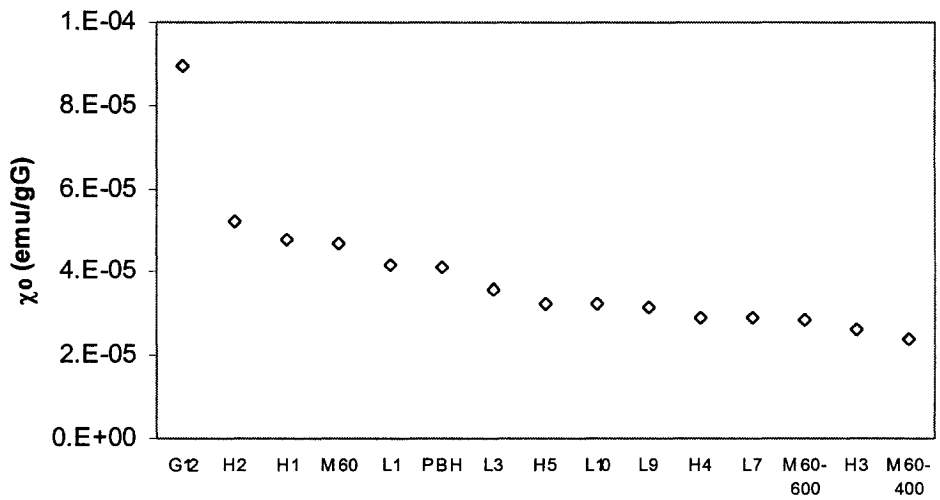

Figure 8.5 Initial slope of microcrystalline hematite samples in order of decreasing value from left to right. G12, H1 and H2 have the highest values

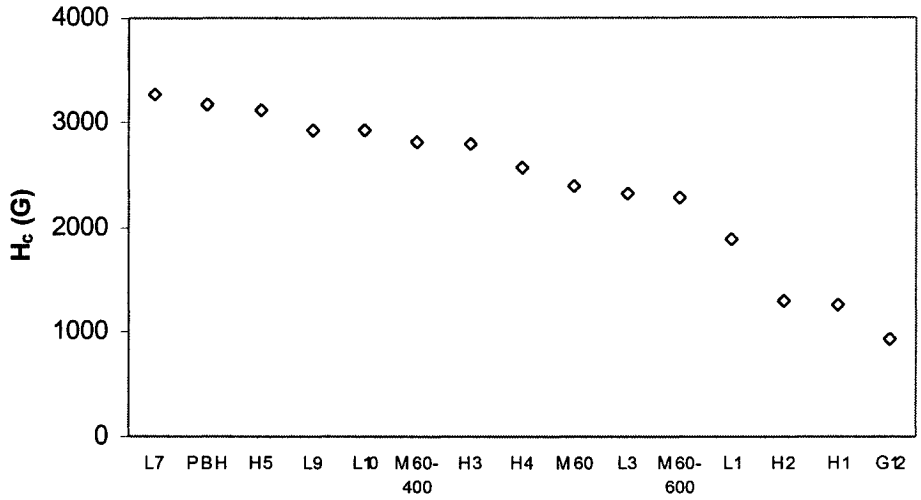

Figure 8.6 Magnetic coercivity of microcrystalline hematite samples in order of decreasing value from left to right. G12, H1 and H2 have the lowest values

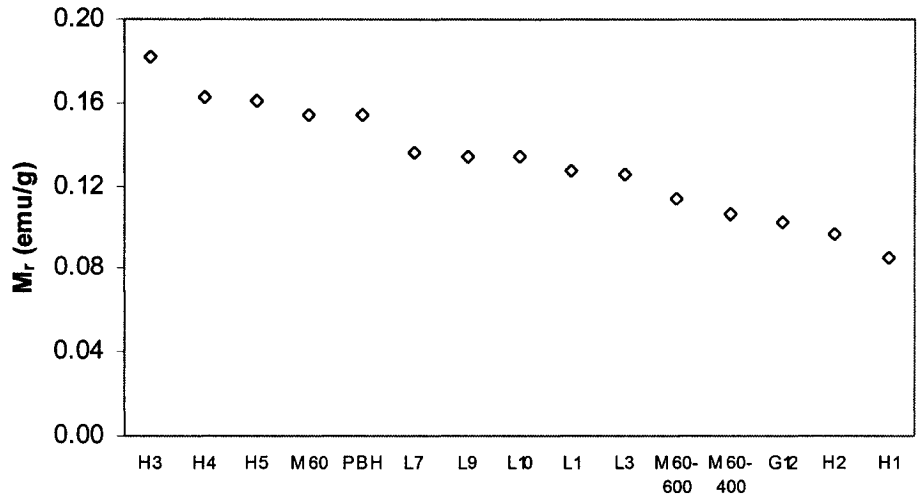

Figure 8.7 Remanent magnetization of microcrystalline hematite samples in order of decreasing value from left to right. G12, H1 and H2 have the lowest values

The observed uniaxial symmetry in the basal plane for these samples could be the result of a restriction that disabled the formation of the expected triaxial symmetry in the

basal plane of the hexagonal crystalline structure of hematite, which is confirmed to be present in the rest of the samples. Several studies of the anisotropy in the basal plane of synthetic and natural single crystals of hematite (e.g., Tasaki and Iida, 1963; Besser *et al.*, 1967; Porath, 1968) have concluded that the anisotropy should have a magnetoelastic origin due to internal or external stress. Dunlop (1971) studied synthetic powders of hematite samples and found uniaxial magnetoelastic anisotropy in some samples and triaxial magnetocrystalline anisotropy in others, and suggested the possibility of having both types of anisotropies in the basal plane. Particularly, Tasaki and Iida (1963) and Banerjee (1963) have found uniaxial anisotropy in synthetic single crystals and triaxial anisotropy in natural crystal specimens, respectively, and interpreted the uniaxial anisotropy as having a magnetoelastic origin caused by internal strain due to crystalline defects. Porath (1968) has shown that applying external compression within the basal plane induces uniaxial anisotropy in natural single crystals with easy direction of magnetization perpendicular to the compression. Compression along the trigonal axis induces greater triaxial anisotropy in the basal plane due to the reorientation of the crystalline structure in three sets of rhombohedral twins (Porath and Raleigh, 1967). Additionally, Rancourt (2001) has indicated that the dipolar shape anisotropy barrier can be the cause of a preferred magnetization axis parallel to the main elongation axis of a particle, and that the shape surface itself and surface roughness can cause deviant local magnetocrystalline anisotropies. In this sense, the uniaxial anisotropy suggested in samples H1, H2 and G12 could be caused by crystalline defects and / or probably an elongated shape of the particle. The triaxial anisotropy suggested for the rest of the samples

could be most probably representing the expected triaxial symmetry of easy magnetization directions in a hexagonal crystalline structure such as that in hematite.

8.1.3 The Annealed Series

The annealed series of samples includes the annealed M60 series (M60, M60-400 and M60-600) and PBH; they represent a group of hematite samples annealed at different temperatures: not annealed (M60), 400 °C (M60-400), 600 °C (M60-600), and 1000 °C (PBH). Figure 8.8 shows the change in magnetization for increasing annealing temperatures for this annealed series. There is not a general decreasing tendency in the magnetization values for higher annealing temperatures as has been observed previously for other hematite samples and that has been explained by the effect of the reduction of the defect moment (e.g., Gallon, 1968; Dunlop, 1971).

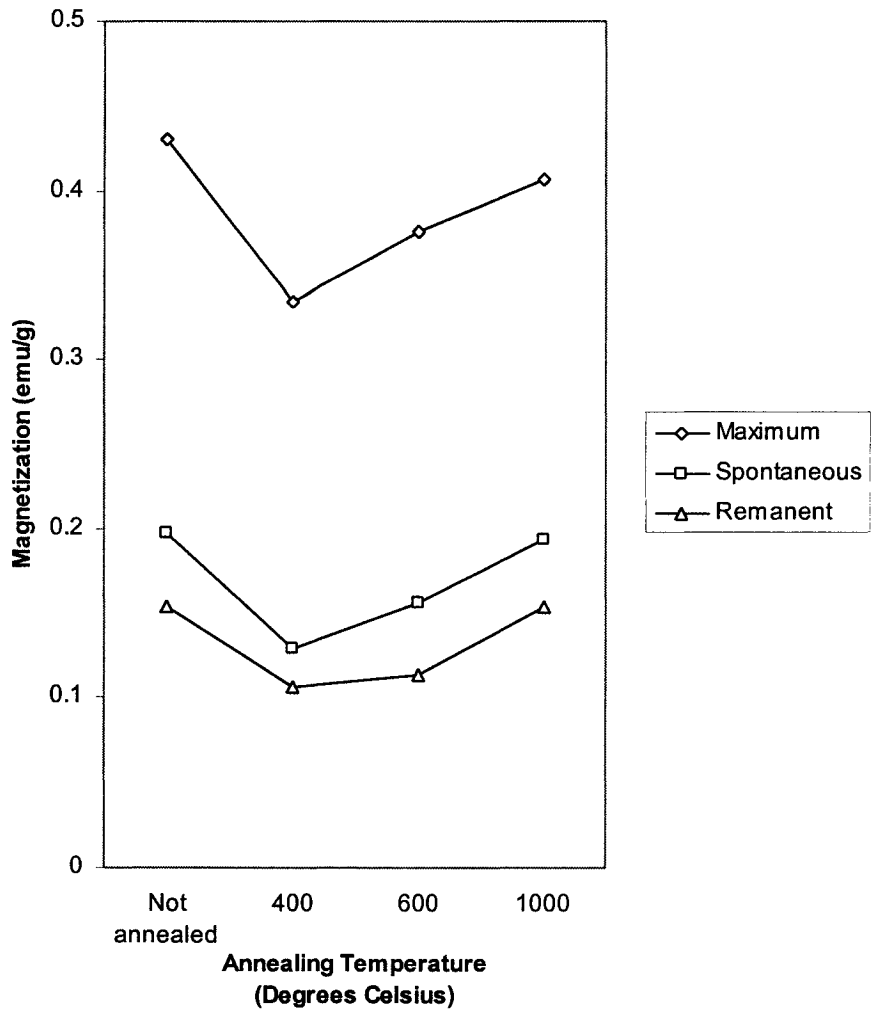

Figure 8.8 Magnetization values of the annealed series of hematite samples

The observed variation in mass magnetization values as the annealing temperature is increased suggests that the reduction of the defect moment is not the only process taking place during the process of annealing: the spin-canted moment might be affected by the repairing mechanism of the structure obtained through annealing. The spin-canted moment could be enhanced at the expense of the reduction of the defect moment. Dunlop (1971) has indicated that the annealing process not only reduces internal stress caused by the presence of

defects in the crystalline structure, but that it can also alter the nature of the spin-canted moment by altering the energy barriers opposing the canting of the spins. Dang *et al.* (1998) have suggested that the degree of spin-canting is very sensitive to lattice expansion, particle size, surface and shape effects, and presence of defects, all of which are altered during the annealing process. For the annealed series considered in figure 8.8, annealing to 400 °C reduces the magnetization. This reduction could be mainly due to the reduction of the defect moment caused by the repairing of the structure as the temperature increases. However, when annealing to higher temperatures (600 °C and 1000 °C) the magnetization increases. At these higher temperatures the defect moment continues to be reduced but at the same time, and in a greater degree in this case, the spin-canted moment may be increasing as a result of the less proportion and new configuration of defects in the structure as it is being repaired through the annealing process, which alters the energy terms opposing an additional canting of the spins. This interpretation suggests that the defect moment and the spin-canted moment are interdependent in the hematite structure, in that they both are affected by the alteration of defects caused by the annealing procedure.

Additionally, figure 8.8 shows that the magnetization in the not annealed sample (M60) is of similar magnitude to the magnetization in the sample annealed at the highest temperature (PBH). This suggests that the predominant defect moment in the not annealed sample is of similar magnitude as the enhanced spin-canted moment in the defect-free crystalline structure of the most annealed sample.

The susceptibilities of the annealed series are compared in figure 8.9. In contrast to the initial susceptibility, which shows a similar tendency to the magnetization values

discussed above, the high field susceptibility is relatively constant (as previously mentioned in section 8.1.1) for all the samples within the annealed series considered. The high field susceptibility is therefore independent of the main type of moment formation: defect moment or spin-canted moment. This is because, as indicated in section 8.1.1, this high field susceptibility is relatively insensitive to the proportion of defects in the structure. Consequently, the additional spin-canting induced by high applied magnetic fields depends neither on the spontaneous spin-canted moment nor the spontaneous defect moment in the sample.

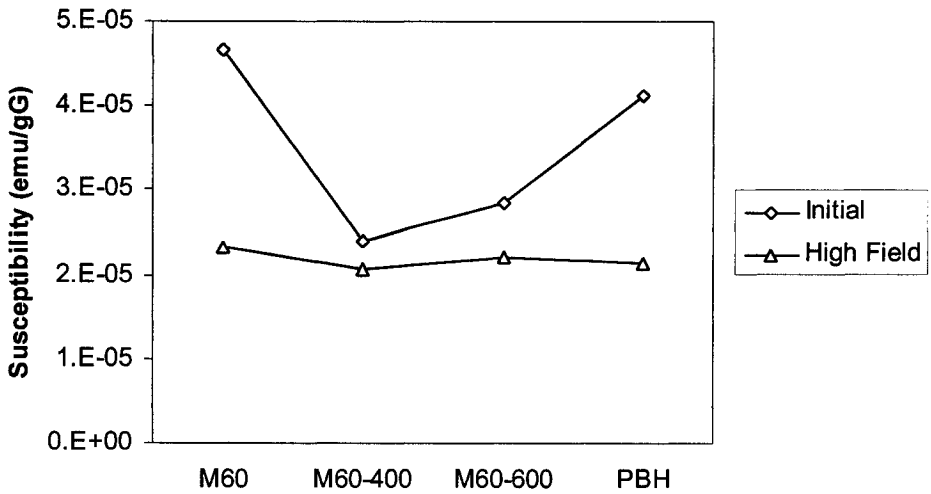

Figure 8.9 Magnetic susceptibilities of the annealed series of hematite samples

8.2 Ferrihydrites

8.2.1 Field Cycles – Basic Extractable Parameters

The field cycles of the ferrihydrite samples presented in chapter 6 (Presentation of the Measured Data: figures 6.16 to 6.20) show superparamagnetic behaviour. This is confirmed

by the fact that they show neither remanence nor coercivity (no hysteresis effect). Moreover, the values of magnetization reached could not be attributable to paramagnetism, since, as seen in section 2.1 (Theoretical Simulations of Paramagnetism), the magnetization values related to paramagnetism are much smaller. In general, the field cycles seem to show a linear behaviour, but actually, the samples FH-6L, FH-2L-N1 and FH-2L-N2 show a clear curvature. Figures 8.10 to 8.14 show for all of the ferrihydrite samples, the deviation of the data points from a linear fit through them, in magnitude of the percentage of the highest measured moment.

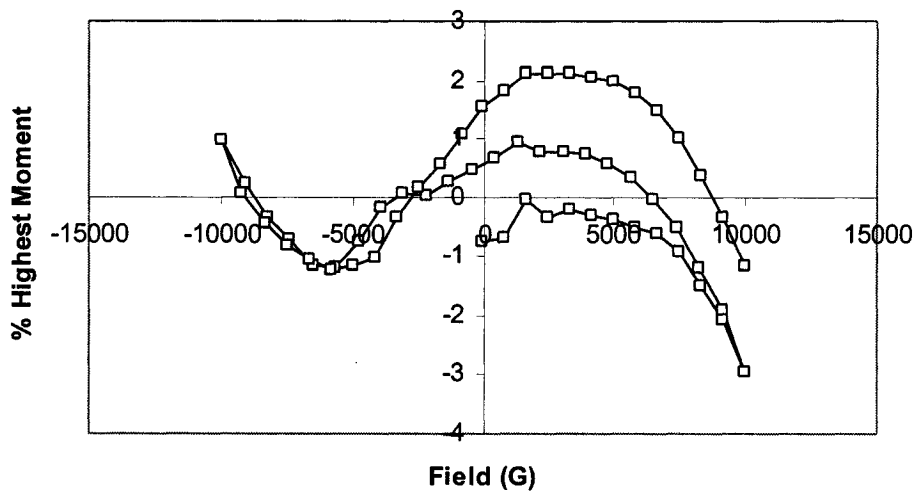

Figure 8.10 Deviation of data points from a linear fit through the field cycle of FH-6L

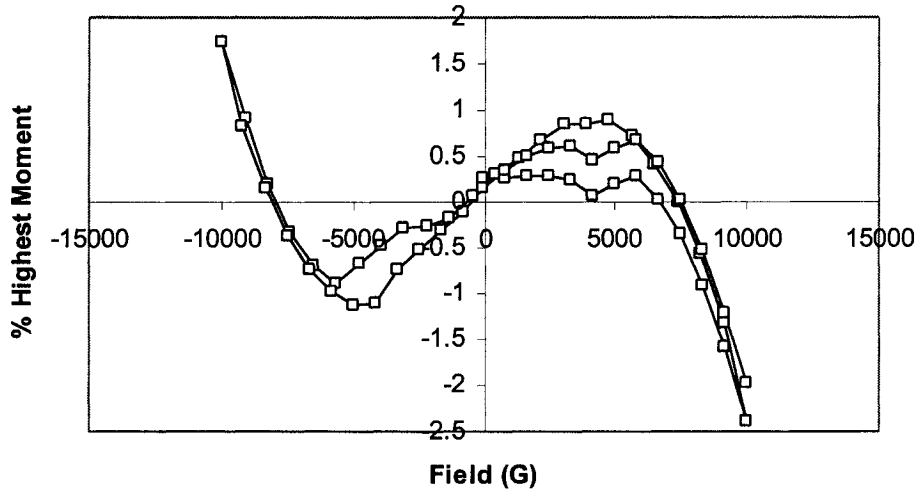

Figure 8.11 Deviation of data points from a linear fit through the field cycle of FH-2L-N1

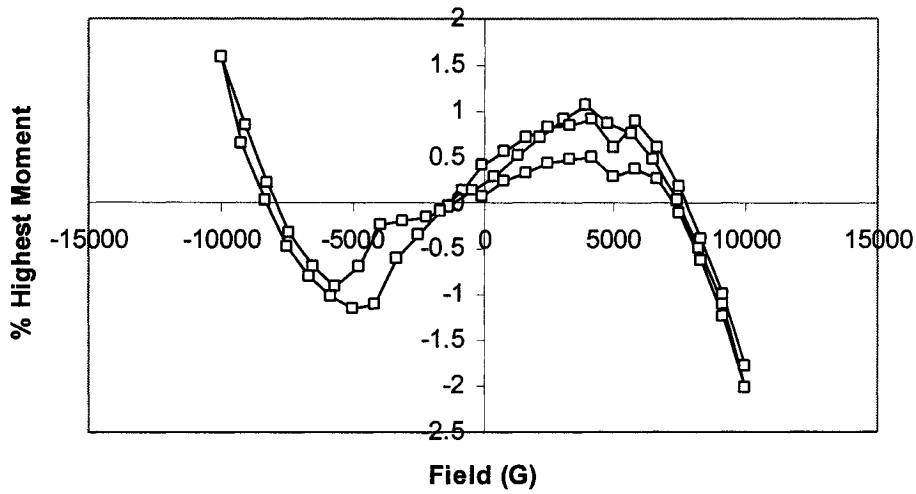

Figure 8.12 Deviation of data points from a linear fit through the field cycle of FH-2L-N2

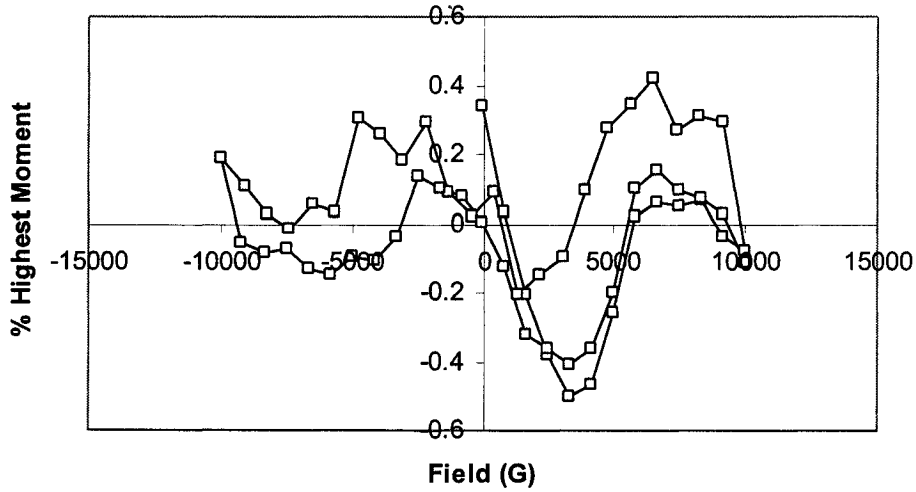

Figure 8.13 Deviation of data points from a linear fit through the field cycle of FH-2L-S

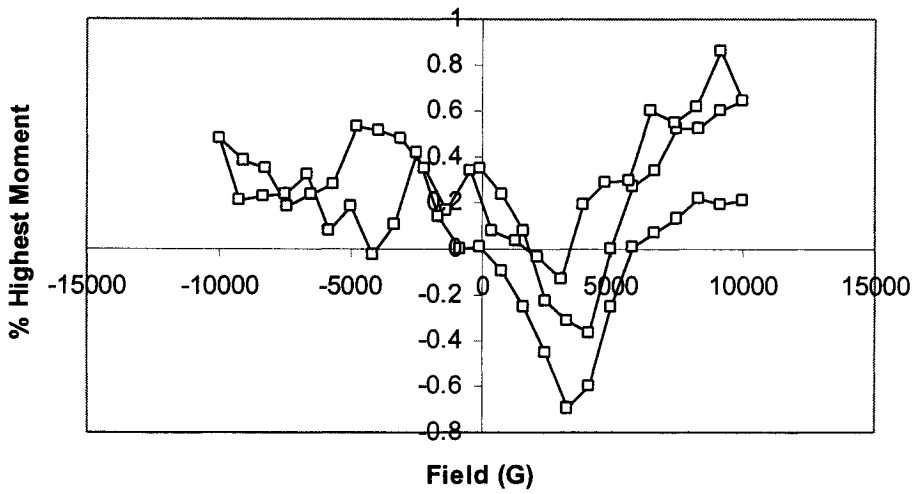

Figure 8.14 Deviation of data points from a linear fit through the field cycle of FH-2L-N3-P

The samples FH-6L, FH-2L-N1 and FH-2L-N2 show a clear pronounced curvature in the field cycle; the samples FH-2L-S and FH-2L-N3-P do not show a similar curvature to

these. The samples FH-2L-N1 and FH-2L-N2 show similar curvatures in addition to similar field cycles (Chapter 6: figures 6.17 and 6.18) and the same ^{57}Fe Mössbauer spectroscopy and pXRD results (section 4.3.2). This shows that the use of a different type of filter and the possible incorporation of it into the sample does not affect the reproducibility of magnetic properties for samples with identical synthesis conditions, as expected, since the addition of a small amount of diamagnetic material would not dramatically affect the magnetic response. In this sense, this also shows the extent to which two essentially identical syntheses yield identical samples.

The variation of the basic extracted parameters (M_s, M_{max}, χ_0, χ_d) among the ferrihydrite samples is shown in figures 8.15 and 8.16. The sample-to-sample variations of the parameters are all similar. In general, these parameters do not have the same meaning as in the single-domain microcrystalline hematites considered in section 8.1 since the ferrihydrite samples are superparamagnetic. The response of the superparamagnetic ferrihydrites to an applied field is based on different processes than the ones taking place in a magnetically blocked single-domain microcrystalline hematite. As a result, the basic parameters extractable from the magnetization-field cycles are not easily interpretable (Rancourt *et al.*, 2004). The magnetic granulometry method used in the following section (8.2.2) yields intrinsic parameters that are more reliable for interpreting the characteristics of the ferrihydrite samples.

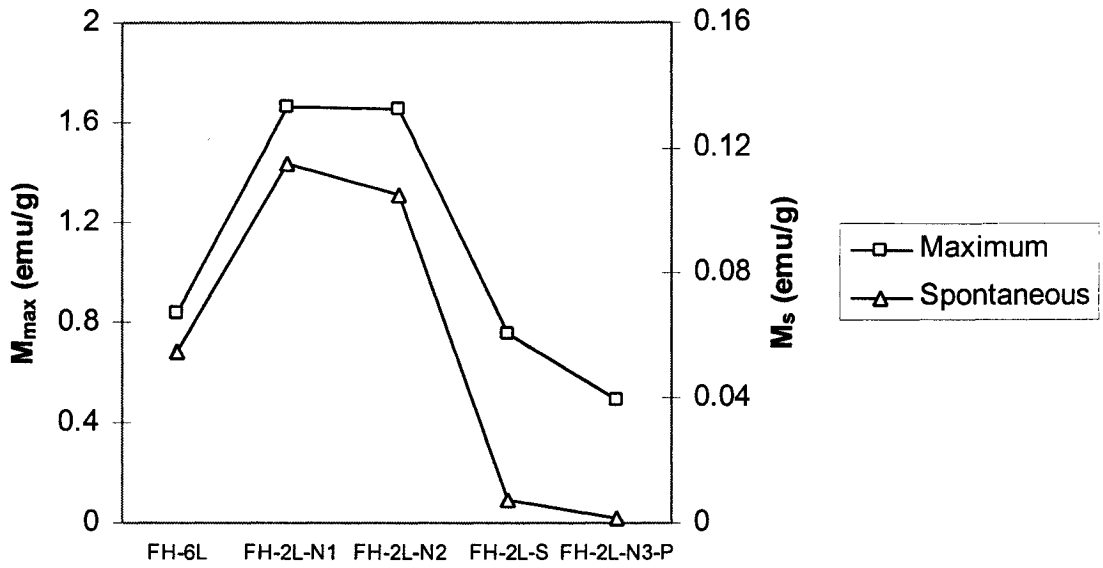

Figure 8.15 Variation of the extracted magnetization values (M_{max}, M_s) for the ferrihydrite samples. (The line connecting the points in this figure and in figure 8.16 is an aid to the eye for observing the variation of the extracted parameters among the samples considered)

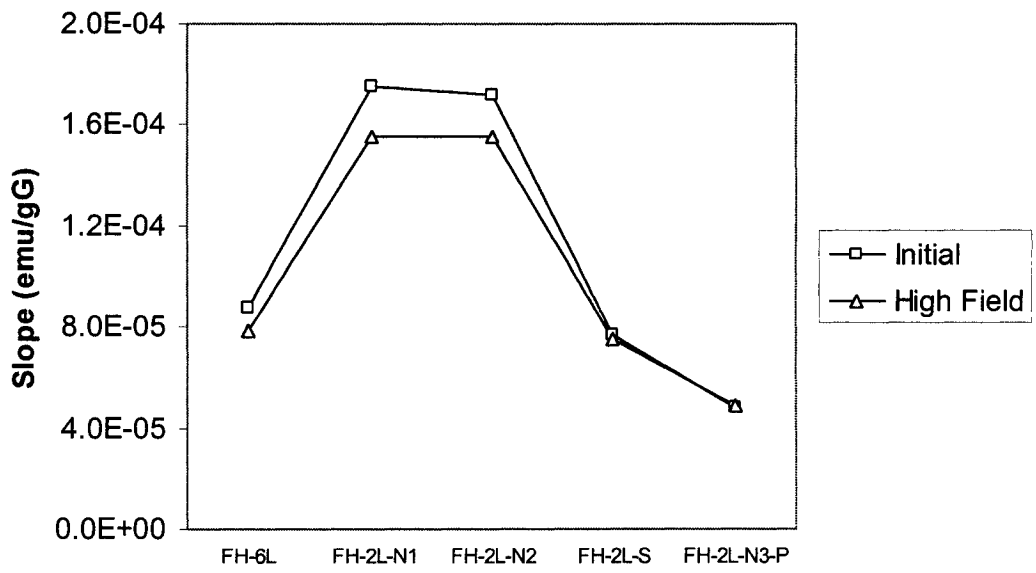

Figure 8.16 Variation of extracted slope values (χ_0, χ_d) for the ferrihydrite samples

8.2.2 Magnetic Granulometry

As indicated in chapter 7 (Data Analysis Methods), the number average mass (m_p) and number average supermoment (μ) of a superparamagnetic particle are parameters that can be extracted from the field cycle data using a graph of the mass susceptibility (χ_g) versus the field squared (H^2). This type of graphs for the ferrihydrite samples are shown in figures 8.17 to 8.21.

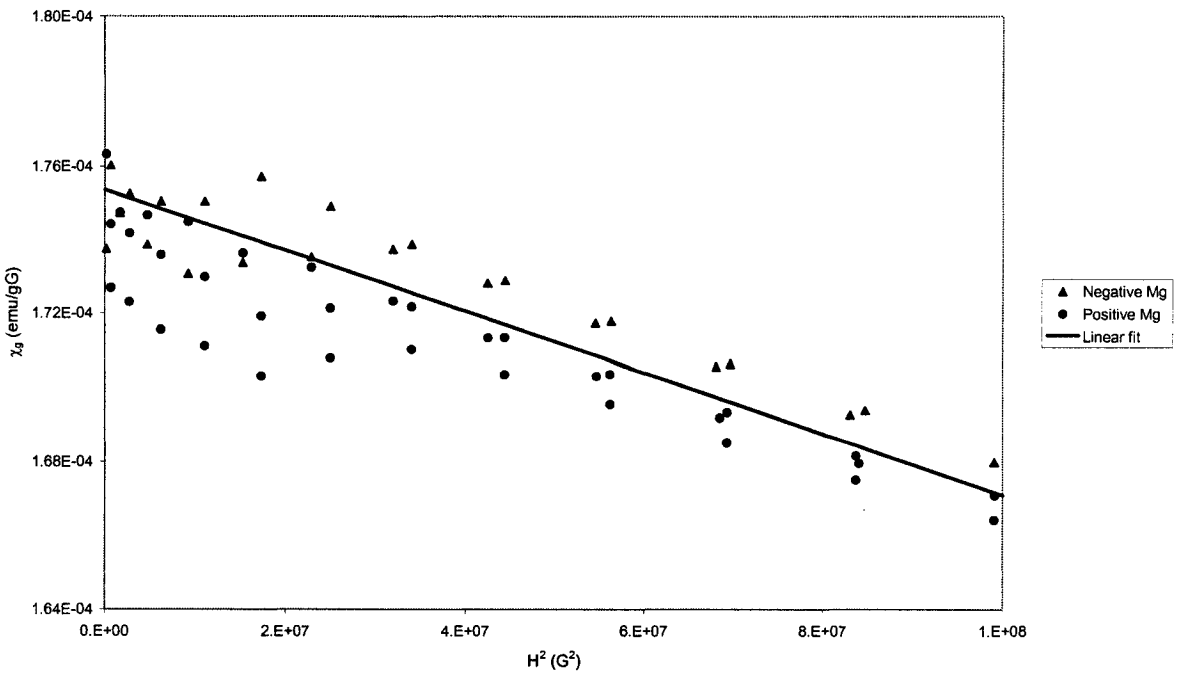

Figure 8.17 Mass susceptibility versus field squared graph for FH-2L-N1 showing linear fit of the high field region data and distinction between data corresponding to negative and positive magnetization values.

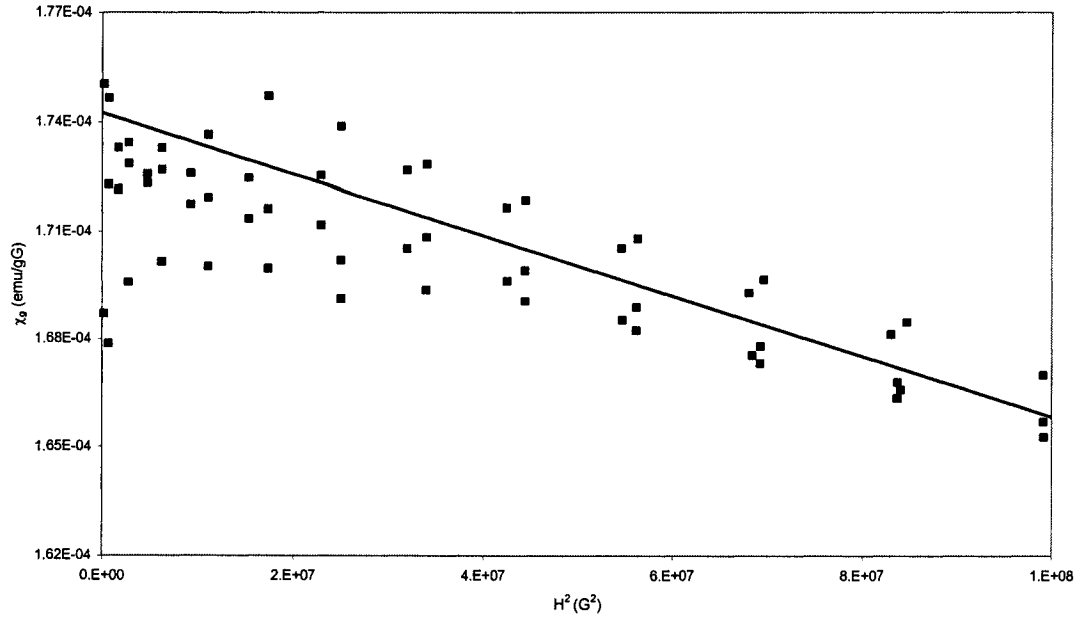

Figure 8.18 Mass susceptibility versus field squared graph for FH-2L-N2 showing linear fit of the high field region data

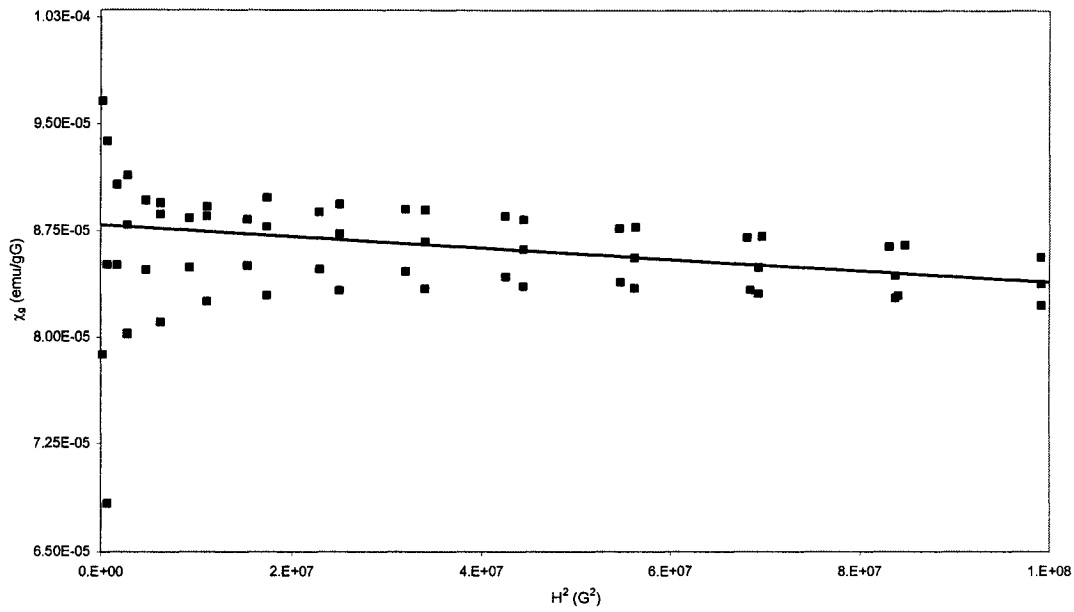

Figure 8.19 Mass susceptibility versus field squared graph for FH-6L showing linear fit of the high field region data

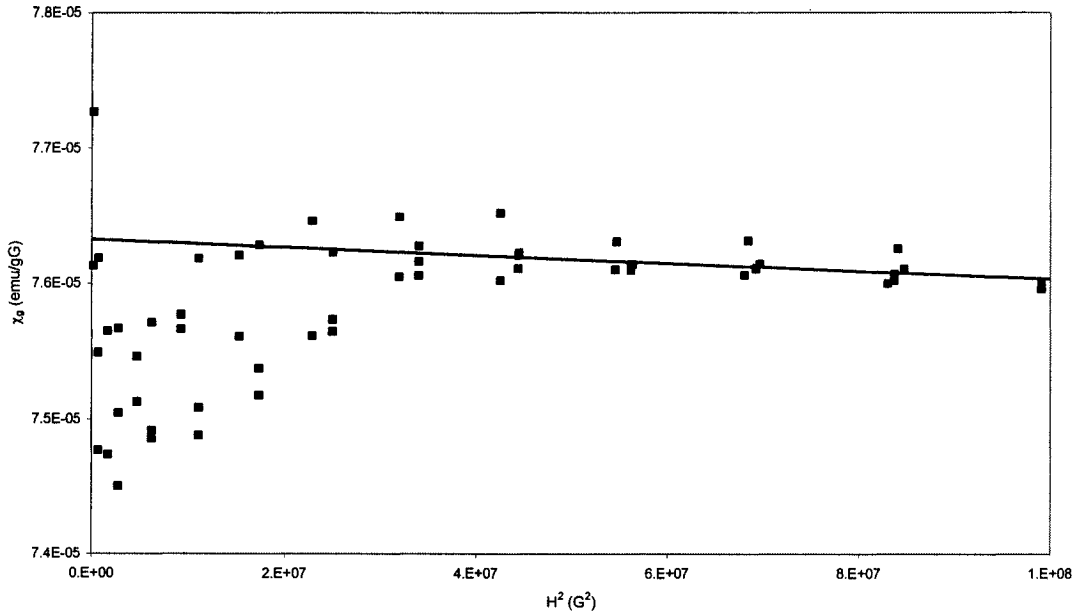

Figure 8.20 Mass susceptibility versus field squared graph for FH-2L-S showing linear fit of the high field region data

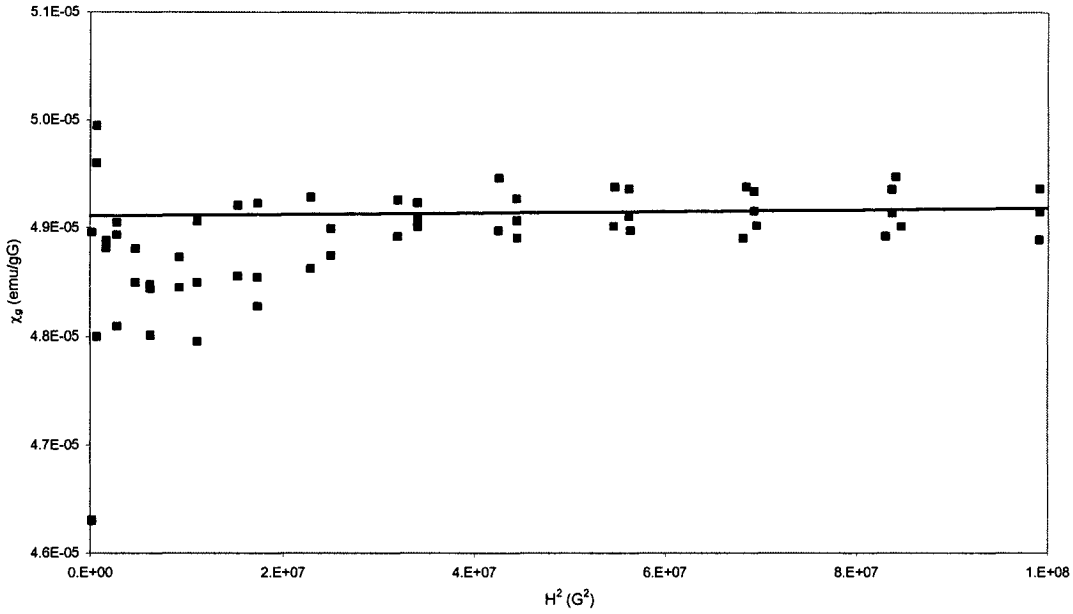

Figure 8.21 Mass susceptibility versus field squared graph for FH-2L-N3-P showing linear fit of the high field region data

These graphs show big variations in susceptibility at very low fields probably due to inter-particle dipolar interactions (Rancourt *et al.*, 2004). For all graphs, there is a linear region at higher fields ($H^2 \geq 3 \times 10^7$ G^2) where a best-fit line can be drawn to extract the values of the slope (C_2) and intercept (C_1) used to calculate μ and m_p. Although this region shows linear behaviour, the data does not fall into a single line. This is the effect of a small constant shift present in all the magnetization curves, which becomes noticeable when comparing absolute values of M_g with respect to field. The susceptibility values coming from negative magnetization values are shifted from the susceptibility values that come from positive magnetization values. Figure 8.17 shows clearly this effect for the sample FH-2L-N1. For this sample, the magnetization curve is shifted to lower values in the positive axis and to higher absolute values in the negative axis. Nevertheless, a line is fitted in the graph χ_g versus H^2 considering all the points in the linear region because this line gives a good estimate position of the data points if they were not shifted relative to one another. The line is fitted considering the precision errors in the susceptibility values, which are relatively constant for all the points in this region and consequently the extracted slope (C_2) and intercept (C_1) have errors associated with these precision errors.

Table 8.1 presents the calculated values of average mass (m_p) and supermoment (μ) of the superparamagnetic particles in the ferrihydrite samples along with the derived intrinsic mass magnetization $\left(=\frac{\mu}{m_p}\right)$, both in emu/g units and in Bohr magnetons per iron atom (μ_B/Fe). Figures 8.22 to 8.24 show graphically these calculated values.

Sample	Supermoment ($\times 10^{-18}$ emu)	Supermoment (μ_B)	Mass ($\times 10^{-18}$ g)	Intrinsic Mass Magnetization (emu/g)	Intrinsic Mass Magnetization ($\times 10^{-2}$ μ_B/Fe)
FH-6L	3.29 (1)	355 (1)	1.028 (6)	3.21 (2)	5.34 (4)
FH-2L-N1	3.365 (3)	362.9 (3)	0.5376 (8)	6.26 (1)	10.61 (2)
FH-2L-N2	3.386 (3)	365.1 (3)	0.5481 (1)	6.18 (1)	10.84 (2)
FH-2L-S	0.98 (4)	106 (4)	0.1055 (8)	9.3 (8)	18 (2)
FH-2L-N3-P	0.55 (9)	60 (9)	0.05 (2)	11 (4)	20 (7)

Table 8.1 Calculated values of supermoment and mass of SP particles in ferrihydrites and derived intrinsic magnetization

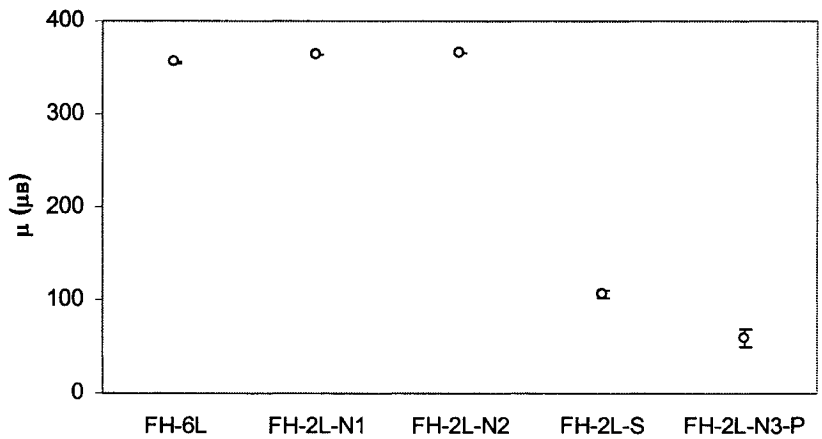

Figure 8.22 Average supermoment of SP particles in the ferrihydrite samples

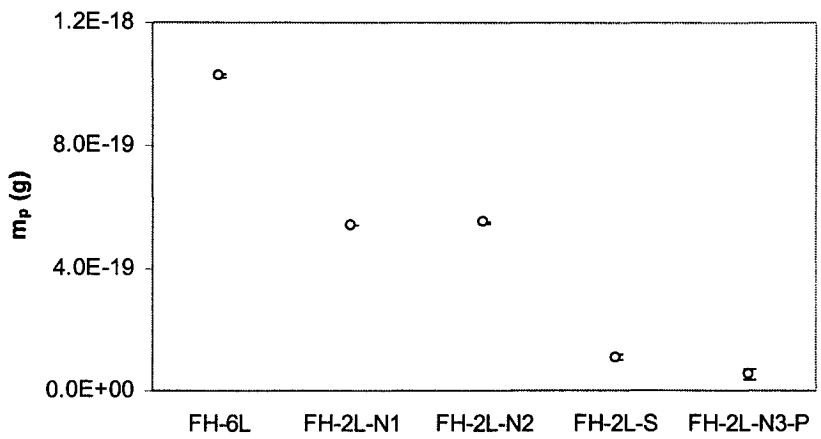

Figure 8.23 Average mass of SP particles in the ferrihydrite samples

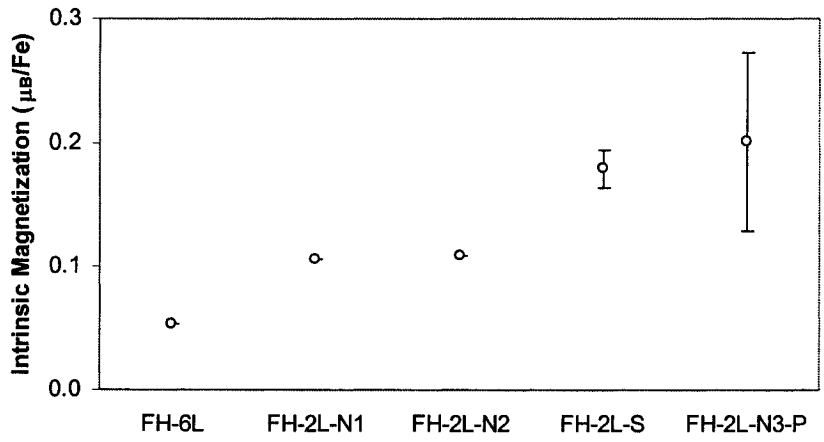

Figure 8.24 Intrinsic mass magnetization of SP particles in ferrihydrite samples

The 2-line ferrihydrites: FH-2L-N1 and FH-2L-N2 have a larger intrinsic magnetization than the 6-line ferrihydrite but they show a smaller particle mass. 2-line ferrihydrites are structurally more disordered than 6-line ferrihydrites (e.g., Eggleton and Fitzpatrick, 1988; Janney *et al.*, 2000; Janney *et al.*, 2001). A greater structural disorder implies less compensation of the spins within the antiferromagnetic structure and this imperfect cancellation of the magnetic moments is the origin of the net spontaneous magnetic moment. In this sense, the higher values of intrinsic magnetization of the 2-line ferrihydrites: FH-2L-N1 and FH-2L-N2, with respect to the values of the 6-line ferrihydrite: FH-6L, is a consequence of the greater structural disorder in 2-line ferrihydrites.

The supermoment and particle mass is greatly decreased for the samples FH-2L-S and FH-2L-N3-P, but they show the highest intrinsic magnetization values. Consequently, the small supermoment values are due to the fact that they have a small particle mass. The co-

precipitated sulphur and phosphate in these samples may have disabled further growth of the particle during the synthesis therefore resulting in smaller particles. The greater intrinsic mass magnetization in FH-2L-S and FH-2L-N3-P is caused by the presences of sulphur and phosphate, respectively, which represent defects in the crystalline structure that impede the compensation of the spins within the AF structure therefore resulting in the net supermoment.

8.2.3 Estimation of Additional Parameters

The estimated particle sizes for the 2-line ferrihydrites and for the 6-line ferrihydrite are shown in table 8.2. The 6-line ferrihydrite shows the largest size. These size dimensions are in agreement with previous observed sizes of ferrihydrite samples (e.g., Eggleton and Fitzpatrick, 1988; Janney *et al.*, 2000)

Sample	Particle Size (nm)
FH-6L	7.89 (2)
FH-2L-N1	6.355 (3)
FH-2L-N2	6.396 (4)
FH-2L-S	3.69 (9)
FH-2L-N3-P	2.9 (3)

Table 8.2 Estimated particle sizes for the ferrihydrite samples

The estimated values of μ' and n are shown in figure 8.25 as a plot of one versus the other. This graph gives the notion of the percentage of iron cations in a particle contributing to the supermoment. A linear fit through the 2-line ferrihydrites pictures a possible linear relationship between μ' and n for this type of ferrihydrite. This linear fit was weighted by the precision errors in μ' and forced to go through the origin since for no magnetic moments in a

particle there should be no supermoment. The slope of this line suggests that 2.136 (1) % of the magnetic moments in a SP particle of 2-line ferrihydrites are actually contributing to the supermoment.

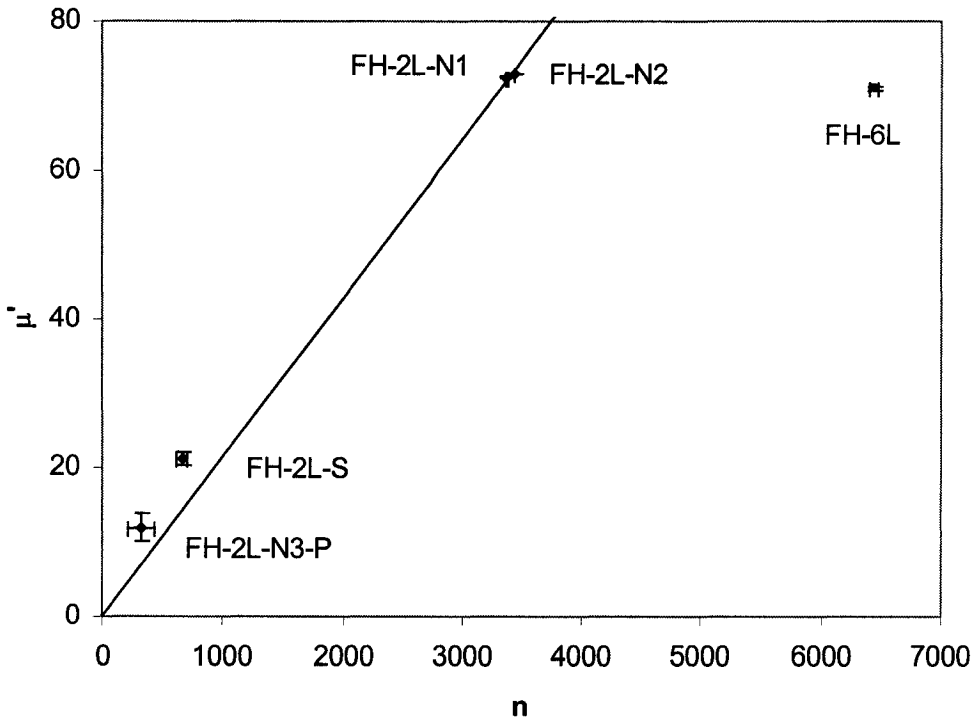

Figure 8.25 Relation between number of moments in a particle (n) and number of moments contributing to supermoment (μ') for the ferrihydrite samples

In figure 8.25, the 6-line ferrihydrite shows very different values from the 2-line ferrihydrites. It shows that a smaller number of moments in the 6-line ferrihydrite are contributing to the supermoment given the higher number of magnetic moments present in a particle, suggesting that the 6-line ferrihydrite has a more ordered structure, where the

magnetic moments cancel each other more, not just a greater size than the 2-line ferrihydrite samples. The values for the 6-line ferrihydrite do not seem to follow the tendency suggested by the 2-line ferrihydrite data points, suggesting a different type of structure. This is consistent with the work of Janney *et al.* (2000 and 2001) who find that there are significant structural differences between the 2-line and the 6-line ferrihydrites, as suggested by details of lattice-fringe geometry and electron nanodiffraction patterns. These authors suggest that the crystal structure of 2-line ferrihydrites is less developed than that of 6-line ferrihydrite. Additionally, they indicate that the most common structure in 6-line ferrihydrites is different from that of 2-line ferrihydrite, suggesting that the main difference between these two types of ferrihydrites is not only degree of crystallinity.

The possibility of a non-linear relationship of the form:

$$\mu' = An^{\alpha} \qquad (8\text{-}1),$$

was studied through a $ln(\mu')$ versus $ln(n)$ graph. A line in this graph can be represented as:

$$ln\mu' = ln(A) + \alpha ln(\mu') \qquad (8\text{-}2),$$

where α is the slope of this linear fit and $ln(A)$ is the intercept.

Figure 8.26 shows the $ln(\mu')$ versus $ln(n)$ graph for the 2-line ferrihydrites. The best-fit data through the data points considering the precision errors in $ln(\mu')$ (y-axis) yields an exponent α of 0.71 (2) and a proportionality factor A of 0.24 (4), suggesting the relationship: $\mu' = 0.24n^{0.71}$.

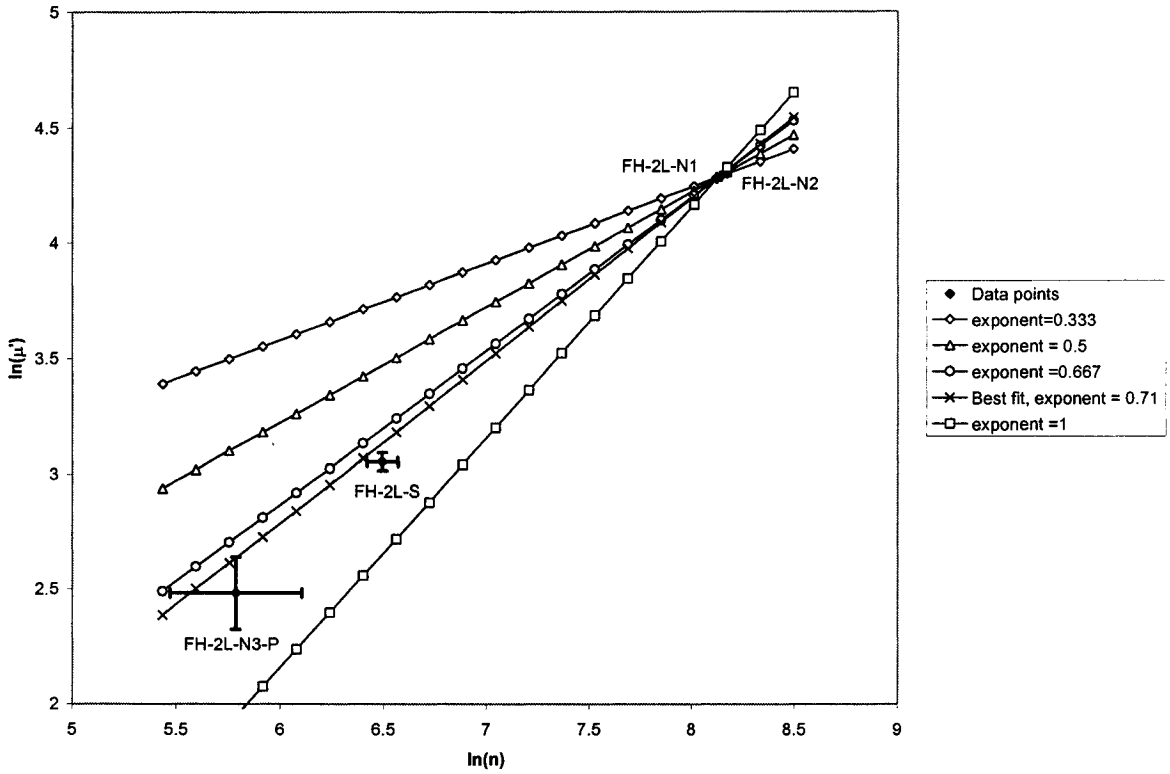

Figure 8.26 Linear fits through the data points of the ferrihydrites associated with different α values in the moment formation model $\mu'=An^{\alpha}$.

Figure 8.26 additionally shows lines that were fitted to go through the data imposing specific slope values, which represent different exponents α in the expression $\mu'=An^{\alpha}$ inspired by the models proposed by Neél (1961) that may represent the supermoment formation mechanism in superparamagnetic antiferromagnetic particles. An exponent of $^1/_2$ ($\mu'=An^{1/2}$) represents the situation where uncompensated moments occur randomly within the two AF sublattices. The exponent of $^2/_3$ ($\mu'=An^{2/3}$) represents the case where only the moments at the surface belonging to one of the AF sublattices contribute to the supermoment. The exponent $^1/_3$ ($\mu'=An^{1/3}$) represents the case where the uncompensated

moments at the surface occur randomly within the two AF sublattices. Additionally, the exponent of 1 ($\mu'=An$) could also be considered to represent the case of all the magnetic moments, or a direct fraction of them, are contributing to the supermoment.

As can be seen in this figure the lines with the slopes $^1/_3$ (=0.333), $^1/_2$ (=0.5) and 1 are not consistent with the four data points presented. The line with the $^2/_3$ slope cannot be regarded as inconsistent because it is within the range of 95% of probability (twice the precision error) of the data points. The line fitted with a slope of $^2/_3$ yields a proportionality factor of 0.32 therefore representing the relation $\mu'=0.32n^{2/3}$. In any case, the extracted α and A cannot be accounted as precise because the fit is based on only four points; additionally their errors are different and for that reason the fit is giving more weight to the data points with smaller errors. Nevertheless, figure 8.26 gives the notion of what simple model could be more representative of the data. In this sense, the moment surface model: $\mu' \propto n^{2/3}$ is the one that seems to represent better the data.

A less simple but possible supermoment mechanism is that of a combination of several simple models. The supermoment of an AF particle, such as ferrihydrite, could have a significant contribution from the uncompensated moments at the surface, which are expected in such small particles. Additionally random processes such as crystalline defects within the interior of the particle could contribute to the moment. Also, the presence of impurities could contribute as a defect moment throughout the particle. A relation representing all of this can be expressed by equation 8-3. Indeed, further data will be needed before such a more complete model can be evaluated.

$$\mu' = An^{2/3} + Bn^{1/2} + Cn \qquad (8\text{-}3).$$

8.3 Nanohematites

8.3.1 Field Cycles – Basic Extractable Parameters

In similarity to the ferrihydrite samples the field cycles of the nanohematite samples presented in chapter 6 (Presentation of the Measured Data: figures 6.21 to 6.24) show superparamagnetic behaviour; in contrast, they show an evident curvature. In general, the four nanohematite samples show similar field curves. This in agreement with the previous characterization performed on them where they also show similar results (section 4.3.2). The variations of the basic extracted parameters are shown in figures 8.27 and 8.28. As with the ferrihydrites, the sample-to-sample variations of the parameters are all similar.

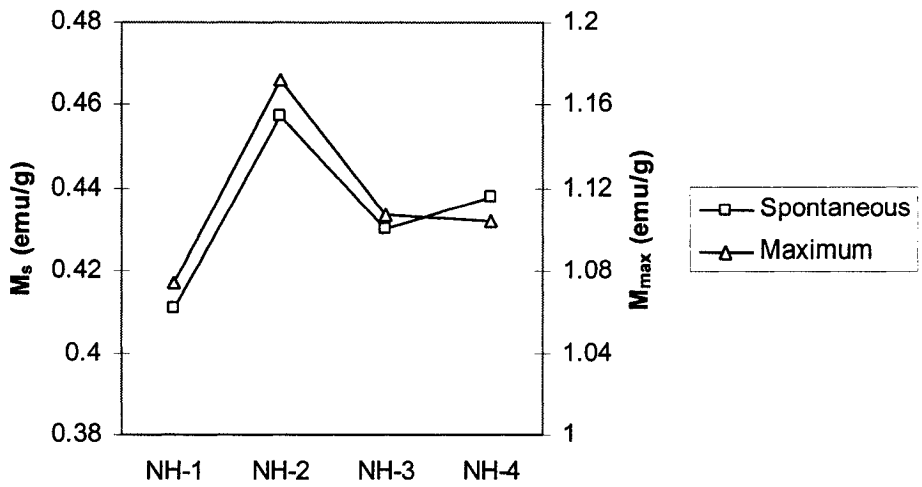

Figure 8.27 Variation of the extracted magnetization values (M_{max}, M_s) for the nanohematite samples. (The line connecting the points in this figure and in figure 8.28 is an aid to the eye for observing the variation of the extracted parameters among the samples considered)

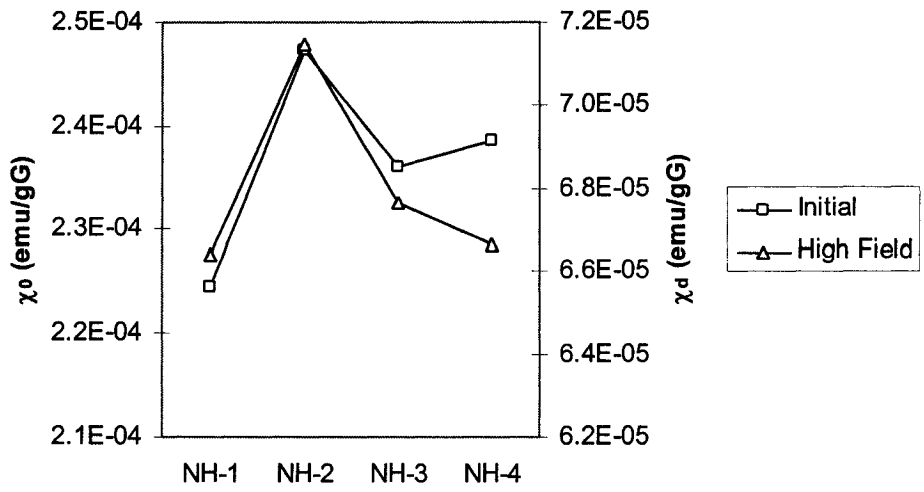

Figure 8.28 Variation of extracted slope values (χ_0, χ_d) for the nanohematite samples

In the same way as done with the ferrihydrites, we shall not interpret these basic parameters as previously done with the microcrystalline hematites. The main difference between the nanohematite samples and the microcrystalline hematite samples is that the former exhibits superparamagnetism while the latter show single-domain behaviour. Thus, the thermal condition of the superparamagnetic particles does not allow the basic extractable parameters to give intrinsic information about them. The exploration of the calculation of intrinsic parameters of the nanohematite samples is done in the following section.

8.3.2 Magnetic Granulometry

In Chapter 4: section 4.3.2, it is indicated that the RT MS spectra for the nanohematite samples suggest that the nanohematite fraction of the sample has its blocking temperature near RT, indicating that at this temperature the inter-particle interactions may

not be negligible. The magnetic granulometry method developed by Rancourt *et al.* (2004) is based on the assumption that these interactions are negligible. In this sense, this method should only be applied to these samples in a tentative way. Accordingly, and following the evidence that the field cycles show superparamagnetism, the method is applied in the same way as done with the ferrihydrite samples in section 8.2.2.

Figures 8.29 to 8.32 show the graphs of χ_g versus H^2 for the four nanohematite samples. Note that for these samples the data shows a curved behaviour for most of the field range. Nevertheless, we attempt to extract μ and m_p using a linear fit of the first five points with the smallest H^2 values that are predicted to approximately follow a linear behaviour before the data deviates into a curve. Figure 8.33 shows the best-fit line through these points for NH-1; the graphs for the rest of the nanohematite samples are similar.

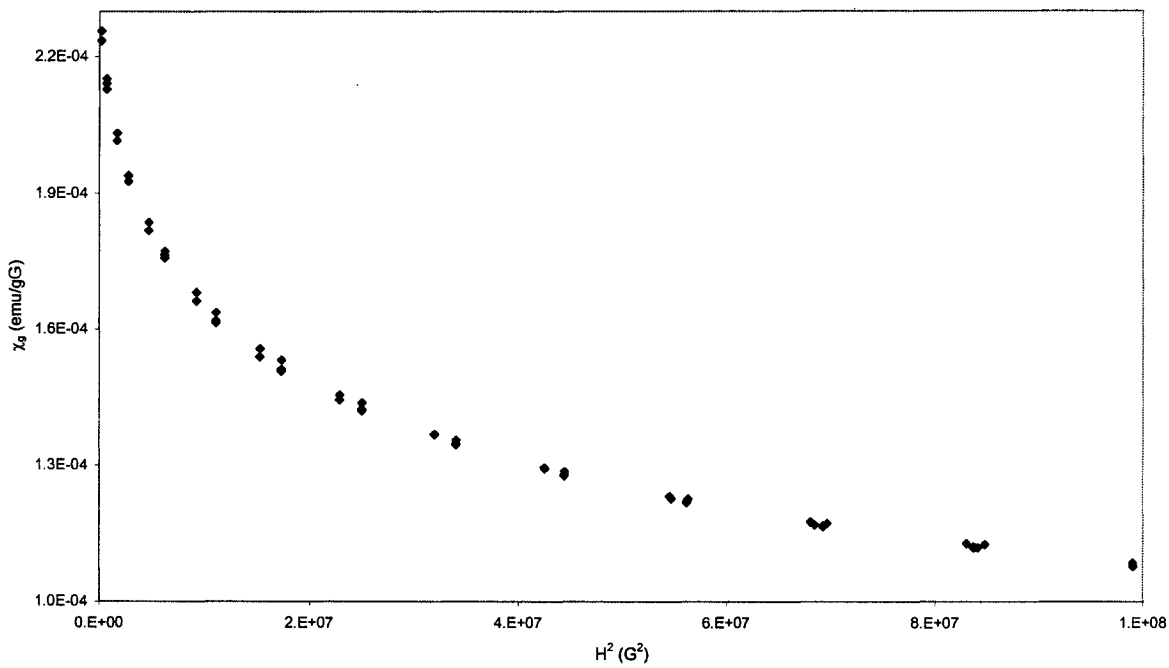

Figure 8.29 Mass susceptibility versus field squared graph for NH-1

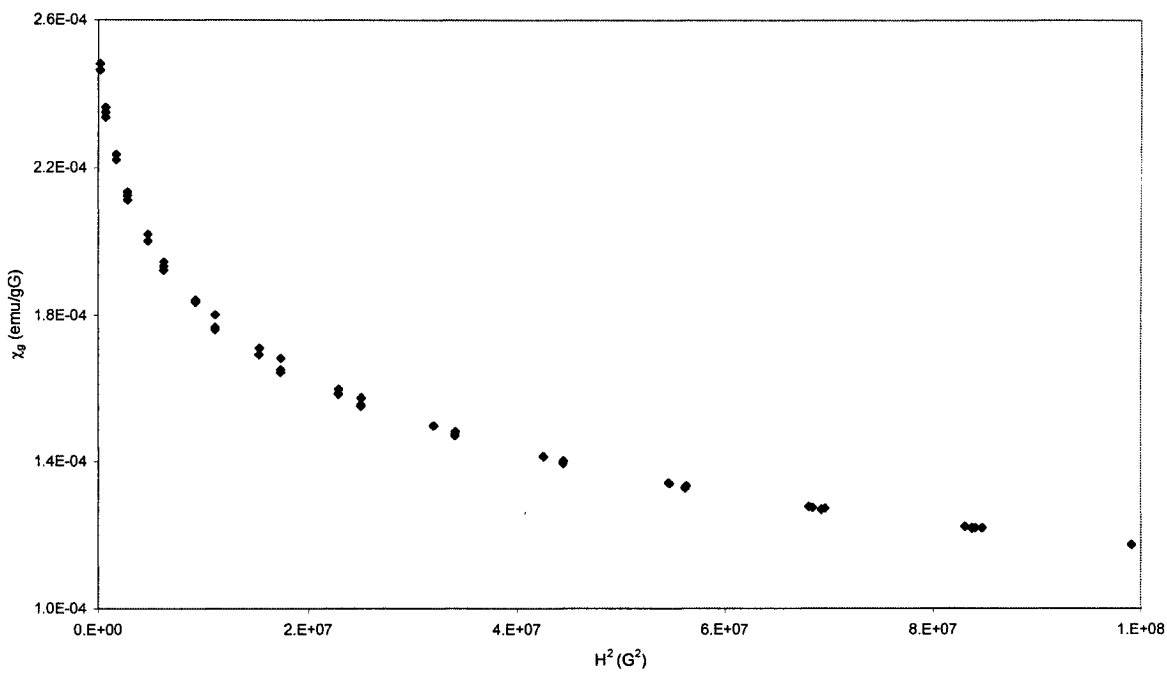

Figure 8.30 Mass susceptibility versus field squared graph for NH-2

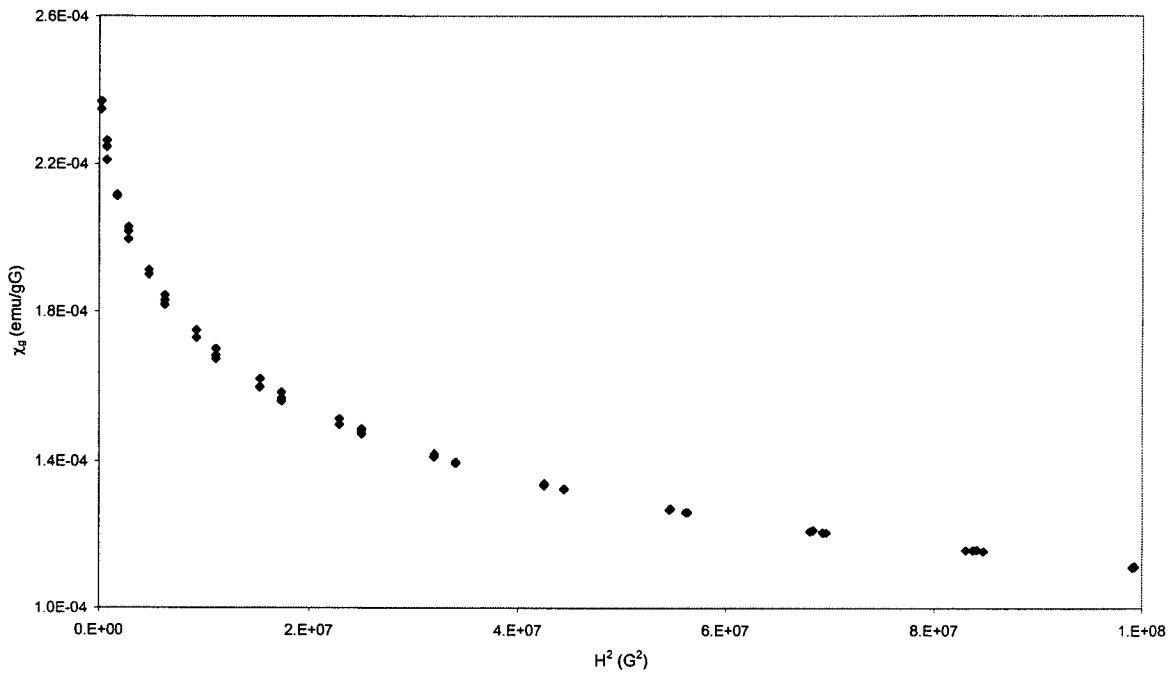

Figure 8.31 Mass susceptibility versus field squared graph for NH-3

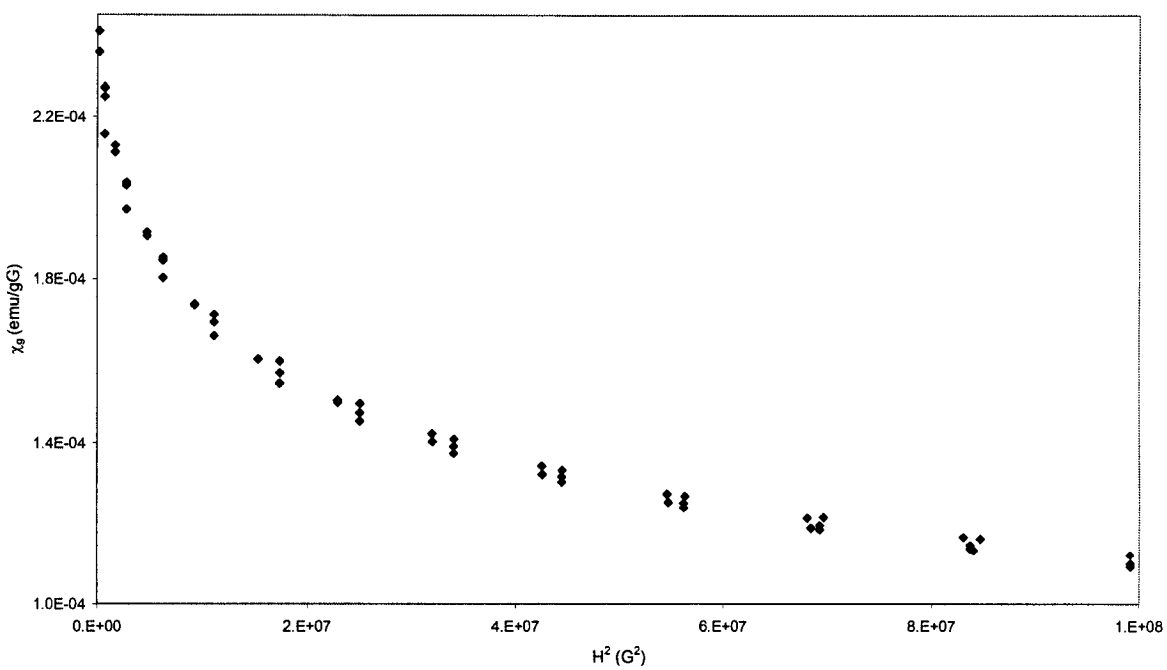

Figure 8.32 Mass susceptibility versus field squared graph for NH-4

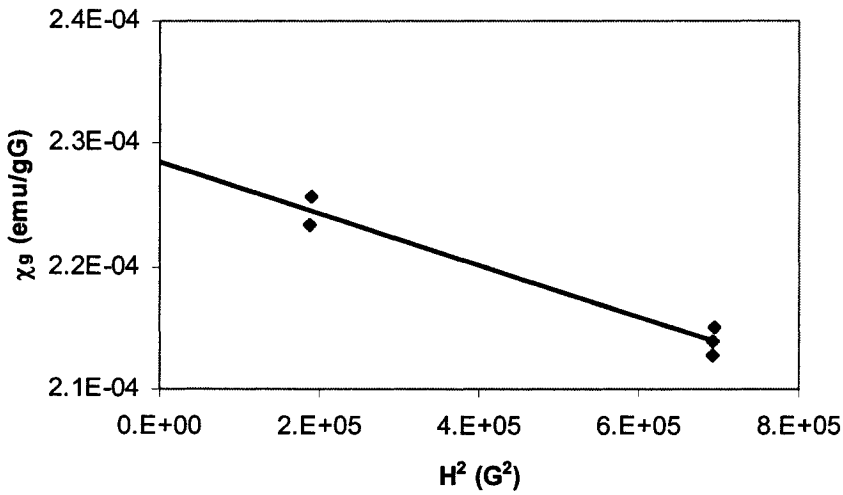

Figure 8.33 Linear fit used to extract μ and m_p in NH-1

The extracted average supermoment (μ) and average particle mass (m_p) for each nanohematite sample are shown in table 8.3 along with the calculated intrinsic mass magnetization. When comparing these intrinsic mass magnetization values with the extracted spontaneous magnetization value for the pure bulk hematite (PBH) sample (M_s=0.194 (2) emu/g), it can be seen that the intrinsic mass magnetization for the nanohematite samples is approximately three times higher than that of the single-domain PBH sample. The nanohematite samples show higher magnetization values because of their nanophase nature. The smaller size of the nanohematite particles makes the surface effects largely affect the magnetic properties because of the relatively greater fraction of magnetic moments that are not cancelled at the surface. Additionally, the smaller size allows the defects to have a more evident effect in the magnetic properties of the sample.

Sample	Supermoment ($\times 10^{-18}$ emu)	Supermoment (μ_B)	Mass ($\times 10^{-18}$ g)	Intrinsic Mass Magnetization (emu/g)	Intrinsic Mass Magnetization ($\times 10^{-2}$ μ_B/Fe)
NH-1	46.8 (7)	5040 (70)	80 (2)	0.59 (2)	0.90 (3)
NH-2	47.7 (3)	5140 (30)	75.2 (8)	0.634 (8)	0.99 (1)
NH-3	48.7 (3)	5250 (70)	82 (2)	0.59 (2)	0.93 (3)
NH-4	55.6 (4)	6000 (50)	105 (2)	0.53 (1)	0.82 (2)

Table 8.3 Calculated supermoment and mass of SP particles in nanohematite samples and derived intrinsic mass magnetization

8.3.3 Estimation of Additional Parameters

The estimated particle sizes for the nanohematite samples are shown in table 8.4. The values are in the limit of SD-SP behaviour for hematites estimated by Banerjee (1971). However, they are smaller than the nanohematite size dimensions of 250 nm to 500 nm observed by Strangway *et al.* (1967) showing superparamagnetism in magnetization-field cycles.

Sample	Particle Size (nm)
NH-1	30.7 (3)
NH-2	30.1 (1)
NH-3	31.0 (3)
NH-4	33.7 (2)

Table 8.4. Estimated particle sizes for the nanohematite samples

The size dimensions presented in table 8.4 are higher than the particle sizes estimated previously using the powder X-ray diffraction (pXRD) data (section 4.3.2). Consequently, a deeper analysis of the method of extraction of the particle mass for these nanohematites was approached since probably the ideal linear region for extracting the C_1 and C_2 values could be in the region of H^2 smaller than 2×10^5 G^2 (~ 400 G) (figure 8.33). In this sense, we

considered a graph of m_p versus H^2, where the mass values were calculated using the C_1 and C_2 of different straight lines connecting consecutive data points in the χ_g versus H^2 graph. Figure 8.34 shows this graph for sample NH-1; the other samples have similar graphs.

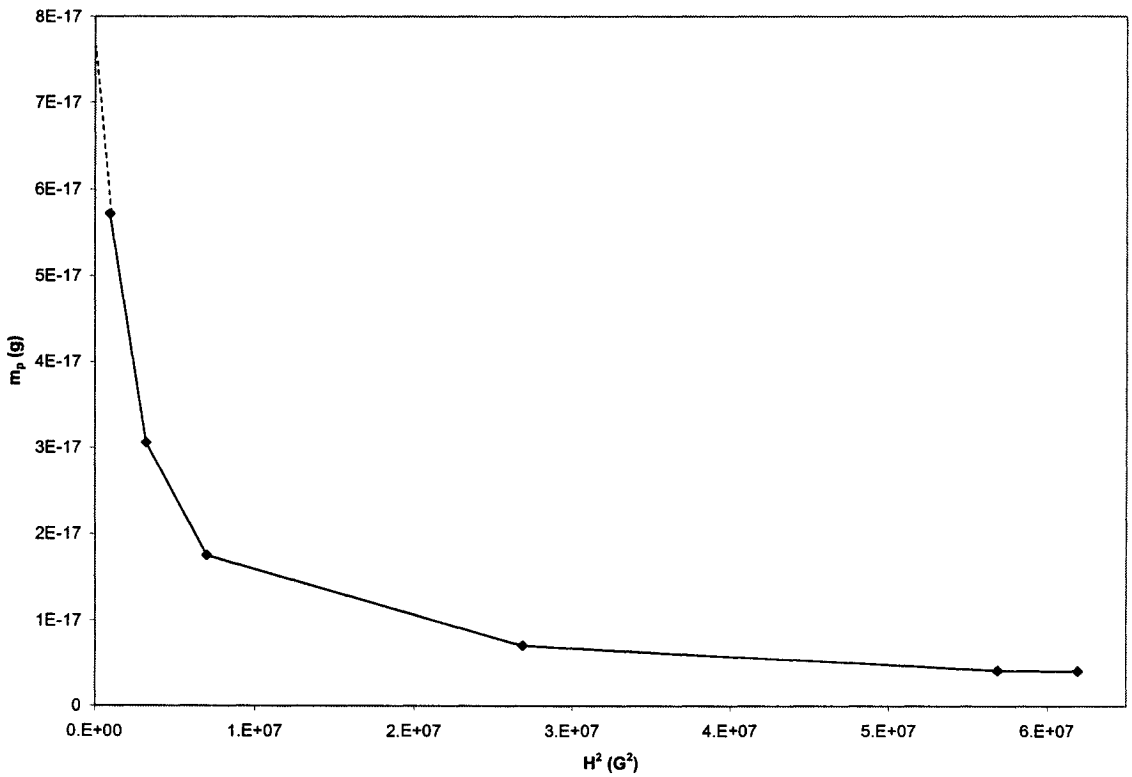

Figure 8.34 Extrapolation of m_p values to low field region in NH-1

The dashed line is an approximate visual extrapolation of the tendency of the curve to very small fields. This line intercepts the y-axis between the m_p values of 7×10^{-17} g and 8×10^{-18} g, giving size dimensions between 29 nm and 31 nm, which are approximately similar values to those calculated through the magnetic granulometry method.

The fact that the linear region needed for extracting the supermoment and mass is limited to low fields makes the procedure sensitive to the bigger particles that saturate at lower fields. Figure 8.35 shows the agreement between the measured magnetization curve and the simulated curve of NH-1, calculated by introducing the extracted parameters (μ and m_p) into the Langevin expression (equation 2-2, where $m_p = \frac{N}{n}$); the graphs for the rest of the nanohematite samples are similar. It is shown that the simulated magnetization curve only agrees with the measured curve at low fields therefore yielding particle sizes representing only the larger particles. Thus, the procedure is not sensing the presence of the smaller particles, which are more difficult to saturate due to their higher thermal energy.

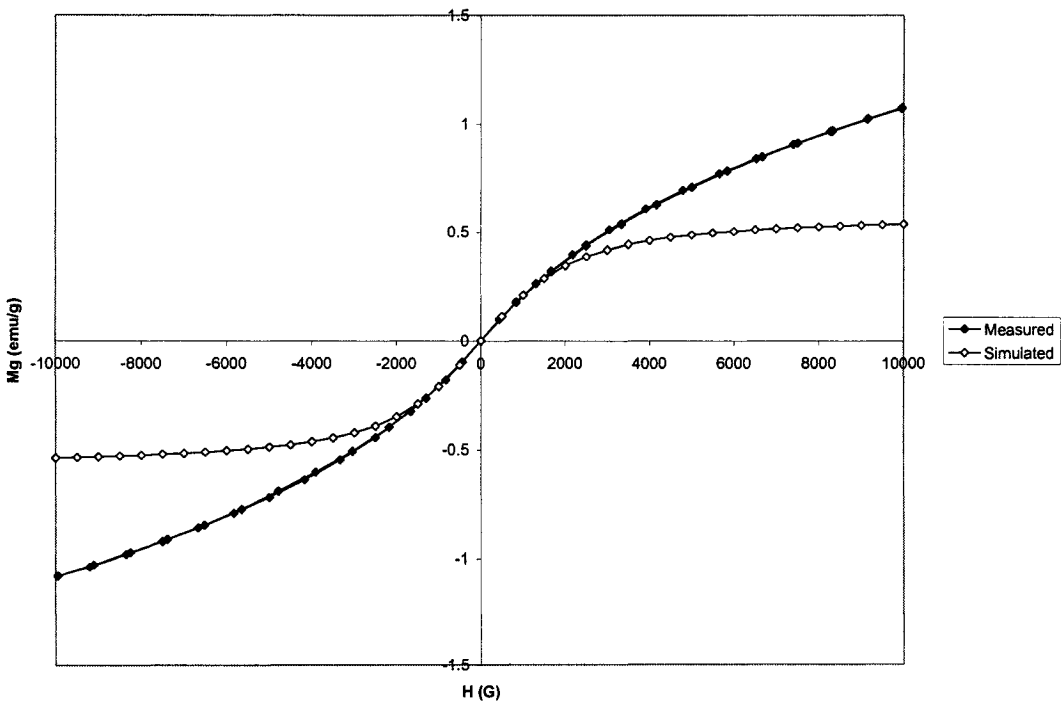

Figure 8.35 Measured and simulated magnetization curve for NH-1

The resultant estimated particle sizes for the nanohematite samples shown in table 8.4 could also be representing a magnetic particle size. This idea suggests the presence of magnetic clusters of nanohematite and possibly 6-line ferrihydrite attached to its surface resulting in a magnetic particle size of approximately 30 nm. Evidently, the fact that the nanohematite samples are a mixture of nanohematites and ferrihydrite makes the interpretation more complex.

Table 8.5 shows the calculated μ' and n values and derived percentage of magnetic moments contributing to the supermoment. The fraction of magnetic moments contributing to the supermoment is one order of magnitude less than for the 2-line ferrihydrites, mainly due to the different structural order and greater crystallinity in the nanohematite samples.

Sample	n ($\times 10^3$)	μ'	% Moments Contributing to μ
NH-1	301 (9)	1009 (10)	0.34 (1)
NH-2	284 (3)	1028 (6)	0.362 (4)
NH-3	309 (8)	1050 (10)	0.34 (1)
NH-4	397 (6)	1200 (10)	0.302 (5)

Table 8.5 Estimated values of total number of magnetic moments per particle (n) and number and percentage of magnetic moments contributing to it (μ')

The fraction of moments contributing to the supermoment of these nanohematites has a contribution from the uncompensated moments within the AF structure (defect moment) and from the spin-canted moment characteristic of hematite particles. The spontaneous moment per particle for all the nanohematite samples (M_s in Bohr magnetons per particle) is approximately 200 μ_B. This is a much larger magnitude than that expected for the spontaneous moment due to only spin-canting: approximately 15 μ_B/particle, assuming a

canting angle of 10^{-4} rad (Dzyaloshinsky, 1958). This suggests that the defect moment originating from the uncompensation of moments is the main contributor to the measured supermoment. In this sense, the exploration of a possible moment formation mechanism based on imperfect cancellation of the AF sublattices, in an analogous way to that done for the ferrihydrite samples, becomes applicable for these nanohematite samples.

The exploration of a moment formation mechanism of the form of equation 8-1 was done with the nanohematite samples. Figure 8.36 shows the $ln(\mu')$ versus $ln(n)$ graph for these samples along with fit lines through the data representing different α (exponent) values. The best-fit line through the points gives an exponent α of 0.47 (3) and a proportionality factor A of 3 (1), suggesting the relationship: $\mu'=3n^{0.47}$. This best-fit is consistent with the simple model proposed by Neél (1961):$\mu' \propto n^{1/2}$ (exponent α=0.5) that represents the occurrence of random uncompensation of moments within the AF sublattices. The models based on the exponents: $^1/_3$ (=0.333), $^2/_3$ (=0.667) and 1, are not consistent with the data.

Note that in contrast to the ferrihydrites' case, the resultant proportionality factor in the consistent model for the nanohematite samples is greater than one. A possible physical meaning for this proportionality factor is not clear. Nevertheless, the methodology used enables the exploration of the plausibility of simple models for explaining the moment formation mechanism.

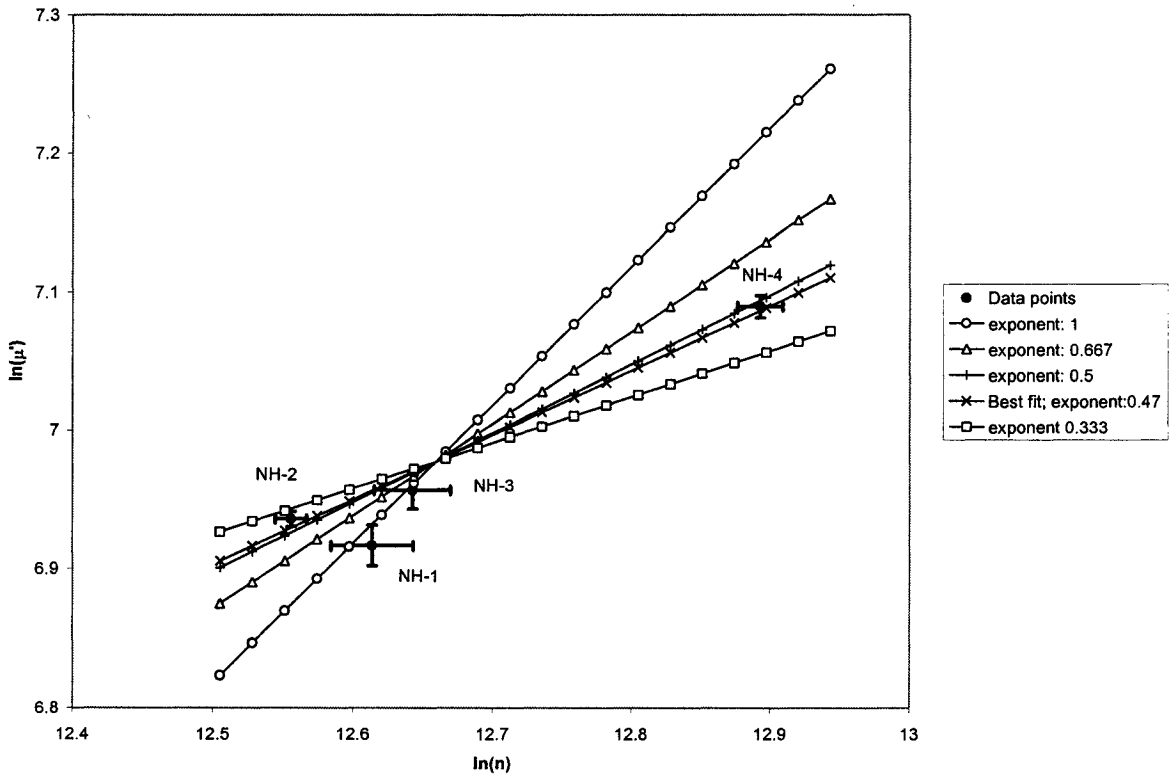

Figure 8.36 Linear fits through the data points of the nanohematites associated with different α values in the moment formation model $\mu'=An^{\alpha}$

In analogy to the ferrihydrite samples, a more complex moment formation model represented by equation 8-3, which assumes a combination of different simple models, can be considered for the nanohematite samples. The net supermoment of a nanohematite particle could be the result of the contribution of the uncompensated moments due to the presence of random defects throughout the particle ($Bn^{1/2}$), along with the moments uncompensated due the limit of the surface ($An^{2/3}$), and the spin-canted moment characteristic of hematite particles (Cn). In the same way as with the ferrihydrites, there is the need to work with a greater amount of data in order to explore in more depth these contributions to the total moment formation mechanism. Nevertheless, the data available for both the ferrihydrites and

the nanohematites has been able to discard certain commonly described simple models in the type of samples considered.

Conclusions

Mineral magnetometry has shown to be a very sensitive characterization tool to characterize synthetic microcrystalline hematite samples that are single-domain and synthetic nanophase hematite and ferrihydrite samples that are superparamagnetic. The analysis of the basic hysteresis parameters of the single-domain samples has provided insight into important characteristics of the samples. A distinction of the type of magnetic anisotropy present in the basal plane of these samples was made, along with the examination of different proportions and arrangements of defects among them. Additionally, the effect of annealing on the origin of the spontaneous magnetic moment was examined, and the relative insensitivity of the high field susceptibility to sample-to-sample variations was observed.

The analysis of the magnetic data of the superparamagnetic nanohematite and ferrihydrite samples, using a recently developed method, has been able to provide particle size dimensions and intrinsic magnetic properties, such as the intrinsic mass magnetization. The extracted parameters enabled the direct comparison of the intrinsic parameters of the superparamagnetic and the single-domain (magnetically blocked) samples. It has been seen that the co-precipitation of sulphur or phosphate in the 2-line ferrihydrite samples affects the intrinsic magnetization and particle size. The exploration of possible moment formation mechanisms gives insight into the structural differences between the 2-line ferrihydrites and 6-line ferrihydrite. Additionally, it suggests possible simple models of moment formation mechanism for the ferrihydrite and the nanohematite samples. The latter samples should be

studied in more detail considering the fact that they are a mixture of nanohematite and 6-line ferrihydrite, and given the proximity of their blocking temperature to room temperature.

The methodology developed in this work using synthetic samples could be applied in the future to natural samples containing the type of iron oxides and iron oxyhydroxides that the synthetic samples used in this study intend to resemble. In the same way, the magnetic granulometry method used for the superparamagnetic samples could also be applied to synthetic and natural samples that contain mixtures of the type of superparamagnetic samples studied, paramagnetic species, and ferromagnetic or ferrimagnetic phases (Rancourt *et al.*, 2004).

References

Ashcroft, N. W. and N. D. Mermin. 1976. *Solid State Physics* R. Holt and Winston. Philadelphia: Saunders College.

Banerjee, S. K. 1963. "An Attempt to Observe the Basal Plane Anisotropy of Hematite" *Philosophical Magazine* Ser.8, 8:2119-2120.

Banerjee, S. K. 1971. "New Grain Size Limits for Palaeomagnetic Stability in Haematite". *Nature Physical Science* 232:15-16.

Bean, C. P. and J. D. Livingston. 1959. "Superparamagnetism" *Journal of Applied Physics* 30:1205-95.

Besser, P. J., A. H. Morrish, and C. W. Seerle. 1967. "Magnetocrystalline Anisotropy of Pure and Doped Hematite." *Physical Review* 153:632-40.

Bigham, J. M., U. Schwertmann, S. J. Traina, R. L. Winland, and M. Wolf. 1996. "Schwertmannite and the Chemical Modeling of Iron in Acid Sulfate Waters." *Geochimica Et Cosmochimica Acta* 60:2111-21.

Bishop, J. L. 1998. "Biogenic Catalysis of Soil Formation on Mars?" *Origins of Life and Evolution in the Biosphere* 28:449-459

Carlson, L., J. M. Bigham, U. Schwertmann, A. Kyek, and F. Wagner. 2002. "Scavenging of As From Acid Mine Drainage by Schwertmannite and Ferrihydrite: a Comparison With Synthetic Analogues." *Environ. Sci. Technol.* 36:1712-19.

Catti, M., G. Valerio and R. Dovesi. 1995. "Theoretical Study of Electronic, Magnetic, and Structural Properties of α-Fe_2O_3 (hematite)." *Physical Review B* 51:7441-7450.

Cornell, R. M. and U. Schwertmann. 1996. *The Iron Oxides - Structure, Properties, Reactions, Occurrence and Uses*. Weinheim: VCH.

Crangle, J. 1991. *Solid State Magnetism*. New York: Van Nostrand Reinhold.

Dang, M.-Z., D. G. Rancourt, J. E. Dutrizac, G. Lamarche, and R. Provencher. 1998. "Interplay of Surface Conditions, Particle Size, Stoichiometry, Cell Parameters, and Magnetism in Synthetic Hematite-Like Materials." *Hyperfine Interactions* 117:271-319.

Dunlop, D. J. 1970. "Hematite: Intrinsic and Defect Ferromagnetism" *Science* 169:858-860.

Dunlop, D. J. 1971. "Magnetic Properties of Fine-particle Hematite" *Annales de Geophysique* 27:269-293.

Dunlop, D. J. and Ö. Özdemir. 1997. *Rock Magnetism. Fundamentals and Frontiers* Cambridge University Press.

Dzyaloshinsky, I. 1958. "A Thermodynamic Theory of "Weak" Ferromagnetism of Antiferromagnetics." *Journal of Physics and Chemistry of Solids* 4:241-55.

Eggleton, R. A. and R. W. Fitzpatrick. 1988. "New Data and a Revised Structural Model for Ferrihydrite." *Clays and Clay Minerals* 36:111-24.

Flanders, P. J. and J. P. Remeika. 1965. "Magnetic Properties of Hematite Single Crystals" *Philosophical Magazine* Ser. 8, 11:1271-1288.

Foner, S. 1959. "Versatile and Sensitive Vibrating-Sample Magnetometer." *Review of Scientific Instruments* 30:548-557.

Fuller, M. D. 1970. "Geophysical Aspects of Paleomagnetism" *CRC Critical Reviews in Solid Sciences* 1: 137-219.

Gallon, T. E. 1968. "The Remanent Magnetization of Haematite Single Crystals" *Proceedings of the Royal Society of London* Ser. A 303:511-524.

Halgeldahl, S. L. 1995. "Bitter Patterns Versus Hysteresis Behavior in Small Single Particles of Hematite." *Journal of Geophysical Research* 100:359-64.

Jambor, J. L. and J. E. Dutrizac. 1998. "Occurrence and Constitution of Natural and Synthetic Ferrihydrite, a Widespread Iron Oxyhydroxide." *Chemical Reviews* 98:2549-85.

Janney, D. E., J. M. Cowley, and P.R. Buseck. 2000. "Transmission Electron Microscopy of Synthetic 2- and 6-Line Ferrihydrite." *Clays and Clay Minerals* 48:111-19.

Janney, D. E., J. M. Cowley, and P. R. Buseck. 2001. "Structure of Synthetic 6-Line Ferrihydrite by Electron Nanodiffraction." *American Mineralogist* 85:327-35.

Jansen, E., A. Kyek, W. Schäfer and U. Schwertmann. 2002. "The Structure of Six-Line Ferrihydrite" *Applied Physics A* 74 [Suppl.]: S1004-S1006

Kletetschka, G and P J. Wasilewski. 2002. "Grain Size Limit for SD Hematite" *Physics of the Earth and Planetary Interiors* 129:173-79.

Kobayashi, K. and M. D. Fuller. 1967. "Vibration Magnetometer" Pp. 450-456 in *Methods in Palaeomagnetism*, editors D.W. Collinson, K. M. Creer and S. K. Runcorn. Elsevier.

Lin, S. T. 1959. "Magnetic Properties of Hematite Single Crystals. I. Magnetization Isotherms, Antiferromagnetic Susceptibility, and Weak Ferromagnetism of a Natural Crystal" *Physical Review* 116:1447-1452

Moriya, T. 1960. "Anisotropic Superexchange Interaction and Weak Ferromagnetism." *Physical Review* 120:91-98

Néel, L. and R. Pauthenet. 1952. "Étude thermomagnétique d'un monocristal de $Fe_2O_3\alpha$" *Comptes Rendus Hebdomadaires des Séances de l'Académie des Sciences* 234 :2172-2174.

Néel, L. 1953. "Some New Results on Antiferromagnetism and Ferromagnetism" *Reviews of Modern Physics* 25:58-63.

Néel, L. 1961. "Superparamagnétisme Des Grains Très Fins Antiferromagnétiques." *Comptes-Rendus Des Séances De L'Académie Des Sciences* 252:4075-80.

O'Reilly, W. 1984. *Rock and Mineral Magnetism*. Glasgow and London: Blackie.

Pankhurst, Q. A. and R. J. Pollard. 1992. "Structural and Magnetic Properties of Ferrihydrite." *Clays and Clay Minerals* 40:268-72.

Porath, H. and C.B. Raleigh. 1967. "An Origin of the Triaxial Basal-Plane Anisotropy in Hematite Crystals" *Journal of Applied Physics* 38:2401-2402.

Porath, H. 1968. "Stress Induced Magnetic Anisotropy in Natural Single Crystals of Hematite" *Philosophical Magazine* Ser.8 17:603-608.

Preston, D. W. and E. R. Dietz. 1991. *The Art of Experimental Physics*. New York: John Wiley and sons.

Pruysers, P. A., G. J. de Lange, J. J. Middelburg, and D. J. Hydes. 1993. "The Diagenetic Formation of Metal-Rich Layers in Sapropel-Containing Sediments in the Eastern Mediterranean." *Geochimica Et Cosmochimica Acta* 57:527-36.

Rancourt, D. G. 1998. "Mössbauer Spectroscopy in Clay Science." *Hyperfine Interactions* 117:3-38.

Rancourt, D. G. 2001. "Magnetism of Earth, Planetary, and Environmental Nanomaterials." Pp. 217-92 in Reviews in Mineralogy and Geochemistry Volume 44: *Nanoparticles and the Environment*, editors J. F. Banfield and A. Navrotsky. Mineralogical Society of America.

Rancourt, D. G., D. Fortin, T. Pichler, P.-J. Thibault, G. Lamarche, R. V. Morris, and P. H. J. Mercier. 2001. "Mineralogy of a Natural As-Rich Hydrous Ferric Oxide Coprecipitate Formed by Mixing of Hydrothermal Fluid and Seawater: Implications Regarding Surface Complexation and Colour Banding in Ferrihydrite Deposits." *American Mineralogist* 86:1-18.

Rancourt, D. G., F. González-Lucena and P. J. Thibault. 2004. "Magnetic granulometry from equilibrium magnetization measurements: Mineral magnetometry of superparamagnetic particles and application to synthetic ferrihydrites." In press *American Mineralogist.*

Roberts, D. R., D. G. Rancourt and C. P. Slomp. 2003. "Oxidative diagenesis of sapropel S1 in the eastern Mediterranean Sea" Unpublished.

Seehra, M. S., V. S. Babu and A. Manivannan. 2000. "Neutron Scattering and Magnetic Studies of Ferrihydrite Nanoparticles." *Physical Review B* 61(5):3513-18.

Strangway, D.W., B. E. McMahon, R. M. Honea and E. E. Larson. 1967. "Superparamagnetism in Hematite" *Earth and Planetary Science Letters* 2:367-371.

Tasaki, A and S. Iida. 1963. "Magnetic Properties of Synthetic Single Crystals of αFe_2O_3" *Journal of the Physical Society of Japan* 18:1148-1154.

Thompson, R. and F. Oldfield. 1986. *Environmental Magnetism.* Allen & Unwin .

Torii, M., K. Fukuma, C.-S. Horng, and T.-Q. Lee. 1996. "Magnetic Discrimination of Pyrrhotite- and Greigite-Bearing Sediment Samples." *Geophysical Research Letters* 23:1813-16.

van der Zee, C., D. R. Roberts, D. G. Rancourt and C. P. Slomp. 2003. "Nanogoethite is the dominant reactive oxyhydroxide phase in lake and marine sediments." *Geology* 31 (11): 993-996.

Zergenyi, R. S., A. M. Hirt, S. Zimmermann, J. P. Dobson, and W. Lowrie. 2000. "Low-Temperature Magnetic Behavior of Ferrihydrite." *Journal of Geophysical Research* 105:8297-303.

Appendices

Appendix A - Functioning and Limitations of the VSM

One of the first stages of work of this thesis project consisted in understanding the functioning and limitations of the VSM model 7304 manufactured by Lake Shore Cryotronics, Inc. when performing hysteresis cycles. This was done through many types of experiments that test reproducibility, precision and appropriate positioning of the sample. As experiments were performed, several problems were encountered, which were approached by doing tests and analyzing the corresponding data. This led to the identification of several artifacts of the Lake Shore VSM. Thus, several recommendations are given for correcting and dealing with these artifacts in order to obtain a set of precise and comparable results. Through this process the methodology of work evolved towards a more effective and efficient way of using the VSM. The results include a list of additional suggestions for the use of the VSM (see appendix B) and the elaboration of a run sheet (see appendix D) that suggests to the user how to record in paper the most relevant information for the experiments performed. Below are listed the different tests performed.

A.1 Calculation of the Statistical Error in the Measured Magnetic Moment

This procedure was done to test the precision in the magnetic moment value. For this, time experiments, where the moment is measured as a function of time, were run on two different samples at two fixed field values: 1 kG and 8 kG, to see if there is a dependence of moment variation with field. The samples used are separate portions of the lake sediments

RS-2 and RS-3; these are powdered samples and they are described in chapter 3 (Exploratory Work).

The statistical error in the measured magnetic moment was taken as the standard deviation of the residuals of the linear trend line fitted through the scattered points. This linear trend was not always horizontal for the same sample: a drift through time in the moment values was present in several runs. Thus, the estimation of the statistical error done presented here does not take into account this possible drift.

For each field value (1 kG or 8 kG), the residuals associated with the two samples were grouped and an estimated error value was calculated. The resultant statistical errors in the moment are shown in table A.1

Field (G)	Error in Measured Magnetic Moment (emu)
1000	4×10^{-6}
8000	5×10^{-6}

Table A.1 Calculated statistical error in measured magnetic moment at low and high magnetic fields

These estimated errors do not seem to vary significantly with field and they are in agreement with the error in the measured moment claimed by the manufacturer: 5×10^{-6} emu.

A.2 Reproducibility of the Measured Moment

Hysteresis cycles at room temperature were run twice (with the same settings and conditions) for two different samples to examine the reproducibility in the measured magnetic moment. The samples used are the same lake sediments that were used for the

estimation of the statistical error of the measured moment (section A.1). For each sample, the reproducibility was quantified by calculating the absolute differences between the shift-corrected moment measurements for each of the two runs at each field value. Table A.2 shows the average absolute difference between the two runs of each sample and the maximum absolute moment value (μ_s) measured at the highest field (± 10 kG) along with the estimated reproducibility. There is not an observable dependence of reproducibility with measured moment, thus, from these tests the estimated range of reproducibility is between 0.9 % and 1.9 % of the measured magnetic moment at each corresponding field value.

Sample	Average Absolute Difference (emu)	Maximum μ_s (emu)	Reproducibility (%)
RS-2	1.07×10^{-5}	0.0012	0.9
RS-3	2.24×10^{-5}	0.0012	1.9

Table A.2 Estimated reproducibility of the measured magnetic moment

A.3 Magnetization Shift of the Hysteresis Cycle

One of the problems encountered when performing experiments was that the resultant cycles seemed shifted in the moment axis in a different value each time they were run. The cycle starts at a value on the moment axis, which can be small or large in magnitude and either positive or negative, and the cycle continues from that initial shifted value. The occurrence of these shifts was studied and analyzed and they were concluded to be of a random nature. But, in general, they are larger in magnitude after manipulating the rod for changing samples.

After a test session with a Lake Shore technician, it became convenient to set all moment offsets to zero in the settings of the software in order to minimize the effect of this artifact. This suggestion is indicated in the general guidelines for the use of the VSM (appendix B). But even after this precaution is taken the resultant graphs present shifts that are generally of a smaller magnitude. In order to make a better visual comparison among samples, this small shift effect ("centre shift") is corrected as described in section 5.3.

A.4 Saddling Region

When working with big quantities of samples that occupy larger regions in the Z-direction of the holder sample space length, there is the concern of the appropriate saddled position. The range of position in the Z-axis of the saddled region was tested by running time experiments with the reference nickel sphere sample provided with the VSM. In these experiments, the moment is measured as a function of time at a fixed high saturating field for different positions on the Z-axis. The experiments show that there is no difference in the moment values throughout the Z-axis length corresponding to the space that could be visually considered as in between the detection coils; therefore, all the sample volume in this region is detected and measurable.

Appendix B - General Guidelines for the Use of the VSM

This appendix consists of a series of suggestions supplementary to the information in the User's Manual for a convenient use of the VSM model 7304 manufactured by Lake Shore Cryotronics, Inc., located at the Magnetometry Lab, room B30 in the MacDonald building at the University of Ottawa. They are the result of various experiments performed (appendix A) with the objective of testing the limits of satisfactory performance of the device.

B.1 Initiating the VSM system

- Turn on water chiller.
- Turn on the flow of the water system to the VSM.
- Turn on power supply.
- Turn on the VSM main controller and computer.
- The IDEAS-VSM software version 3.0.1 works properly only if it is started, exited and restarted again, due to a moment meter error message.
- Before each session and each time the program is closed and reopened, the following have to be checked in the moment meter dialog window:
    - Set all moment offset to zero: Failure to set this could result in significant random shifts in the moment value for the whole cycles.
    - Set the Auto Range function to ON.

- Before each session and even before calibration, it is recommended to warm up the head drive (turn it on) for at least one hour.

B.2 Calibrations

Three calibrations can be performed before taking measurements. If all three calibrations are to be performed, they should be done in the following order:

- Gaussmeter calibration: This is required when the moment reading at zero field (after ramping to 0) is greater than ± 0.05 G.
- Moment offset calibration
- Moment gain calibration: This calibration should be performed before each daily session of measurements. It involves saddling in the three directions: X, Y and Z. When saddling consider the following:
    - First, the sample can be centred by visual inspection.
    - If a cryostat or furnace is to be attached, it is recommended to saddle before either is attached, so that saddling could be performed easier afterwards.
    - Make sure the hall probe is not in contact with anything (e.g., the cryostat).
    - The knob in the front controls the front-back direction where the saddled position requires a maximum in moment.
    - The knob at the right side controls the left-right direction, which requires a minimum in moment.
    - Saddling in the Z direction requires a maximum in moment.
    - After turning each knob consider the moment value that stabilizes when you are not touching the knobs.

- According to Foner (1959), the saddling procedure guarantees that small further displacements of the sample in any direction will not affect the output of the signal.

B.3 Edition of Experiments

- The Auto Range function is active when it is checked both in the edition window of the experiment and in the moment meter range in the Moment Meter Dialog Box. Thus, when creating an experiment be sure to check Auto Range ON in order for it to stay as a default setting each time you run the experiment.
- When choosing to work with a fixed sensitivity, choose one according to the moment values expected at saturation.

B.4 Sample

- If working with a sample volume that does not permit the holder to screw in completely, adjust the Z direction so that the sample volume is visually centred between the coils.

Appendix C - Weighing Procedure

The weighing of the samples was done using a Sartorius MP2 microbalance which has a precision up to 1×10^{-6} g. This high precision makes the effect of the mass error small on the final error in the mass magnetization value. The use of a common balance with a precision of 1×10^{-4} g would increase the mass error obtained with the microbalance up to 700%, and therefore the effect of the final error would be bigger. Considering the samples studied and the type of sample holders used, it is recommended to follow the suggestions outlined below when weighing the samples.

The sample can be weighted inside the holder to minimize errors due to sample lost on the weighing paper surface, but only the bottom part of the holder with the sample should be weighted; adding the top part would be excessive weight for the microbalance. Since the holders used cannot be in an upright position due to their lack of a flat bottom, aluminum foil cups (Al cups) are used to hold upright the bottom part of the holder that contains the amount of sample being weighted. The choice of Al cups is based on their small weight (lighter than tin cups) and their good manipulability.

The suggested procedure for weighing is the following:

- Weight the Al cup with the bottom part of the holder inside. It is recommended to do this for each holder since they have variations in weight.
- Pour the sample into the holder using the metallic spatula; it is better to do this if the holder is taken out of the Al cup.

- Put the holder (with sample) in the Al cup, weight this.
- The resultant weight of the sample is:

$$weight(sample) = weight(Alcup + holder + sample) - weight(Alcup + holder)$$

NOTE: Always use the tweezers to introduce, take out and manipulate aluminum cups and bottom parts of holders, since touching them with your fingers could add weight due to moisture and contamination.

Appendix D – VSM Run Sheet

Date													
User													
Calibrations													
Sample Name													
Filename													
Holder													
Experiment Type *													
Experimental settings													
Temperature range													
Field range													
Sample description													
Sample mass													
Comments													

* (P): profile; (E): experiment

Appendix E - Units of Magnetic Quantities

All the measured and derived magnetic quantities used in this study are expressed in the cgs (emu) magnetic unit system. Table E.1 indicates the units used for each quantity and the corresponding units in the SI. The quantity in SI units is obtained by multiplying the quantity in cgs units by the conversion factor.

Magnetic Quantity	Symbol	cgs (emu) Unit System	Conversion Factor	SI Unit System
Sample Magnetic Moment	μ_s	emu	10^{-3}	J/T
Applied Magnetic field	H	G	10^{-4}	T
Mass Magnetization	M_g	emu g^{-1}	1	J $T^{-1}kg^{-1}$
Mass Susceptibility	χ_g	emu $g^{-1}G^{-1}$	10^{-4}	J $T^{-2}kg^{-1}$

Table E.1 Units of magnetic quantities and their conversion to SI units